INVESTIGATIONS OF HEXAGONAL BORON NITRIDE AS A SEMICONDUCTOR FOR NEUTRON DETECTION

By

JOSEPH YAZBECK

B.S., University of Michigan-Dearborn, 2009

A THESIS

Submitted in partial fulfillment of the requirements for the degree

MASTER OF SCIENCE

Department of Mechanical and Nuclear Engineering
College of Engineering

KANSAS STATE UNIVERSITY
Manhattan, Kansas

2012

Approved by:

Co-Major Professor
Dr. William L. Dunn

Approved by:

Co-Major Professor
Dr. Jeffrey Geuther

Abstract

The properties of hexagonal boron nitride (h-BN) as a semiconductor neutron detection medium were investigated. Single h-BN crystal domains were synthesized by the Chemical Engineering department at Kansas State University (KSU) using crystallization from molten metal solutions. At Texas Tech. University (TTU), a detector was fabricated using epitaxial h-BN growth on a sapphire substrate where metallic micro-strip contacts 5 μm apart and 5 nm thick where deposited onto the un-doped h-BN. In this research both the crystal domains synthesized at KSU and the detector fabricated at TTU were tested for neutron response. Neutron irradiation damage/effects were studied in pyrolytic h-BN by placing samples in the central thimble of the TRIGA MARK II reactor at KSU and irradiating at increasing neutron fluences. The domains synthesized at KSU as well as the detector fabricated at TTU showed no response to neutron activity on a MCA pulse height spectrum. Conductivity analysis showed abrupt increases in the conductivity of the pyrolytic h-BN at around a fluence of 10^{14} neutrons per cm^2. Bandgap analysis by photoluminescence on the irradiated pyrolytic h-BN samples showed shifts in energy due to towards plane stacking disorders upon neutron irradiation. Future efforts may include the introduction of dopants in h-BN growth techniques for charge carrier transport improvement, and mitigation of plane stacking disorders.

Table of Contents

List of Figures

List of Tables

List of Symbols

^{239}Pu	plutonium isotope with atomic mass 239
^{235}U	uranium isotope with atomic mass 235
^{113}Cd	cadmium isotope with atomic mass 113
^{3}He	helium isotope with atomic mass 3
^{6}Li	lithium isotope with atomic mass 6
^{10}B	boron isotope with atomic mass 10
E	energy
h	Planck's constant
$\hbar$	Planck's constant divided by 2π
ν_f	average number of neutrons produced by fission
ν	frequency
λ	photon wavelength
Δ	change in
m	mass
i	complex variable: $\sqrt{-1}$, or statistical Monte Carlo element
k	Boltzmann constant
ε_o	permittivity of free space
ε_s	permittivity of semiconductor material
ε_A	absolute efficiency
ε_R	relative efficiency
ε_i	intrinsic efficiency
μ	micron
μ_e	electron mobility
μ_h	hole mobility
v_e	electron drift velocity
v_h	hole drift velocity
Ω	solid angle
σ	microscopic cross-section
Σ_a	macroscopic absorption cross-section
σ_I	conductivity
ρ	random number between 0 and 1
$\rho_{^{10}\mathrm{B}}$	mass density of ^{10}B
c	velocity of light
n	neutron
p	proton

List of Abbreviations

KSU	Kansas State University
TTU	Texas Tech. University
BN	boron nitride
h-BN	hexagonal boron nitride
g-BN	graphitic hexagonal boron nitride
CVD	chemical vapor deposition
NCM	neutron conversion medium
CENDL	China Nuclear Data Center and Chinese Nuclear Data Network
ATM	atmosphere
PMT	photo-multiplier tube
pdf	probability distribution function
APD	avalanche photodiode
e	electron
e^-	electron charge
e-hole	electron hole pair
e-ion	electron ion pair
Av	Avogadro's number
MNE	Mechanical and Nuclear Engineering department at KSU
eV	electron volt
keV	kilo electron volt
MeV	million electron volt
SRIM	stopping and range of ions in matter
LLD	lower level discrimination
ULD	upper level discrimination
MCA	multi-channel analyzer
MOCVD	metal organic chemical vapor deposition
LHS	left hand side of an equation
RHS	right hand side of an equation

Acknowledgements

Some parts of this work would not have been possible to achieve without the help of the following: The chemical engineering department at KSU , headed by Dr. James Edgar, promptly provided single crystal h-BN samples for testing, S.M.A.R.T. Laboratory staff, headed by Dr. Douglas McGregor, afforded forward facilities, equipment, materials, and advice and showed genuine interest in the successful and uninterrupted flow of experiments to their conclusion. The collaborative team at Texas Tech University, headed by Hong X. Jiang, provided detectors for testing as well as performed vital photoluminescence analysis of the bandgap of pyrolytic hexagonal boron nitride samples.

Dedication

I would like to dedicate this work firstly to my brother Antoine, his wife Majd, and my two nephews Tony and Jad for their emotional support during my graduate school period. Also, sincere dedication is extended to Dr. Jeffery Geuther, my immediate supervisor and co-advisor, and Dr. William L. Dunn, my advisor, for their moral, intellectual, and technical support. Dedication is also extended to the remaining members of my chosen committee, Drs. James Edgar and Douglas McGregor, for their support, advice, and genuine interest in my success.

Chapter 1 - Introductory Aspects

Applications of neutron detection are prevalent in science, engineering, and medicine. In medicine, neutrons play roles in imaging, dosimetry, and cancer treatment. In engineering, neutron detectors are crucial to nuclear energy research and nuclear power operations. In nuclear non-proliferation applications, neutron detection is a primary indicator of the presence of fissile materials such as ^{239}Pu.

This thesis is an account of a portion of a collaborative research project between Kansas State University (KSU) and Texas Tech. University (TTU). The project is focused on the development of a high efficiency semiconductor neutron detector based on hexagonal boron nitride (h-BN) for national security and non-proliferation purposes.

TTU's part of the project is the fabrication of the detector using epitaxial layers of h-BN grown via chemical vapor deposition (CVD) on a sapphire substrate (Li et al, 2011). KSU's part is divided between the Chemical Engineering Department (ChE) and the Mechanical and Nuclear Engineering (MNE) Department. The ChE Department is investigating h-BN single crystal growth methods from molten metal solutions (Kubota, et al, 2008). The MNE Department is investigating the relation between radiation damage and the useful lifetime of an h-BN based detector using pyrolytic BN, and is assessing the crystals synthesized by the KSU ChE Department, as well as testing the detector fabricated at TTU for neutron detection using the TRIGA MARK II reactor at KSU. In addition, Monte Carlo studies using Matlab programming were used by the KSU team for expected spectrum, average energy deposition per reaction, and neutron absorption prediction for different h-BN parameters, such as thicknesses and enrichment fraction of ^{10}B.

Section 1.1: Brief Introduction to Neutron Detection

Suitable Neutron Detection Materials

Due to their intrinsic charge neutrality, neutrons cannot directly ionize matter. A neutron conversion medium (NCM) affords indirect neutron detection. A NCM suitable for neutron detection is a medium which, whether by chemical composition or impregnation, contains an

isotope with a high microscopic neutron absorption cross-section; the isotope promptly releases ionizing radiation, such as gamma-rays (γ-rays) or charged particles upon the absorption of a neutron. Prompt release of ionizing radiation permits detection at the instant the neutron is absorbed. The isotopes ^{3}He, ^{6}Li, ^{10}B, ^{113}Cd, ^{235}U and ^{239}Pu are used by scientists and engineers, pure or as part of a medium, because they are suitable NCM's. The cross-sections in barns as a function of neutron energy in eV for the ^{3}He, ^{6}Li, ^{10}B, and ^{113}Cd isotopes are shown in Fig.1-1.

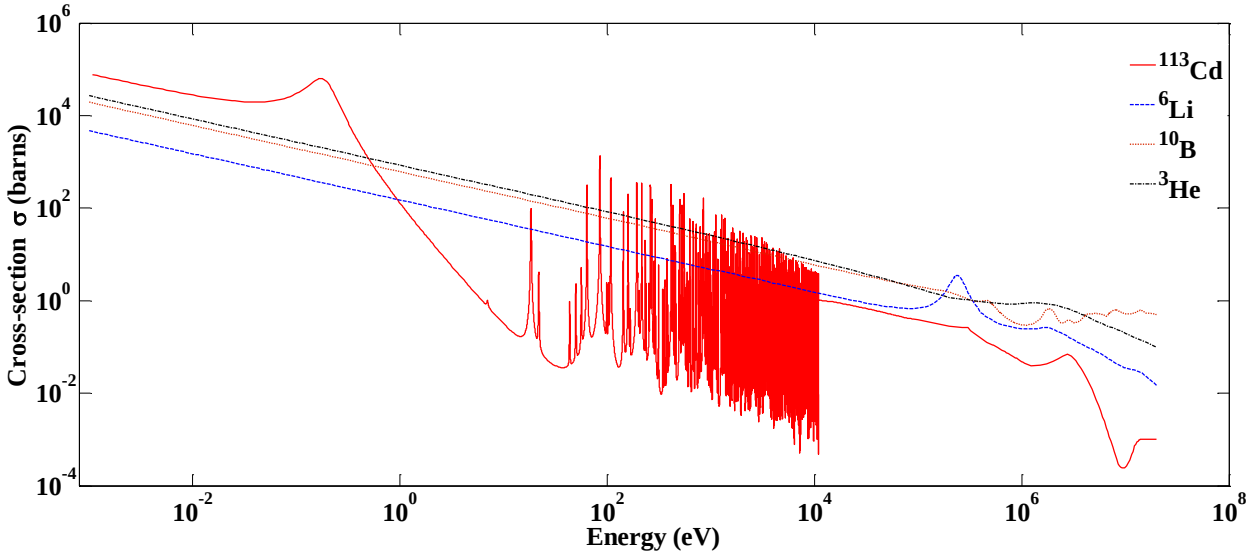

Figure 1-1: Microscopic neutron cross sections (σ) in barns for ^{3}He, ^{6}Li, ^{10}B, and ^{113}Cd as given by the China Nuclear Data Center and Chinese Nuclear Data Network (CENDL).

^{3}He is not a naturally occurring isotope on earth and is material leftover from the nuclear weapons manufacturing era; consequently, ^{3}He is expensive and becoming increasingly rare prompting research on efficient alternative NCMs such as the mentioned isotopes. The boron compound BN is being investigated for semiconductor properties and is of special interest, motivating the collaborative research between KSU and TTU.

Detectors: Energy Deposition, Efficiency, and Types

Radiation detectors respond to the energy deposited in the detection medium of the detector; neutron detectors generally use NCMs to generate directly ionizing radiation such as charged particles. When travelling through matter, charged particles deposit energy as described by the Bragg curve; energy deposition also defines the particle's range in the specific medium and is characteristic of the medium through which the particle is travelling. A sample Bragg curve for a

1.78 MeV alpha particle travelling in h-BN was developed by the *Stopping and Range of Ions in Matter* (SRIM) code (Ziegler, 2011) and is provided in Fig. 1-2; the figure shows more energy deposition near the end of the particle's range than at the beginning of the particle's range.

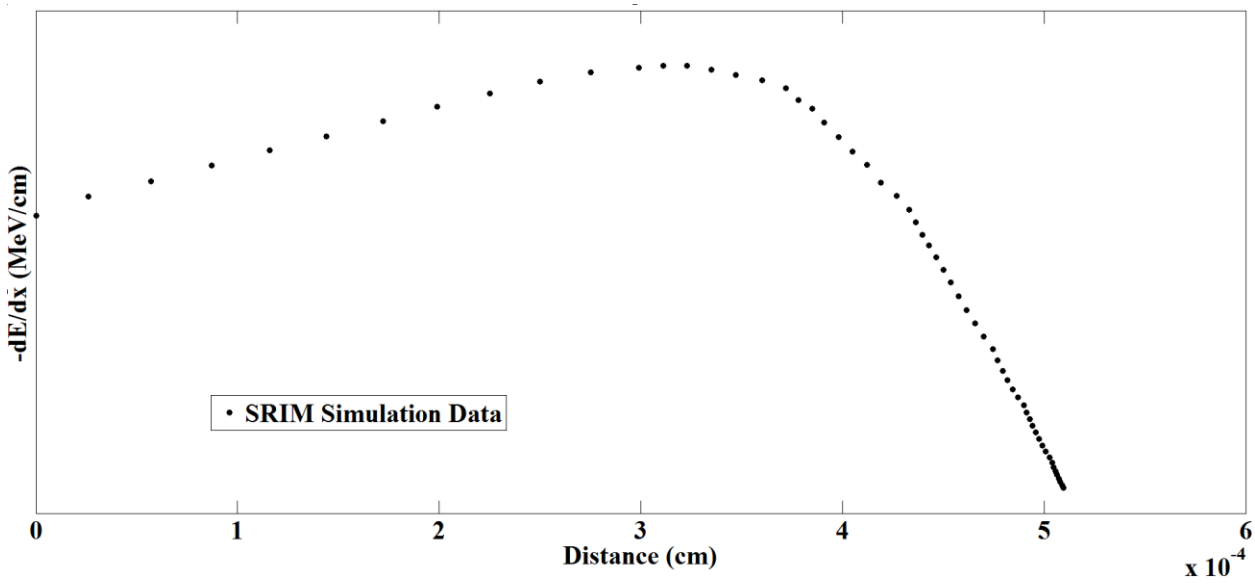

Figure 1-2: Bragg curve for a 1.78 MeV alpha particle in h-BN. A 1.78 MeV alpha particle was chosen because one of the ^{10}B neutron reactions produces such an alpha particle.

Neutron detectors make use of the nuclear reactions presented in Eqs.1-1.1 through 1-1.5 (Tsoulfanidis, and Landsberger, 2010) summarized below.

$$^{3}He + n \rightarrow {}^{3}H + p \qquad 1\text{-}1.1$$

$$\begin{array}{ll} 94\%\text{ probability} & {}^{10}B + n \rightarrow {}^{7}Li + {}^{4}He + \gamma\text{-ray} \\ 6\%\text{ probability} & {}^{10}B + n \rightarrow {}^{7}Li + {}^{4}He \end{array} \qquad 1\text{-}1.2$$

$$^{6}Li + n \rightarrow {}^{4}He + {}^{3}H \qquad 1\text{-}1.3$$

$$^{235}U + n \rightarrow \nu\,{}^{1}n + \text{fission products} \qquad 1\text{-}1.4$$

$$^{113}Cd + n \rightarrow {}^{114}Cd + \gamma\text{-ray} \qquad 1\text{-}1.5$$

In order to compare devices based on different materials and geometries, the devices' efficiencies must be compared. To simply describe total efficiency of a detector as the number of absorbed neutrons by which a detectable signal was generated in the detector divided by the number of neutrons impinging on the detector is intrinsically incomplete. The geometric set up

between source and detector, the source shape, and other factors play large roles in efficiency calculations. Due to the lack of standardization, detailed geometries—detector, source, and setup—have to be reported for the efficiency value to have full meaning. Although the different types of efficiencies are thoroughly discussed, described, formulated, and published elsewhere (McGregor and Shultis, 2011), efficiencies will again be discussed in this thesis for completeness.

Gas filled detectors

Most gas filled neutron detectors make use of neutron interactions with ^{3}He, ^{10}B, ^{6}Li, or ^{235}U with the prompt release of ionizing radiation in the form of charged particles into a gaseous medium. Charged particles passing through a gaseous medium deposit energy and leave a cloud of electron-ion (e-ion) pairs in their wake. The bias voltage applied across the gas separates the e-ion pairs and accelerates the electrons and ions in opposite directions. The collected charges generate a signal in the load resistor of the circuit in the form of a detectable pulse for each neutron interaction (Shultis and Faw, 2002).

A ^{3}He gas filled detector's neutron absorption efficiency—absorbed fraction—largely depends on the amount of gas in the detector's vessel. The amount of gas contained in the vessel is directly proportional to the vessel's size and gas pressure. Increasing the amount of gas increases the efficiency of the detector, but requires higher biasing voltages. The data in Table 1-1 provided by TGM DETECTORS (trademark by Saint-Gobain) shows how the bias voltage changes with both pressure and size for cylindrical ^{3}He tubes.

Table 1-1-1: Operating voltage data for ^{3}He detectors.

Pressure (atm)	2	4	6	8	10
Diameter (inch)	Operating Voltage				
0.5	750	950	1150	1350	1650
0.75	800	1000	1200	1400	1700

The cost of ^{3}He is around $ 1000.00/liter at standard temperature and pressure (STP), which is 1 atmosphere (atm) and 273 degrees Kelvin .

Scintillation Detectors

Scintillation detectors are composed of materials from which light is emitted when energy is deposited by some form of radiation. The scintillation material is usually connected to a photo-multiplier tube (PMT) or avalanche photodiode (APD), each of which transforms the emitted photons from the crystal to electrons and amplifies the electron current to detectable levels.

The isotope ^{113}Cd emits prompt γ-rays post neutron absorption, as indicated by Eq. 1-1.5, where ^{113}Cd may be used as an external NCM outside the scintillation material. Some scintillation crystals are designed to respond to heavy charged particles and the reactions in Eqs. 1-1.2 through 1-1.5 may be used when the crystal is impregnated with the appropriate isotopes. However, heavy charged particles cause physical damage, thus crystals such as thallium-activated sodium iodide NaI(Tl) which respond to γ-rays are usually preferred in order to avoid radiation damage effects caused by charged particles.

Semiconductor Detectors

Semiconductor detectors generate signals via charge collection as gas filled detectors do; however in semiconductor detectors, energy deposition generates electron-hole (e-hole) pairs rather than e-ion pairs. Furthermore, the fundamental differences between the two types of detectors make semiconductor devices more attractive in some cases.

Semiconductors possess electrical conductivity and have higher mass densities than gases leading to higher neutron absorbency per unit length. Good electrical conductivity leads to lower biasing voltages and thus more compact designs. Semiconductor detectors generate signals directly by e-hole separation and charge collection.

E-hole pair generation in a semiconductor requires a certain minimum amount of energy which is the semiconductor's bandgap energy. However the average required energy is about 2.5 to 3 times of the semiconductor's band-gap energy. The band-gap energy is the difference between two energy bands referred to as the valance and conduction bands.

Semiconductor conductivity can be controlled by doping[1]. Doping comes in two forms reflecting the majority charge carriers: *p* for positive doping is the implantation of impurities through which the lattice modification produces an electron accepting medium in the impurity's locality, and *n* for negative doping produces an electron donating medium. In some cases unintentional impurities are present, such impurities may provide charge-trapping sites preventing charges from being collected, thus degrading the detector's energy resolution.

For neutron detection, semiconductors may be coated or impregnated with a NCM, or the semiconductor can be pillared or layered within the NCM. Also, the semiconductor may be the NCM itself as is the case for a proposed h-BN detector to be fabricated at TTU.

Section 1.2: Boron Nitride

Graphitic and Pyrolytic h-BN

This study focuses on the hexagonal form also known as graphitic h-BN (g-BN). The graphitic form has a structure similar to graphite with alternating boron and nitrogen atoms on the hexagonal rings in each layer forming a plane of connected hexagonal rings with a single common BN molecule between contiguous rings as shown in Fig. 1-3. The hexagonal ring planes are held together by van der Waals forces. Graphitic-BN is thermodynamically stable and high quality crystals can be manufactured through CVD or by crystallization from a molten nickel chromium solution using h-BN powder as the solute (Kubota et al, 2008).

Pyrolytic h-BN is a polycrystalline formed of microscopic planes directed haphazardly throughout the entire mass; its microscopic crystals or grains are randomly oriented.

The term single crystal refers to macroscopic ordered sets of parallel planes reaching dimensions of millimeters (Kubota et al, 2008); Fig. 1-3 is an example. Single g-BN crystals are the goal of the effort within the ChE Department at KSU and may be a suitable material for neutron detection with semiconductor properties. However, the charged particles resulting from reactions presented by Eq. 1-1.2 travel through the BN medium from plane to plane displacing

[1] Implantation of impurities by various techniques

individual atoms causing damage to the lattice along their paths. Such damage changes the electrical properties of BN single crystals and altering the crystal's quality and determining a device's lifetime.

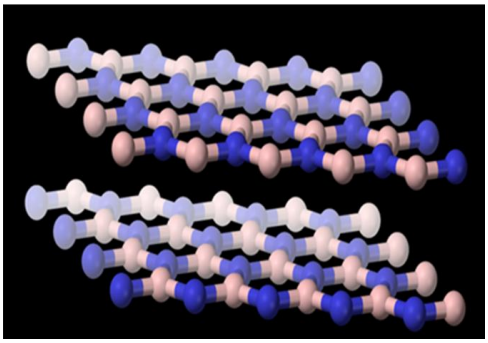

Figure 1-3: Lattice structure of g-BN (Contributors, 2012).

Macroscopic Cross-Section (Σ) and Neutron Absorption of h-BN

Natural boron consists of 19.8% ^{10}B and 80.2% ^{11}B by mass; however the ^{10}B fraction $\equiv f_{^{10}\mathrm{B}}$ can be increased by enrichment. The macroscopic neutron cross-section of ^{10}B in a medium is given by

$$\Sigma(E) = \frac{\rho_{^{10}\mathrm{B}}\sigma(E)\mathrm{A_V}}{10.013}\times 10^{-24}\ \mathrm{cm}^{-1} \qquad 1\text{-}2.1$$

where ρ_{10_B} is the overall mass density of ^{10}B in g/cm^3 within the medium, σ is the microscopic neutron cross-section of ^{10}B in barns, E is neutron energy, $\mathrm{A_V}$ is Avogadro's number whose value is 6.022×10^{23} atoms mole^{-1}, 10.013 is the atomic mass of ^{10}B in grams mole^{-1}, and 10^{-24} is the barn to cm^2 conversion factor.

The mass density of ^{10}B in a medium is determined by dividing the total mass of ^{10}B present in the medium by the total volume of the medium. One mole of h-BN made with natural boron with a molar mass of 24.82 g/mole and a density of 2.1 g/cm^3 implying the volume is 11.819 cm^3/mole which does not vary with $f_{^{10}\mathrm{B}}$.

The average molar mass of boron $\equiv \bar{\mathrm{A}}_\mathrm{B}$ as a function of $f_{^{10}\mathrm{B}}$ is represented by

$$\bar{\mathrm{A}}_\mathrm{B} = f_{^{10}\mathrm{B}}(10.013)\ \mathrm{g/mole} + \left(1 - f_{^{10}\mathrm{B}}\right)(11.009)\,\mathrm{g/mole} \qquad 1\text{-}2.2$$

and the density of ^{10}B can be written as

$$\rho_{10_B} = \frac{f_{10_B}\bar{A}_B}{11.819} \text{ g/cm}^3 . \quad 1\text{-}2.3$$

Substituting Eqs. 1-2.2 and 1-2.3 into Eq. 1-2.1 leads to

$$\Sigma_{\text{h-BN}}\left(\sigma(E_n), f_{10_B}\right) = 5.094\times10^{-3}\sigma(E)\left(11.009 f_{10_B} - f_{10_B}^2\right) \text{ cm}^{-1} \qquad 0 \le f_{10_B} \le 1 \quad 1\text{-}2.4$$

where all units with the exception of cm^{-1} cancel and $\sigma(E)$ is the numerical value of the microscopic cross-section of ^{10}B at a certain neutron energy *E*. Eq. 1-2.4 provides a simplified function for the macroscopic cross-section for any h-BN mass as long as the ^{10}B enrichment fraction and the neutron energy are known and is useful in Monte Carlo coding.

The intensity of unabsorbed neutrons transmitted through a medium with absorption cross section Σ_a is given by

$$N = N_o e^{-\Sigma_a t} \quad 1\text{-}2.5$$

where N_o is the intensity of impinging neutrons onto the medium and *t* is the medium's thickness. The absorbed portion of neutrons N_a is simply *N* subtracted from N_o or

$$N_a = N_o\left(1 - e^{-\Sigma_a t}\right) . \quad 1\text{-}2.6$$

Therefore the absorbed fraction f_a is

$$f_a(\Sigma, t) = 1 - e^{-\Sigma_a t} \quad 1\text{-}2.7$$

and asymptotically approaches unity as either Σ_a or *t* or both simultaneously increase.

Section 1.3: Research Scope

The overall goal of the collaboration is to test the suitability of h-BN for neutron detection. Key to the study is the use of high crystal quality material with low residual impurity concentrations in order to achieve best electrical properties. Radiation damage investigation on pyrolytic h-BN and detector assessment takes place at KSU.

Motivation

One way of fabricating a BN semiconductor neutron detector is by depositing h-BN on a semiconductor substrate such as silicon or gallium arsenide. Neutron conversion takes place in the h-BN layer and the emitted charged particles travel and exit the h-BN, which is the NCM,

striking the semiconductor and depositing the remaining energy generating e-hole pairs which are collected by the bias voltage to generate a signal; diode and pillar based designs have been implemented (Osberg et al, 2007), (Osberg et al 2006). However, such designs suffer from conflicting requirements arising from necessary design parameters: the thicker the NCM the more neutron conversion as Eq. 1.7 shows, yet the thicker the NCM the less energy deposition in the semiconductor due to energy loss of the resulting particles travelling longer distances in the NCM. If the NCM is sufficiently thick, the particles reaching the semiconductor have little or no energy, resulting in weak or lost signals. On the other hand, a thinner NCM results in less neutron absorbency as Eq. 1-1.7 shows and more energy deposition in the semiconductor as shown in Fig. 1-2. Therefore, a design which employs the medium simultaneously as the NCM and the semiconductor mitigates the conflict in requirements and optimizes both neutron absorption and energy deposition in the semiconductor.

Detector Fabrication at TTU

TTU's efforts are focused on the construction of a neutron detector where the NCM—*n*, or *p* doped h-BN—is the semiconductor, enabling e-hole pair generation and collection within the NCM mitigating the conflict between the energy deposition and range parameters. In principle, a BN semiconductor detector could result in a higher, and possibly complete, neutron absorption and energy deposition, as shown in Fig. 1-4.

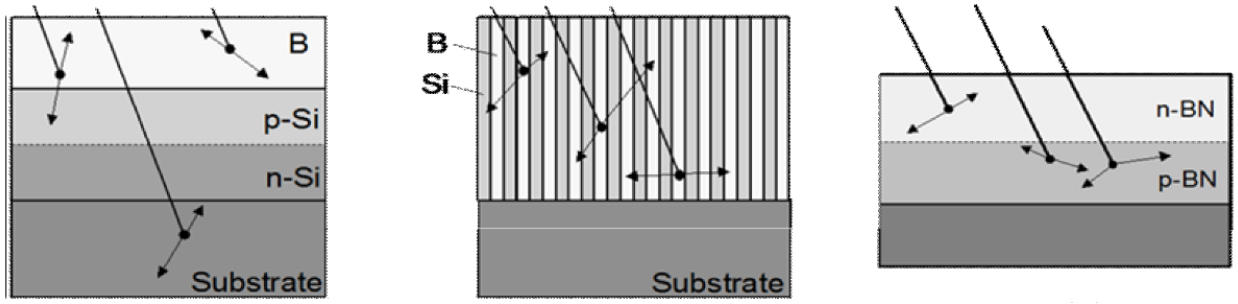

(a) (b) (c)

Figure 1-4: (a)- BN or boron on a silicon *pn* junction, the resulting particles have to travel through the h-BN in order to reach the semiconductor. In some cases the particles do not travel in the semiconductor's direction and in most cases the particles reaching the semiconductor have a fraction of the initial energy. (b)- BN or boron pillared between silicon pillars still suffers from particles having to travel through the h-BN before reaching the semiconductor. (c)- the proposed detector with the BN *pn* junction where the particles are generated within the h-BN and generate e-hole pairs within the h-BN which is the semiconductor.

Crystal Growth and Detector Assessment

The ChE Team at KSU is investigating the crystallization of h-BN from molten metal solutions for neutron detection purposes. Thus far, large single crystals have been grown which seem promising as detector crystals from a materials perspective. However the crystals are extremely thin, brittle, and delicate and easily destroyed—shattered—during detector fabrication.

The MNE Team is:

- fabricating and assessing detectors fashioned from h-BN crystals/samples.
- assessing a detector fabricated at TTU.
- conducting experiments to determine the extent of radiation damage in pyrolytic h-BN. Radiation damage experiments are based on neutron fluence to estimate the lifetime of BN detectors by conductivity and band-gap measurements.
- Using Mote Carlo methods for MCA spectrum prediction of h-BN devices

Chapter 2 - Theoretical Considerations

The proposed detector in Fig. 1-4, (c), is a design employing doped g-BN as the NCM for improved charge transport properties which could eliminate the conflict between range and energy deposition requirements. In essence, if the NCM is a semiconductor with adequate charge transport properties, there will be less restriction on the NCM's thickness which may be grown to reach tens of microns allowing, in principle, almost 90% neutron absorption. Furthermore every absorbed neutron would generate a detectable signal.

Section 2.1: Semiconductors

Semiconductors are a group of materials having conductivities between metals and insulators. There are two general classifications of semiconductors: elemental semiconductors such as silicon and germanium, found in group IV of the periodic table, and compound semiconductors formed from special combinations of elements such as gallium arsenide and indium phosphide. Semiconductors in general have band-gap energies anywhere between 0 and 3 eV. Hexagonal-BN is a compound formed from the group III element boron and the group V element nitrogen and has a band-gap energy of 5.76 eV. However, boron nitride electrical properties may be improved via doping.

Up to this point in the research conducted at KSU and TTU, a *pn* doped BN detector has not yet been fabricated; future efforts should include the use of doped h-BN which may exhibit electrical properties characteristic of semiconductors. However, in order to provide some basis to the concepts by which semiconductors are rendered useful as neutron detectors, a general independent introductory discussion on semiconductors is necessary. The discussion will introduce crystalline, polycrystalline, and disordered solid structures and a basic crystallography approach with the application of Miller plane indices.

To establish a fundamental understanding of charge transport and band structures a brief description of crystalline structures follows. The following discussion terminates with the extraction of the band-gap energy from the Kronig-Penney model and a simple explanation of how the model would apply to disordered solids. Furthermore, the discussion is general and does

not refer to any specific semiconductor unless an example is needed. Detailed reading on subsequent topics such as electron effective mass, the Fermi-Dirac distribution and statistics, charge carrier transport phenomena, and semiconductor devices can be found in (Neamen, 1992), or other introductory semiconductor texts.

The Crystalline Structure of Solids

There are three general types of solids: amorphous, polycrystalline, and crystalline. Each of the solid types is characterized by the size of ordered regions within the material, the spatial volume through which atoms or molecules have a clear periodic arrangement defined by a lattice characteristic of the solid. In amorphous solids, the periodicity of the structure only extends to within a few molecular dimensions. In polycrystalline solids, ordered regions (grains) span many atomic or molecular dimensions and vary in size and orientation with respect to each other. In crystalline solids, order extends throughout the material's volume and the entire volume is a single-crystal. Figure 2-1 is a two-dimensional depiction of the three solid structures.

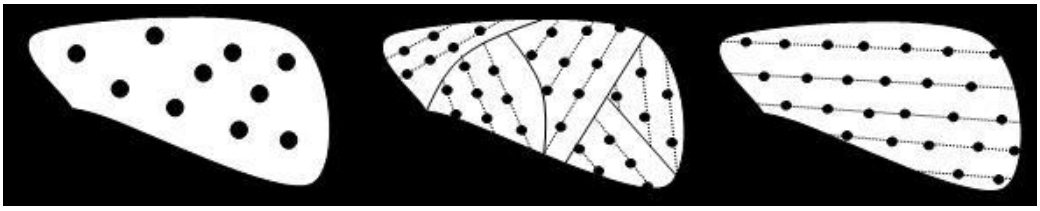

(a) (b) (c)

Figure 2-1: (a) amorphous, (b) polycrystalline, and (c) single-crystal or crystalline.

The advantage of single-crystal or crystalline materials is, in general, crystalline materials' charge transport properties are superior to the charge transport properties of polycrystalline and amorphous solids. Due to the predominance of crystalline materials in the semiconductor application and research areas, the mathematical approach in this chapter applies to single-crystal regions; "band structure and charge transport are not understood in disordered solids…but rather modeled." (Baranovski, 2006)

Lattices

Most crystalline or single-crystal regions in polycrystalline materials possess *spatial periodicity* or *translational symmetry*, and the entire volume of a single-crystal can be retrieved

by the repetition of a building block called the *basis* (Galperin, 1994) or *unit cell* (Neamen, 1992). Because the three dimensional lattice is a periodic repetition of a group of atoms there is no need to consider the entire volume of the crystal in order to represent the crystal. Among the numerous possible types of lattices, the hexagonal lattice is most important as far as h-BN is concerned, but a simple example of a generalized unit cell would be a starting point.

Figure 2-2 shows a basic two dimensional lattice as a base for a three dimensional unit cell. The relationship between the unit cell and the lattice can be characterized by the three lattice constants *a*, *b*, and *c* shown in Fig. 2-2, where every lattice point in the three dimensional crystal can be found using the vector $\vec{r} = p\vec{a} + q\vec{b} + s\vec{c}$ where *p*, *q*, and *s* are integers (Neamen, 1992) and $\vec{a}$, $\vec{b}$, and $\vec{c}$ are the lattice vector constants.

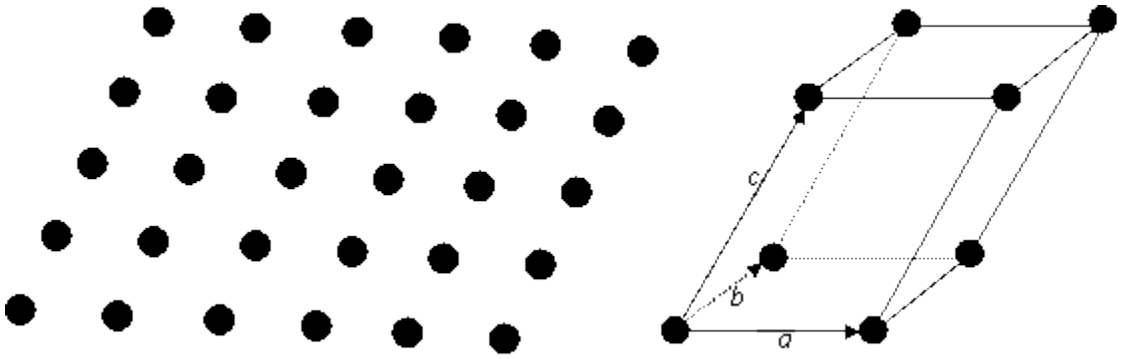

Figure 2-2: A two dimensional single-crystal lattice and a three dimensional generalized unit cell.

The hexagonal lattice system is presented in Fig. 2-3 where the relation $\vec{r} = p\vec{a} + q\vec{b} + s\vec{c}$ still applies and $\vec{a} = \vec{b} \neq \vec{c}$.

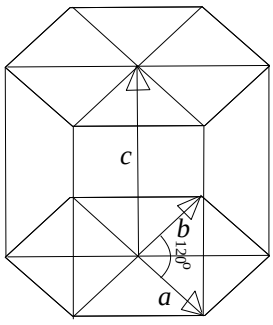

Figure 2-3: The primitive cell in the hexagonal system (Kittel, 1996) showing the relation to g-BN in Figure 1-3.

Crystal Planes and Miller Indices

The structures defined in the previous subsection are the basis needed to reconstruct the crystal. However, crystals are not infinite and must end at certain points in space defining their volume, shape, and the electrical properties of their surfaces. Semiconductor devices are fabricated at or near crystal surfaces and the properties of the crystal's surface influence the device's operational characteristics (Neamen, 1992). Surfaces on or planes through crystals can be described by considering the intercepts of the plane along the $\vec{a}$, $\vec{b}$, and $\vec{c}$ axes and the integer multipliers *p*, *q*, and *s*. Figure 2-4 shows a plane intersecting the $\vec{a}$, $\vec{b}$, and $\vec{c}$ axes at *p*, *q*, and *s* equal to (1, 2, 2) from which the Miller indices for the plane will be derived as an example and Fig. 2-5 shows the (100), (010), (001), and the (110) planes.

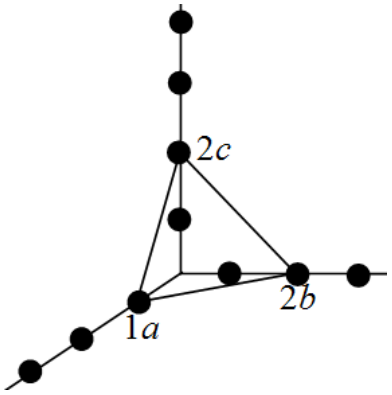

Figure 2-4: A plane intersecting an arbitrary set of axes at p, q, and s equal 1, 2, and 2, respectively.

If one takes the reciprocals of the intercepts in Fig. 2-4, $(1/1,1/2,1/2)$, and then multiplies by the least common denominator, 2, one obtains the set of numbers (2,1,1) and the plane is referred to as the (211) plane; any plane with similar indices is parallel to the plane used to obtain the indices. The axes can be in any direction as long as they form a basis set, and the vectors lengths do not have to be equal but the chosen units must hold in ensuing calculations.

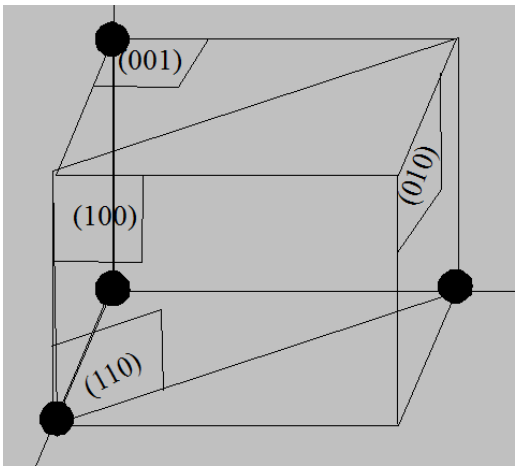

Figure 2-5: The (100), (010), (001), (110) planes.

Miller indices are a means of determining the nearest distance between equivalent parallel planes and the surface atom density per unit area cut by a particular plane. The parameters are important in determining how two different materials will fit one another across their interface when joined. Furthermore, when a crystal is physically cut, analogous to a plane cutting through the crystal to expose a surface, the electrical properties at the surface are defined by the lattice structure and the broken chemical bonds at the surface.

Structural Imperfections and Impurities in Crystals

So far the discussion has covered perfect crystals; in reality, crystals are not perfect, but contain structural defects and impurities. Both structural defects and impurities or dopants affect the crystal's electrical properties.

Structural Imperfections

The point defect is a structural defect characterized by two distinct forms. The first is a missing atom from a particular lattice site referred to as a *vacancy point defect*; the second is an atom located between lattice sites referred to as an *interstitial point defect*. In both cases the perfect geometrical arrangement of the atoms in the lattice and the chemical bonding is disrupted producing localized electrically different properties. The *Frenkle defect* consists of a vacancy and an interstitial in close proximity. A *line defect* is where a partial or entire row of atoms is missing or displaced. The *plane defect* can be visualized as line defect spreading across a region within the crystal as shown in Fig. 2-6 (b).

In disordered solids, the concentration per unit volume of structural defects is high and randomly distributed in size, area, and direction. The defects crisscross each other throughout the solid, warping and deforming each other and the electrical properties vary on a scale of atomic distances. Thus a disordered solid is a material which neither has the structure of a perfect lattice nor the structure of a crystal lattice with isolated defects as shown in Fig. 2-6 (a) and (b).

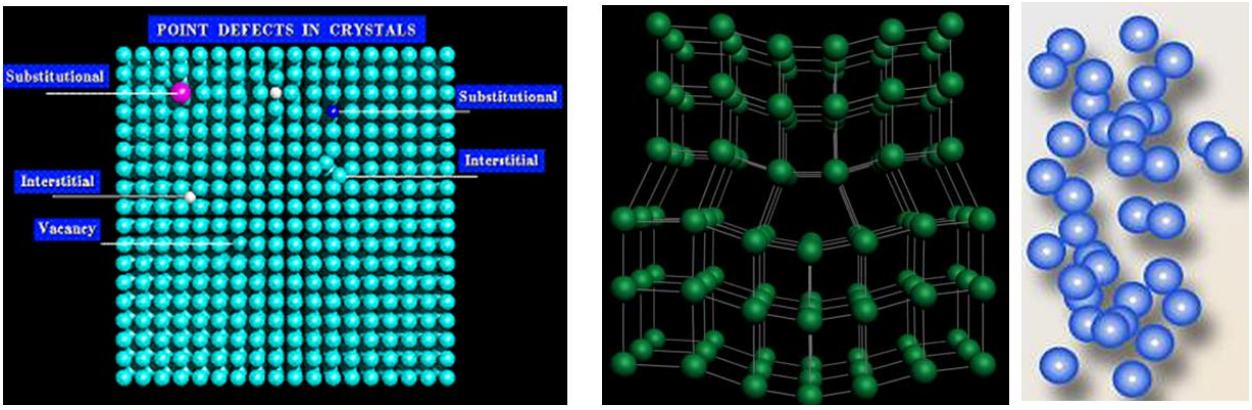

(a) (b) (c)

Figure 2-6: (a)-Point defects in a plane within a crystal lattice (Universe, 2008). (b)-The plane (NDT Resource Center, 2012) in the center may be viewed from two different perspectives, interstitial plane (lower half) or vacancy plane (upper half), depending on the predominant structure of the crystal. (c)-The structure of a disordered solid (SOLIDSONLINE, 2011) a deformed crystal lattice as plane and other defects warp and crisscross each other distorting the crystal lattice and varying the crystal's electrical properties on the order of atomic distances.

When a crystal is cut whether physically or by an imaginary designated plane such as the (110) plane cutting the body-centered cubic lattice in Fig. 2-7 (left) a pattern of the cut atoms shown in Fig. 2-7 (right) emerges, the pattern is repeatable on the entire plane's surface with the exception of localities where defects are present as shown by a vacancy point defect.

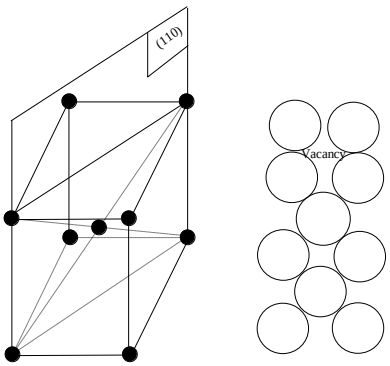

Figure 2-7: A face-centered cubic lattice cut by the (110) plane

As earlier mentioned crystals are not infinite and for simplicity an assumption is made where in the interior of a crystalline solid all valence electrons are strongly bound; the strengths (energy) of the bonds vary based on localized structural parameters and defects. On the surface of a crystal, depending on the crystal's atomic composition, ionic or covalent bonds are broken leaving weakly bound electrons behind.

Impurities

Impurities are unavoidable even in the purest of materials. Impurities located in the place of atoms at lattice sites are referred to as *substitutional impurities* and impurities located in-between lattice sites and are referred to as *interstitial impurities*. Some impurities such as oxygen in silicon are inert and tend to have no effect on the crystal's electrical properties. Gold and phosphorous on the other hand can drastically change the crystal's electrical properties (Neamen, 1992). Silicon was used as an example to demonstrate the effect of impurities; ultimately, the overall electrical properties are a function of the material and the impurity.

Quantum Mechanics

Discussing semiconductors and their behavior and how they apply to neutron detection directly would seem ideal. However, prior to describing in detail the events leading to neutron detection, a fundamental understanding of the behavior and motion of charge in semiconductors should be established through quantum mechanics, for the electrical properties of semiconductors are directly related to the behavior of electrons in the crystal lattice and the potentials therein. The behavior and characteristics of these electrons can be described by the formulation of quantum mechanics called wave mechanics using Schrödinger's wave equation.

The Basis of Quantum Mechanics

Prior to presenting Schrödinger's wave equation the basic principles of quantum mechanics are briefly introduced: the principle of energy quanta, the wave-particle duality principle, and the uncertainty principle.

- **The Principle of Energy Quanta**

In 1900 Max Planck postulated *quanta* as thermal radiation being emitted from a heated surface in discrete packets. In 1905 Albert Einstein explained the results of the photoelectric effect by introducing *photons* as the energy in a light-wave contained in discrete packets, where the photon's energy must be enough to unbind an electron from the surface of a metal where the minimum of the energy needed is referred to as the material's *work-function*. Unless equal to the next needed level of energy to emit a more strongly bound electron, any energy in excess of the material's work-function will be manifested as the kinetic energy of the electron. Both Plank and Einstein deduced $E = hv$ as the energy contained in the photons, where h is Plank's constant and is equal to 6.625×10^{-34} J-s, and v is the frequency of the electromagnetic wave.

- **The Wave-Particle Duality**

In 1924 Louis-Victor-Pierre-Raymond, 7th duc[2] de Broglie postulated the relation between a wave and a particle in motion as a relation of reciprocation and because waves, which are energy in motion, behaved as particles, then moving particles should manifest wave-like behavior. The reciprocation is described as the momentum, p, of a photon is given by h/λ where λ is the wave's wavelength, then the wavelength, λ, of a particle in motion should be h/p. The wave-particle duality is proven by the diffraction of moving sub-atomic particles, and is the basis for many applications, including neutron diffraction to achieve a monoenergetic beam of thermal neutrons.

- **The Uncertainty Principle**

The first two principles of quantum mechanics are definitive and absolute, but certain experimental results on small subatomic particles do not agree with Newtonian physics applied on large objects such as planets, falling objects, and speeding bullets.

In 1927 Werner Heisenberg announced the Uncertainty Principle which in the most succinct terms states: *the more precisely the position of a particle is determined, the less precisely the momentum is known in the instant the position was observed, and vice versa*, or in

[2] French for duke

mathematical terms $\Delta p\ \Delta x \geq \hbar$ where $\hbar$ is $h/2\pi$ and Δp and Δx are the uncertainties in the particle's momentum and position, respectively. The second statement of the principle, which can be directly derived from the first, states: *it is impossible to simultaneously describe with absolute accuracy the energy of a particle and the instant of time the particle had the energy, and vice versa* which in mathematical terms is given as $\Delta E\ \Delta t \geq \hbar$ where ΔE and Δt are the uncertainties in the particle's energy and the uncertainty in the time at which the particle's energy was measured, respectively.

Schrödinger's Wave Equation.

Schrödinger's wave equation, a basic postulate of quantum mechanics (Neamen, 1992) can be written in one spatial dimension x

$$\frac{-\hbar^2}{2m}\frac{\partial^2\Psi(x,t)}{\partial x^2}+V(x)\Psi(x,t)=i\hbar\frac{\partial\Psi(x,t)}{\partial t} \quad , \qquad 2\text{-}1.1$$

where $\Psi(x,t)$ is the one-dimensional wave function, $V(x)$ is the one-dimensional time independent potential function, m is the particle's mass, and i is the complex variable $\sqrt{-1}$. The three dimensional form of Schrödinger's wave Eq. involves the three Cartesian directions x, y, and z, and can also be represented in cylindrical and spherical coordinate systems. The solution to the one-dimensional non-relativistic Schrödinger's wave Eq. is sufficient to demonstrate the basic ideas and the statistical nature of charge transport mechanisms.

The first step in solving Eq. 2-1.1 is the separation of the functions of the constituent independent variables x and t as shown in Eq. 2-1.2 (Griffiths, 2005).

$$\Psi(x,t)=\psi(x)\phi(t) \qquad 2\text{-}1.2$$

Where $\psi(x)$ and $\phi(t)$ are the independent position and time functions, respectively. The substitution of Eq. 2-1.2 into Eq. 2-1.1 yields the complete derivative .

$$\frac{-\hbar^2}{2m}\phi(t)\frac{d^2\psi(x)}{dx^2}+V(x)\psi(x)\phi(t)=i\hbar\psi(x)\frac{d\phi(t)}{dt} \qquad 2\text{-}1.3$$

Dividing Eq. 2-1.3 by $\psi(x)\phi(t)$ yields

$$\frac{-\hbar^2}{2m}\frac{1}{\psi(x)}\frac{d^2\psi(x)}{dx^2}+V(x)=i\hbar\frac{1}{\phi(t)}\frac{d\phi(t)}{dt} \qquad 2\text{-}1.4$$

The left hand side (LHS) and the right hand side (RHS) of Eq. 2-1.4 are functions of *x* and *t*, respectively. Thus, each side must be equal to a constant referred to as the separation constant denoted by η. Equating the RHS or the time-dependent portion of Eq. 2-1.4 to η gives

$$i\hbar \frac{1}{\phi(t)} \frac{d\phi(t)}{dt} = \eta \qquad 2\text{-}1.5$$

which can be solved to yield

$$\phi(t) = e^{-i(E/\hbar)t} \qquad 2\text{-}1.6$$

.

The introduction of the term *E*—energy—into Eq. 2-1.6 must be justified before moving further. The form of Eq. 2-1.6 is the classical exponential solution of the sinusoidal wave where $\eta/\hbar$ is the angular frequency ω and the energy $E=h\nu=h\omega/2\pi$. Thus $\omega= \eta/\hbar= E/\hbar$ and so the separation constant is the total energy of the particle and the LHS of Eq. 2-1.4 is equal to the particle's total energy *E* as shown below

$$\frac{-\hbar^2}{2m} \frac{1}{\psi(x)} \frac{d^2\psi(x)}{dx^2} + V(x) = E \qquad 2\text{-}1.7$$

.

through simple algebraic manipulation Eq. 2-1.7 becomes

$$\frac{d^2\psi(x)}{dx^2} + \frac{2m}{\hbar^2}\left(E - V(x)\right)\psi(x) = 0 \qquad 2\text{-}1.8$$

where *E* is the total energy—kinetic + potential—in the system and is known as the Hamiltonian operator(Griffiths, 2005).

As for the physical meaning of the wave Eq. and ultimately the description for the behavior of an electron in a crystal, Eq. 2-1.6 can be substituted in Eq. 2-1.2 to yield the complex function

$$\Psi(x,t) = \psi(x) e^{-i(E/\hbar)t} \qquad 2\text{-}1.9$$

.

Because Eq. 2-1.9 is complex, the validity of a physically tangible solution seems absurd. However, in 1926 Max Born postulated the function $\left|\Psi(x,t)\right|^2$ as the probability density function of finding the electron between *x* and *x* + *dx* (Neamen, 1992). Because Ψ is a complex-valued function, then

$$\Psi(x,t)\Psi^*(x,t) = \left|\Psi(x,t)\right|^2, \qquad 2\text{-}1.10$$

where $\Psi^*(x,t) = \psi^*(x)e^{+i(E/\hbar)t}$ and is the complex conjugate of $\Psi(x,t)$. Clearly by performing the operation in Eq. 2-1.10 the result is

$$\left|\Psi(x,t)\right|^2 = \psi(x)\psi^*(x) = \left|\psi(x)\right|^2, \qquad 2\text{-}1.11$$

where $\left|\psi(x)\right|^2$ is the electron's position probability density function (pdf). Eq. 2-1.11 expresses a key difference between classical and quantum mechanics and supports the validity of the uncertainty principle.

The electron's pdf must be normalized such that

$$\int_{-\infty}^{+\infty}\left|\psi(x)\right|^2 = 1. \qquad 2\text{-}1.12$$

Equation 2-1.12 is one boundary condition which allows the determination of the wave function's coefficients. The other boundary conditions which must be imposed are the wave function and the resulting first derivative must have the following two properties if the total energy *E* and the potential function *V*(*x*) are finite everywhere; i.e. $\psi(x)$ and $d\psi(x)/dx$ must be continuous, finite, and single valued.

Solving Schrödinger's Wave Equation.

Solving Schrödinger's Eq. using several examples with different constant potential functions provides an indication of the behavior of electrons under the influence of the different potentials and the electrons' total energy. The results will be used to describe the general behavior and electrical properties of semiconductors.

- **The Electron in Free Space**

The electron in free space example represents an unbounded electron with a constant potential function. The total energy *E* of the electron must be greater than the potential function or otherwise the electron would be bounded. Furthermore, with *E* > *V*(*x*), from Eq. 2-1.8 $E - V(x)$ represents a net energy, if *V*(*x*) is constant. For simplicity, *V*(*x*) will be assumed to be zero and Eq. 2-1.8 becomes Eq. 2-1.13, which is the time independent portion of Eq. 2-1.2.

$$\frac{d^2\psi(x)}{dx^2} + \frac{2Em}{\hbar^2}\psi(x) = 0. \qquad 2\text{-}1.13$$

The solution to Eq. 2-1.13 is

$$\psi(x) = Ae^{\left[\frac{ix\sqrt{2mE}}{\hbar}\right]} + Be^{\left[\frac{-ix\sqrt{2mE}}{\hbar}\right]} \quad \text{2-1.14}$$

Eq. 2-1.13 can be represented in sines and cosines and the time independent solution will not be affected. However, the time dependent portion, $\phi(t)$, has an exponential solution, Eq. 2-1.6, and the substitution of Eq. 2-1.14 into Eq. 2-1.9 simply makes the algebra easier and results in the following

$$\Psi(x,t) = Ae^{\left[\frac{i}{\hbar}\left(x\sqrt{2mE}-Et\right)\right]} + Be^{-\left[\frac{i}{\hbar}\left(x\sqrt{2mE}-Et\right)\right]} \quad \text{2-1.15}$$

Equation 2-1.15 describes a travelling wave representing a moving electron in free space. The term with coefficient *A* is a wave travelling in the +*x* direction and the portion with the coefficient *B* represents a wave travelling in the –*x* direction. Imposing boundary conditions by which the electron is travelling in the +*x* direction, then *B* must be zero; the reverse is also true. Thus for the electron travelling in the +*x* direction Eq. 2-1.15 becomes

$$\Psi(x,t) = Ae^{\left[\frac{i}{\hbar}\left(x\sqrt{2mE}-Et\right)\right]} \quad \text{2-1.16}$$

Referring back to the wave-particle duality principle and setting the wave number $k = 2\pi/\lambda$, and as earlier shown $\omega = E/\hbar$ by replacing *i* with *j* Eq. 2-1.16 reduces to

$$\Psi(x,t) = Ae^{\left[j(kx-\omega t)\right]} \quad \text{2-1.17}$$

Thus a free particle with a well defined function has well defined wavelength and momentum, but the probability density function $\Psi(x,t)\Psi^*(x,t) = AA^*$ is a constant independent of position, and thus the particle may be found anywhere. The reasoning is in agreement with the uncertainty principle. A localized free particle is defined by a wave packet, formed by a superposition of wave functions with different momentum or *k* values. The mathematics of wave packets will not be investigated further in this work.

- **The Electron in an Infinite Potential Well**

The electron in free space example effectively demonstrated the application of Schrödinger's Eq. and the three principles of quantum mechanics. The electron in an infinite

potential well represents a strongly bound particle— an electron. The potential function of the infinite well is shown in Fig. 2-8.

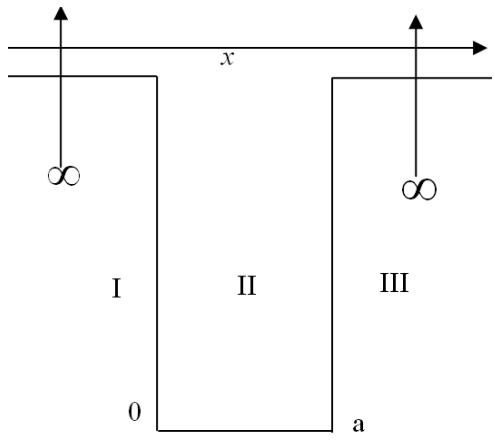

Figure 2-8: The potential function of the infinite well. The electron with finite energy is contained in and confined to the finite space of region II.

Equation 2-1.8 is the time independent portion of Schrödinger's wave Eq., where E is the electron's total energy and $V(x)$ is the potential. Due to the electron's confinement in region II the wave function $\psi(x)$ in regions I and III must be zero simply because the electron's energy is finite and the potential is infinite. However, the potential in region II is zero and Eq. 2-1.8 can be rewritten as

$$\frac{d^2\psi(x)}{dx^2}+\frac{2Em}{\hbar^2}\psi(x)=0 \qquad \text{2-1.18}$$

the solution is given by

$$\psi(x)=C_1\cos\left(\sqrt{\frac{2mE}{\hbar^2}}x\right)+C_2\sin\left(\sqrt{\frac{2mE}{\hbar^2}}x\right) \qquad \text{2-1.19}$$

by equating K to $\sqrt{2mE/\hbar^2}$, Eq. 2-1.19 can be presented as

$$\psi(x)=C_1\cos(Kx)+C_2\sin(Kx) \qquad \text{2-1.20}$$

As earlier stated, the wave function in regions I and III must be zero; therefore, due to the required continuity, the wave function must be zero at the inside edges of the potential well where $x = 0$, and $x = a$. Imposing the mentioned boundary conditions on Eq. 2-1.20, then C_1 must equal zero rendering $\psi(x)=0$ at x=0; as for the second boundary at a the trivial solution is of course $C_2 = 0$. However, with $C_1 = 0$ Eq. 2-1.20 becomes

$$\psi(x) = C_2 \sin(Kx) = 0 \qquad \text{2-1.21}$$

and solutions other than $C_2 = 0$ at a are all K values rendering $sin(Ka) = 0$, for a is constant. For the sine function to equal zero the argument must be an integral multiple of π and implies

$$Ka = n\pi \qquad \text{2-1.22}$$

or

$$K = \frac{n\pi}{a} \qquad \text{2-1.23}$$

.

In order to find C_2 Eq. 2-1.21 must be normalized as shown in Eq. 2-1.24

$$\int_0^a C_2^2 \sin^2(Kx)\,dx = 1 \qquad \text{2-1.24}$$

.

Evaluation of the integral in Eq. 2-1.24 and substitution of the value of K from Eq. 2-1.23 yields

$$\psi(x) = \sqrt{\frac{2}{a}} \sin\left(\frac{n\pi x}{a}\right) \qquad n = 1, 2, 3, \cdots, \infty \qquad \text{2-1.25}$$

.

Equation 2-1.25 is a standing wave in the potential versus the travelling wave of the free electron, and looking back at Eq. 2-1.23 and the earlier statement where $K = \sqrt{2mE/\hbar^2}$ as a precursor to Eq. 2-1.20, then

$$E = E_n = \frac{\hbar^2 n^2 \pi^2}{2ma^2} \qquad \text{2-1.26}$$

.

Also, in Eq. 2-1.25 K must have discrete values, implying that the total energy of the particle can only have discrete values as demonstrated by Eq. 2-1.26. The result is the quantization of the particle's energy; i.e. the energy of the particle can only have discrete values (Neamen, 1992). However, if the energy is precisely known then the momentum is precisely known and, by the uncertainty principle, the position cannot be known and the normalized form of Eq. 2-1.25 represents the probability density functions of all energies respective to the values of n. The first five energy levels with respective wave and probability functions for $a = 5$ Å are depicted in Fig. 2-9.

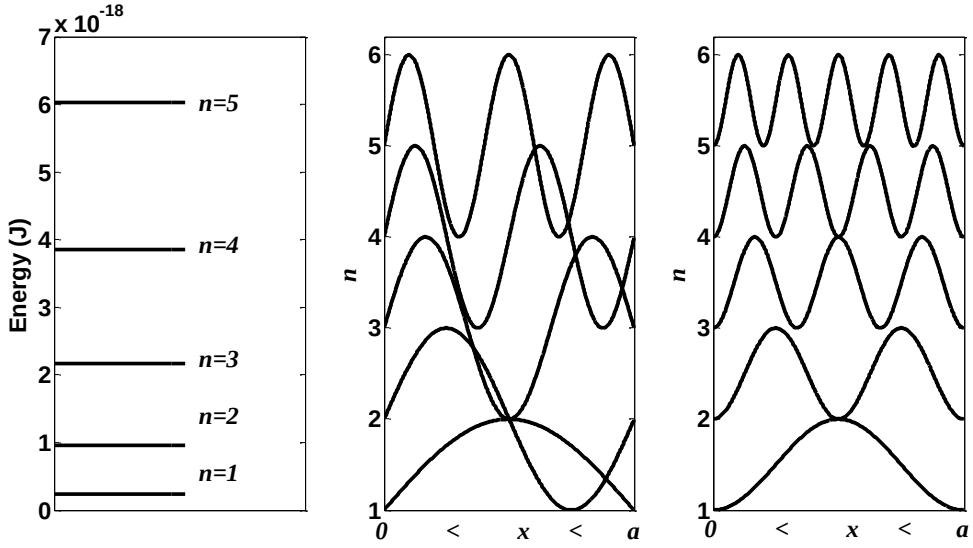

(a) (b) (c)

Figure 2-9: (a) The first 5 energy levels (b) the respective position, and (c) probability functions for $a = 5$ angstroms.

- **The Step Potential**

Previously the particle was considered to be confined between two infinite potential barriers—the infinite potential well. Infinite potential do not exist and are only of theoretical interest. A particle flux travelling from one medium to another, or through a defect within a crystal, encounters a finite potential, which may be lower or higher than the particles' total energy.

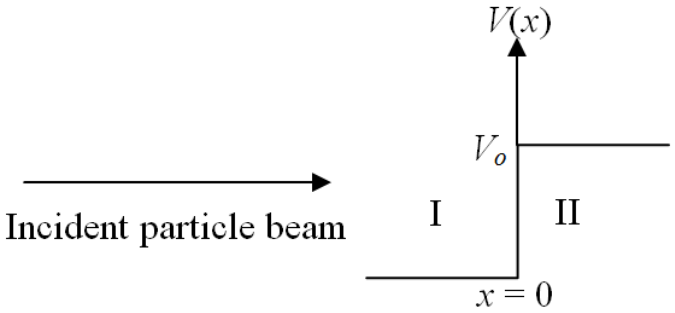

Figure 2-10: The step potential function, the potential exists in region II where $x > 0$.

In region I of Fig. 2-10, the potential V is zero and the time independent Schrödinger's Eq. for region I is

$$\frac{d^2\psi_{\mathrm{I}}(x)}{dx^2} + \frac{2Em}{\hbar^2}\psi_{\mathrm{I}}(x) = 0 \qquad 2\text{-}1.27$$

and the solution is

$$\psi_{\mathrm{I}}(x) = A_{\mathrm{I}} e^{iK_{\mathrm{I}}x} + B_{\mathrm{I}} e^{-iK_{\mathrm{I}}x} \qquad (x \le 0) \,. \tag{2-1.28}$$

The subscript I denotes the variables in Eq. 2-1.28 which are pertinent to region I, and $K_{\mathrm{I}} = \sqrt{2mE/\hbar^2}$.

In region II the potential exists and has a positive constant value V_o. The time independent Eq. for region II is given as

$$\frac{d^2\psi_{\mathrm{II}}(x)}{dx^2} + \frac{2m}{\hbar^2}(E - V_o)\psi_{\mathrm{II}}(x) = 0 \tag{2-1.29}$$

By rearranging $(E - V_o)$ into $(V_o - E)$ Eq. 2-1.29 has an exponential solution and is of the form

$$\psi_{\mathrm{II}}(x) = A_{\mathrm{II}} e^{-K_{\mathrm{II}}x} + B_{\mathrm{II}} e^{K_{\mathrm{II}}x} \qquad (x \ge 0) \,, \tag{2-1.30}$$

where $K_{\mathrm{II}} = \sqrt{2m(V_o - E)/\hbar^2}$, and boundary conditions force the solution to remain finite rendering $B_{\mathrm{II}} = 0$ for $(x \ge 0)$ and the solution to Eq. 2-1.29 is

$$\psi_{\mathrm{II}}(x) = A_{\mathrm{II}} e^{-K_{\mathrm{II}}x} \qquad (x \ge 0) \,. \tag{2-1.31}$$

The boundary conditions necessary to solve for the coefficients $A_{\mathrm{I}}, B_{\mathrm{I}}$, and A_{II} are: at x = 0 both ψ_{I} and ψ_{II} must be equal and their derivatives must be equal in order for the total wave function to be continuous. So at x = 0

$$A_{\mathrm{I}} + B_{\mathrm{I}} = A_{\mathrm{II}} \,, \tag{2-1.32}$$

and the derivatives being equal at x = 0 yields

$$iK_{\mathrm{I}}A_{\mathrm{I}} - iK_{\mathrm{I}}B_{\mathrm{I}} = -K_{\mathrm{II}}A_{\mathrm{II}} \tag{2-1.33}$$

Solving Eqs. 2-1.32 and 2-1.33 for B_{I} and A_{II} in terms of A_{I}, results in

$$B_{\mathrm{I}} = \frac{-\left(K_{\mathrm{II}}^2 + 2iK_{\mathrm{I}}K_{\mathrm{II}} - K_{\mathrm{I}}^2\right)A_{\mathrm{I}}}{\left(K_{\mathrm{II}}^2 + K_{\mathrm{I}}^2\right)} \tag{2-1.34}$$

and

$$A_{\mathrm{II}} = \frac{2K_{\mathrm{I}}\left(K_{\mathrm{I}} - iK_{\mathrm{II}}\right)A_{\mathrm{I}}}{\left(K_{\mathrm{II}}^2 + K_{\mathrm{I}}^2\right)} \tag{2-1.35}$$

Derived from Eqs. 2-1.34 and 2-1.35 elsewhere (Griffiths, 2005; Neamen, 1992) is the reflectance coefficient R must be unity for particles with $E < V_0$, implying the wave is totally reflected back into region I by the step potential; yet, Eq. 2-1.31 also implies the wave's existence in region II, as by Eq. 2-1.32 A_{II} is not zero. The result implies that there is a probability where a particle in region I moving towards region II would penetrate the barrier into region II. Even though the probability of a particle with $E < V_0$ penetrating from region I into region II exists, the reflectance coefficient is still unity indicating that any particle which does penetrate the barrier is eventually reflected back into region I in the $-x$ direction.

- **The Potential Barrier**

Of all the examples thus far, the potential barrier—depicted in Fig. 2-11—has the most significant implications in semiconductors. The mathematics involved in solving Schrödinger's equation have been demonstrated in the two previous examples; the steps for solving Schrödinger's equation, for the potential barrier are the same as the previous examples; however, they are more complex and lengthy, thus only the solutions and their meaning will be provided here.

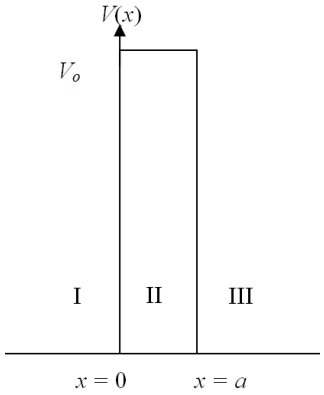

Figure 2-11: The potential barrier function.

The solutions of the wave equation for the regions I, II, and III in Fig. 2-11 are given, respectively, by (Neamen, 1992)

$$\psi_{I}(x) = A_{I}e^{iK_{I}x} + B_{I}e^{-iK_{I}x} \qquad 2\text{-}1.36$$

$$\psi_{II}(x) = A_{II}e^{K_{II}x} + B_{II}e^{-K_{II}x} \qquad 2\text{-}1.37$$

$$\psi_{III}(x) = A_{III}e^{iK_{I}x} + B_{III}e^{-iK_{I}x} \qquad 2\text{-}1.38$$

where $K_{\mathrm{I}} = \sqrt{2mE/\hbar^2}$ and $K_{\mathrm{II}} = \sqrt{2m(V_o - E)/\hbar^2}$.

The coefficient B_{III} is representative of a negative travelling wave, but there are no potentials in region III and thus a particle can never be reflected back into the potential in region III and thus B_{III} must be zero. Due to the potential barrier's finite width neither A_{II} nor B_{II} can become unbounded, and in region I both A_{I} or B_{I} must remain for the particle can be reflected as earlier demonstrated. As before, the coefficients B_{I}, A_{II}, B_{II}, and B_{III} can be determined in terms A_{I}.

Of particular interest in semiconductors is the transmission parameter[3] T defined as

$$T = \frac{A_{\mathrm{III}} \times A_{\mathrm{III}}^*}{A_{\mathrm{I}} \times A_{\mathrm{I}}^*} \quad \text{2-1.39}$$

Equation 2-1.39 implies that a particle impinging on the potential barrier in region I, has a finite probability of penetrating the barrier and appearing in region III (Neamen, 1992). This phenomenon is known as *tunneling* which what enables semiconductors to operate the way they do.

- **The Single Electron Atom**

Extending Schrödinger's wave equation to the single electron atom provides a qualitative idea of how the outermost electrons of atoms behave and their energy levels in terms of quantum numbers. For simplicity, the atom will be considered spherical and Schrödinger's Eq. in spherical coordinates is

$$\nabla^2 \Psi(r,\theta,\phi) + \frac{2m_o}{\hbar^2}\left(E - V(r)\right)\psi(r,\theta,\phi) = 0 \quad \text{2-1.40}$$

where m_o is the electron's rest mass and $V(r) = -e^2/4\pi\varepsilon_o r$ is the potential function due to the coulomb attraction between the electron and the nucleus. The negative sign is indicative of the force being inwards towards the nucleus and the electron is bound to the nucleus. Substitution of the spherical Laplacian and separating the variables r,θ,ϕ as previously demonstrated in Eq. 2-1.2 results in

[3] T is the ratio of the transmitted flux in region III to the incident flux in region I; also known as the probability of transmittance.

$$\frac{\sin^2\theta}{R}\frac{\partial}{\partial r}\left(r^2\frac{\partial R}{\partial r}\right)+\frac{1}{\Phi}\frac{\partial^2\Phi}{\partial\phi^2}+\frac{\sin(\theta)}{\Theta}\frac{\partial}{\partial\theta}\left(\sin(\theta)\frac{\partial\Theta}{\partial\theta}\right)$$
$$+r^2\sin^2\theta\frac{2m_o}{\hbar^2}(E-V)=0 \qquad \text{2-1.41}$$

.

The middle term, involving the azimuthal angle has the solution

$$\Phi=e^{im\phi}, \qquad \text{2-1.42}$$

where *m* is a separation constant, and with the imposed condition where the wave function must be single valued, *m* must be an integer where $m=0,\pm1,\pm2,\pm3,\pm4,\ldots$. The separation constants for the other two terms in Eq. 2-1.41 are *l* and *n*, where $n=1, 2, 3,\ldots$, and $l=n-1, n-2, n-3,\ldots$. "It can be shown that $|m|=l,l-1,\cdots,0$" (Donald A. Neamen, 1992). The quantities *l*, *n*, and *m* are designated as *quantum numbers*. A fourth quantum number defines the electron's spin and is designated by the symbol *s* with values of $+1/2$ and $-1/2$ (Neamen, 1992; Griffiths, 2005). Each set of allowed quantum numbers is a distinct quantum state which is a consequence of the Pauli exclusion principle[4], and the solution to the wave Eq. is designated as $\Psi_{l,m,n}$. As shown in Fig. 2-9, *n* is the principal quantum number and the electron's energy may be given as

$$E_n=\frac{-m_o e^4}{(4\pi\varepsilon_o)^2\,2\hbar^2n^2}. \qquad \text{2-1.43}$$

The derivation of how the separate quantum numbers apply to atoms with higher number of electrons is not the object of this work and the single electron atom is the simplest example and provides a qualitative idea; however, some explanation is due in order to clarify how the quantum numbers apply to the electronic configuration of the elements as the definition of energy levels and valence electrons. In Table 2-1 the quantum number *n* defines the energy level of a shell, *l* pertains to a sub-shell within the *n* energy shell and so on; *s* is the spin due to the electron's angular momentum as the electron spins on an axis.

[4] The Pauli Exclusion Principle states that, in any given system (an atom, molecule, or crystal), no two electrons may occupy the same quantum state (Griffiths, 2005).

Table 2-1: Initial portion of the periodic table (Neamen, 1992; Griffiths, 2005). Valence electrons are the electrons in the unfilled *n* energy level. Helium has the *n* level completely filled and no other electrons and thus has no valence electrons.

Element	Electronic configuration	*n*	*l*	*m*	*s*	Valence electrons
Hydrogen	$1s^1$	1	0	0	$+1/2$ or $-1/2$	1
Helium	$1s^2$	1	0	0	$+1/2$ and $-1/2$	0
Lithium	$1s^2 2s^1$	2	0	0	$+1/2$ or $-1/2$	1
Beryllium	$1s^2 2s^2$	2	0	0	$+1/2$ and $-1/2$	2
Boron	$1s^2 2s^2 2p^1$	2	1	0,-1,+1	$+1/2$, $-1/2$	3
Carbon	$1s^2 2s^2 2p^2$	2	1	0,-1,+1	$+1/2$, $-1/2$	4
Nitrogen	$1s^2 2s^2 2p^3$	2	1	0,-1,+1	$+1/2$, $-1/2$	5
Oxygen	$1s^2 2s^2 2p^4$	2	1	0,-1,+1	$+1/2$, $-1/2$	6
Fluorine	$1s^2 2s^2 2p^5$	2	1	0,-1,+1	$+1/2$, $-1/2$	7
Neon	$1s^2 2s^2 2p^6$	2	1	0,-1,+1	$+1/2$, $-1/2$	0

Quantum Theory Extended To Solids and Crystals

As shown an electron confined to a finite space within an atom can only take discrete *quantized* energy levels, and by the Pauli Exclusion Principle, no two electrons confined in an atom may have the same set of quantum numbers. The extension of *quantized* energy levels from atoms to crystal systems leads to allowed and forbidden *energy band structures*. The concept of energy band structure leads to the understanding of the electrical properties of semiconductors and will introduce the parameter known as the electron's *effective mass*. Dealing with electrons in single crystal systems implies the existence of a very large number of electrons in a finite confined space and must be approached statistically.

Energy Band Formation

Just as there are allowed and forbidden energy bands in atomic systems, allowed and forbidden energy bands exist in systems comprised of a multitude of atoms such as crystal lattices. The phenomenon arises from the close proximity of the atoms in the solid. As atoms approach each other the radial probability density functions tend to overlap. The overlapping places electrons from adjacent atoms in the same confined space. The Pauli Exclusion Principle does allow atoms in the same space to have the same quantum state—quantum number sets—; even though, the principal quantum number *n* will not change for adjacent atoms, the quantum numbers *l*, m_s and *s* cannot form the same set with the same principal energy level *n*. The changes in *l*, m_s and *s* bring about slightly different energy levels about the principal energy level, causing a split in the valence electrons' energy levels.

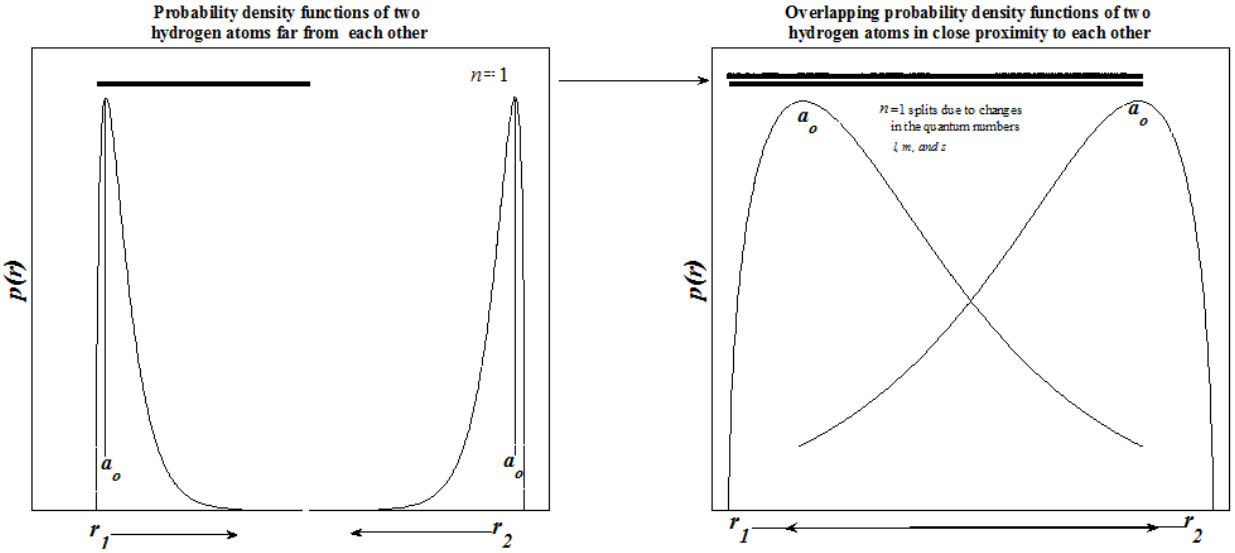

(a) (b)

Figure 2-12: (a)-The radial probability density functions of two hydrogen atoms far from each other. (b)- The radial probability density functions of two hydrogen atoms in close proximity of each other; a_o is the Bohr radius[5].

Figure 2-12 (a) shows the radial probability density function of two single electron atoms—hydrogen—sufficiently far from each other in order for neither electron to occupy the same space. Figure 2-12 (b) shows the radial probability density function of the same atoms but close enough to each other in order for the radial probability density functions to overlap. The

[5] The Bohr radius is an approximation of the distance between the nucleus—proton—of the hydrogen atom and the orbiting electron.

overlapping implies that the two electrons would, at some point, have to exist in the same finite volume causing changes—perturbations—in the quantum numbers l, m_l and s.

The splitting of energy levels due to changes in l, m_l and s does not change the principal energy level n; changes in n can only be achieved by the injection of energy from an external source such as heat or an electric field. Thus the splitting is minute about the principal energy level, and according to Fig. 2-9 there are allowed and forbidden n levels. The splitting of energy levels about n also has forbidden levels and when there are N atoms there will, at least, be N splits about n. If N is large, the forbidden and allowed states in the N splits about n are close enough to each other and the entire region may be considered as a continuous energy band as shown in Fig. 2-13. In other words, the energy needed to elevate an electron from one energy level to a higher energy level within the band is infinitesimally small. The same is true for energy lost by an electron when falling from one energy level to a lower energy level within the band. In both cases the energy is minute when N is on the order of 10^{10} or larger.

Figure 2-12 depicts the potential functions of two hydrogen atoms being drawn closer together by some imaginary force. In a real crystal adjacent atoms are intrinsically close and share valence electrons. Each atom, depending on the lattice, is surrounded by a number of other atoms; each of the surrounding atoms is in turn surrounded by a number of atoms affecting the energy levels in the initial atom. The effect propagates through the crystal, generating an energy state for each atom in the crystal. The discussion will be later extended to the valence and conduction bands, which, on a physically measurable scale, are the basis of semiconductor operation and electrical properties.

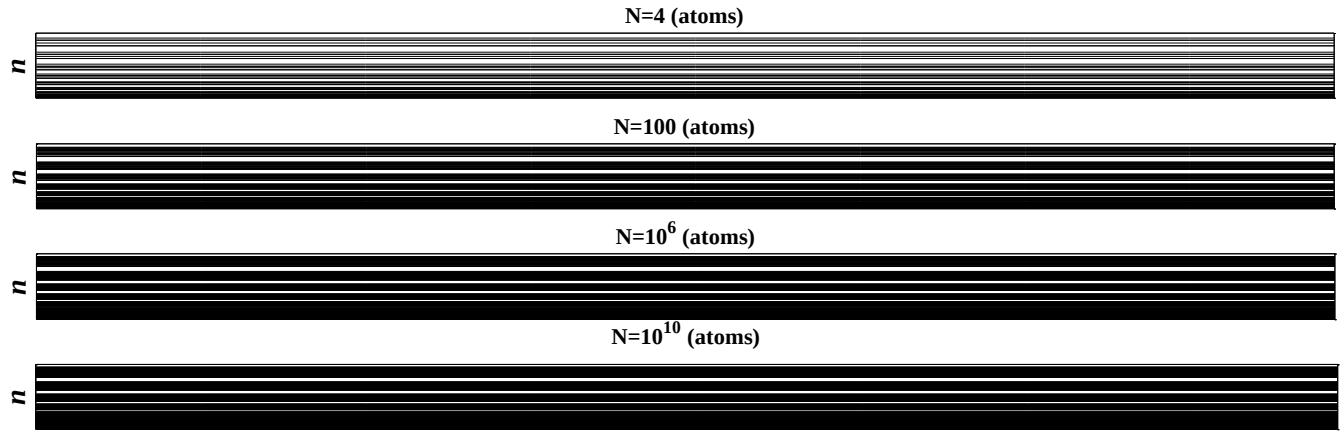

Figure 2-13: The splitting of energy levels due to the number of atoms in close proximity; as the number of atoms increases progressively the splitting about the principal energy level *n* increases accordingly until the bands about *n* appear continuous. The white bands are forbidden energy states. The figure is based on arbitrary values and does not represent any real data.

The Kronig-Penney Model

The potential function of a single atom is $V(r) = -e^2/4\pi\varepsilon_o r$ where r is always positive with the center of the atom at $r = 0$. The previous analysis can now be extended to a one-dimensional model of potentials and wells spreading across a one-dimensional crystal; the model was first introduced in 1931 by R.L. Kronig and W.G. Penney (Stephen T. Thornton, Andrew Rex, 2006).

Figure 2-14 shows the progression of the potential function in a one-dimensional crystal resulting from the overlapping of potential functions of closely packed atoms. The Kronig-Penney model is an idealized representation of adjacent potential barriers separated by potential wells. The model idealizes Fig. 2-14 (c) and depicts potential barriers and wells equal in width and height as shown in Fig. 2-15.

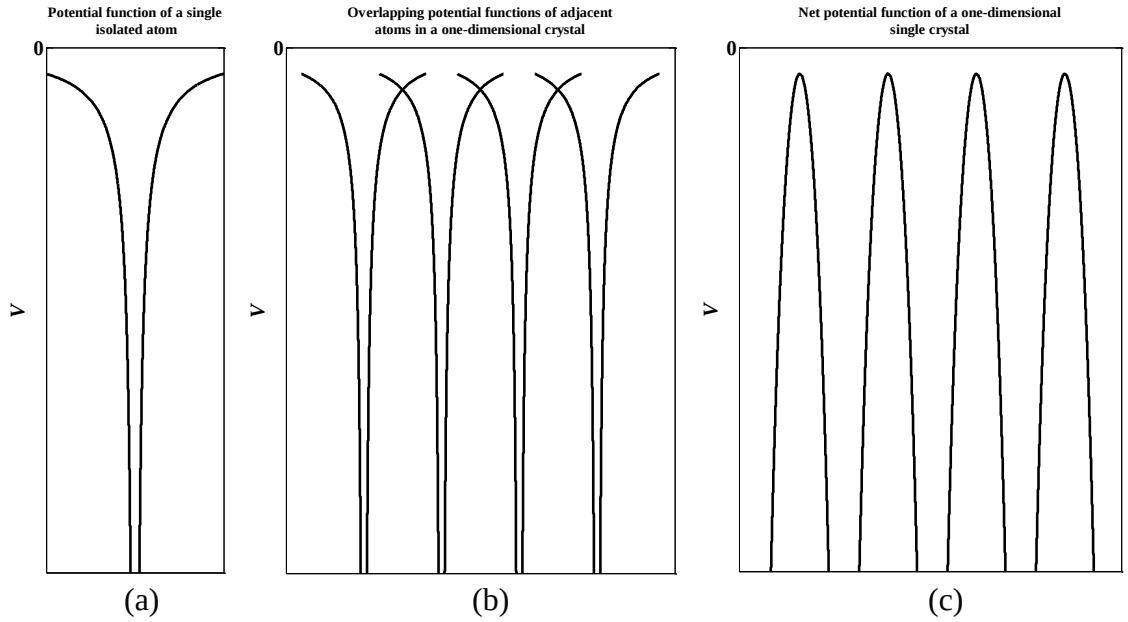

Figure 2-14: (a)-potential function of an isolated atom. (b)- Due to the close placement of atoms in a crystal the potential functions overlap. (c)- The overlapping potential functions add to produce a net potential function in the crystal.

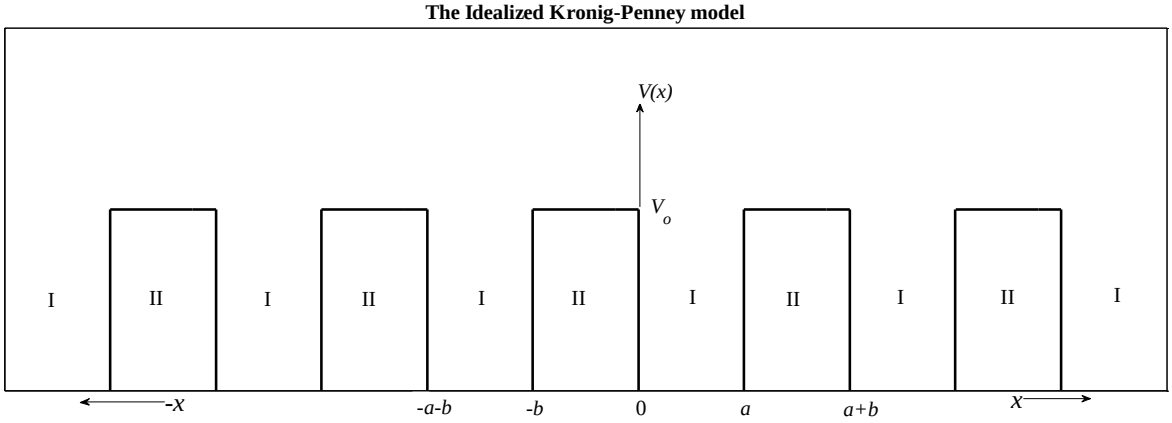

Figure 2-15: The idealized Kronig-Penney model has equal potentials and widths on all barriers and wells, respectively.

In Fig. 2-15 all barriers are of equal width and potential, and all wells have the same width. Thus all wells are labeled as region I, and all barriers are labeled as region II. In a real crystal neither the potentials nor the wells have equal widths or heights. The idealization simplifies solving Schrödinger's equation and offers qualitative insight into important features of the quantum behavior of electrons in a periodic lattice.

The mathematical theorem by Bloch[6] gives the solution to Schrödinger's Eq. in a one-dimensional crystal as

$$\psi(x) = u(x)e^{ikx}, \tag{2-1.44}$$

where k is a constant of motion and $u(x)$ is a periodic function with period $(a+b)$ extending from the starting point of a barrier to the starting point on the next barrier. As previously stated in Eq. 2-1.2, the total solution to the wave equation is the product of the time-independent and time-dependent solutions, which in terms of Eq. 2-1.44 becomes the traveling-wave in Eq. 2-1.45 , representing the motion of an electron in a single-crystal material.

$$\begin{aligned}\Psi(x,t) = \psi(x)\psi(t) &= u(x)e^{ikx}e^{-i(E/\hbar)t} \\ &= u(x)e^{i(kx-(E/\hbar)t)}\end{aligned}. \tag{2-1.45}$$

The relation between k, the total energy E, and the potential V_o, can now be determined by considering a well region—labeled I $(0 < x < a)$—in Figure 2-15 where V_o is zero and substituting the second derivative of Eq. 2-1.44 into the time independent Schrödinger's Eq. given by Eq. 2-1.8 this results in

$$\frac{d^2u_1(x)}{dx^2} + 2ik\frac{du_1(x)}{dx} - (k^2 - \alpha^2)u_1(x) = 0, \tag{2-1.46}$$

where $u_1(x)$ is the amplitude of the wave function in region I and the parameter α is defined as $\alpha^2 = 2mE/\hbar^2$. Performing the same operation on region II $-b < x < 0$ in Fig. 2-15 where V_o is not zero results in

$$\frac{d^2u_2(x)}{dx^2} + 2ik\frac{du_2(x)}{dx} - \left(k^2 - \alpha^2 + \frac{2mV_o}{\hbar^2}\right)u_2(x) = 0. \tag{2-1.47}$$

By defining $\beta^2 = \alpha^2 - 2mV_o/\hbar^2$ Eq. 2-1.47 becomes

$$\frac{d^2u_2(x)}{dx^2} + 2ik\frac{du_2(x)}{dx} - (k^2 - \beta^2)u_2(x) = 0. \tag{2-1.48}$$

[6] Bloch's theorem states that all one-electron wave functions involving periodically varying potential energy functions must be of the form $\psi(x) = u(x)e^{ikx}$ (Neamen, 1992). The solutions are known in literature as Bloch waves.

Noting from the previous definition of α, if $E > V_o$, β is real, and if $E < V_o$, β is imaginary.

The solutions for all regions labeled "I" in Fig. 2-15 are the specific solution of Eq. 2-1.46 particular to the region and given by Eq. 2-1.49 (Neamen, 1992)

$$u_1(x) = Ae^{i(\alpha-k)x} + Be^{-i(\alpha+k)x} \qquad 2a_{n-1} + b < x < a_n \tag{2-1.49}$$

and the solutions for all regions labeled II in Fig. 2-15 are the specific solution of Eq. 2-1.48 particular to the region and given by Eq. 2-1.50 (Neamen, 1992)

$$u_2(x) = Ce^{i(\beta-k)x} + De^{-i(\beta+k)x} \qquad a_n < x < a_n + b. \tag{2-1.50}$$

The continuity of $V(x)$ implies that the first derivative of $u(x)$ and $u(x)$ must also be continuous at all transitions from regions I into regions II and vice versa as the wave—electron—propagates through the crystal.

Considering the boundary $x = 0$ where, because of continuity, $u_1(0) = u_2(0)$

$$A + B = C + D$$
$$\text{or} \tag{2-1.51}$$
$$A + B - C - D = 0$$

now applying the second condition

$$\left.\frac{du_1(x)}{dx}\right|_{x=0} = \left.\frac{du_2(x)}{dx}\right|_{x=0} \tag{2-1.52}$$

yields

$$(\alpha - k)A - (\alpha + k)B - (\beta - k)C + (\beta + k)D = 0. \tag{2-1.53}$$

Applying the same conditions for region I $0 < x < a$, $x_{\underline{\lim a}}$ and region II $-b < x < 0$, $x_{\underline{\lim(-b)}}$ where the first condition $u_1(a) = u_2(-b)$ yields

$$Ae^{i(\alpha-k)a} + Be^{-i(\alpha+k)a} - Ce^{-i(\beta-k)b} - De^{i(\beta+k)b} = 0. \tag{2-1.54}$$

Applying the second boundary condition

$$\left.\frac{du_1(x)}{dx}\right|_{x=a} = \left.\frac{du_2(x)}{dx}\right|_{x=-b} \tag{2-1.55}$$

yields

$$(\alpha-k)Ae^{i(\alpha-k)a}-(\alpha+k)Be^{-i(\alpha+k)a}-(\beta-k)Ce^{-i(\beta-k)b}+(\beta+k)De^{i(\beta+k)b}=0 \quad \text{2-1.56}$$

Equations 2-1.51, 2-1.53, 2-1.54, and 2-1.56 are four simultaneous, linear, homogeneous equations with four unknowns: $A, B, C,$ and D. The trivial solution is setting the four coefficients to zero; a nontrivial solution exists if and only if the determinant is zero as shown in Eq. 2-1.57 (Neamen, 1992)

$$\begin{vmatrix} 1 & 1 & -1 & -1 \\ (\alpha-k) & -(\alpha+k) & -(\beta-k) & (\beta+k) \\ e^{i(\alpha-k)a} & e^{-i(\alpha+k)a} & -e^{-i(\beta-k)b} & -e^{i(\beta+k)b} \\ (\alpha-k)e^{i(\alpha-k)a} & -(\alpha+k)e^{-i(\alpha+k)a} & -(\beta-k)e^{-i(\beta-k)b} & (\beta+k)e^{i(\beta+k)b} \end{vmatrix}=0 \quad \text{2-1.57}$$

The solution to the matrix determinant in Eq. 2-1.57 is given by (Neamen, 1992)

$$\frac{-(\alpha^2+\beta^2)}{2\alpha\beta}\sin(\alpha a)\sin(\beta b)+\cos(\alpha a)\cos(\beta b)-\cos[k(a+b)]=0 \quad E\geq V_o \quad \text{2-1.58}$$

Equation 2-1.58 directly relates *k* to E and V_o via α and β (Neamen, 1992).

If $E > V_o$ the electron would be free, but the useful behavior of semiconductors arises when the electrons are bound in the crystal with $E < V_o$ where tunneling occurs as earlier demonstrated by the transmittance parameter *T*—Eq. 2-1.39—in the potential barrier example. With $E < V_o$, β is imaginary where $\beta = i\gamma$ and $\gamma = -i\beta$. Eq. 2-1.58 may be written as Eq. 2-1.59 which can only be solved by numerical or graphical techniques. Numerical or graphical techniques require the substitution of the symbolic expressions or numerical values of the parameters α and β and given by (Neamen, 1992)

$$\left.\begin{aligned} &\frac{-(\alpha^2+\beta^2)}{2\alpha\beta}\sin(\alpha a)\sinh(-i\beta b)+\cos(\alpha a)\cosh(-i\beta b)-\cos[k(a+b)]=0 \\ &\text{or} \\ &\frac{-(\alpha^2+\beta^2)}{2\alpha\beta}\sin(\alpha a)\sinh(b\gamma)+\cos(\alpha a)\cosh(b\gamma)-\cos[k(a+b)]=0 \end{aligned}\right\} E<V_0 \quad \text{2-1.59}$$

To obtain an equation more amenable to graphical solution, let the width of the potential barrier approach zero and the potential approach infinity; i.e. $\lim_{b\to 0}$ and $\lim_{V_o\to\infty}$ where the product bV_o

remains finite and Eq. 2-1.59 reduces to Eq. 2-1.60 (Neamen, 1992), which is analogous to the one-dimensional Dirac comb function[7] (Griffiths, 2005).

$$\left(\frac{mV_o ba}{\hbar^2}\right)\frac{\sin(\alpha a)}{\alpha a}+\cos(\alpha a)=\cos(ka) \qquad 2\text{-}1.60$$

The first term in Eq. 2-1.60 was derived by using l'Hopital's rule[8] for $0(-\infty/\infty)$, the other two terms are simple substitutions of $\lim_{b\to 0}$. By designating $O' \equiv mV_o ba/\hbar^2$ Eq. 2-1.60 can be rewritten as

$$O'\frac{\sin(\alpha a)}{\alpha a}+\cos(\alpha a)=\cos(ka) \qquad 2\text{-}1.61$$

.

Eq. 2-1.61 is not a direct solution to Schrödinger's equation but rather provides the conditions for which Schrödinger's equation has solutions (Neamen, 1992). In a disordered solid the analogy to the Kronig-Penney Model would be randomized barrier heights and widths rendering high unpredictability of a material's electrical properties.

The Energy Band-gap

Equation 2-1.58 directly relates *k* to the electron's total energy *E* via the parameter α. If V_o in Eq. 2-1.60 is zero then the parameter O' in Eq. 2-1.61 is also zero and $\cos(\alpha a)=\cos(ka)$. This means $\alpha = k$ and the electron is unbound and energy is continuous with no allowed and forbidden energy bands as in Fig. 2-13.

If the electron's energy remains constant and O' increases, the electron becomes increasingly bound to the potential until the total energy of the electron becomes less than the potential and the energy band structure becomes more pronounced. The plot of Eq. 2-1.61 with $E \le V_o$ demonstrates the band structure and is referred to as the *k*-space diagram of a bounded electron.

[7] The one-dimensional Dirac comb function is a periodic function consisting of evenly spaced delta spikes.

[8] l'Hopital's rule uses derivatives to determine limit values when the limit is indeterminate such as $\infty/0,\ 0/\infty, \infty/\infty,$ or $0/0$

Equation 2-1.61 can be represented as $f(\alpha a)=\cos(ka)$ (Neamen, 1992). Fig. 2-16 is a plot of $f(\alpha a)$ verses αa or the LHS of Eq. 2-1.61 where O' is arbitrarily assumed to be 4. The two straight lines at -1 and $+1$ in the bottom Fig. of Fig. 2-16 represent the minimum and maximum limits of the RHS of Eq. 2-1.61 or $\cos(ka)$.

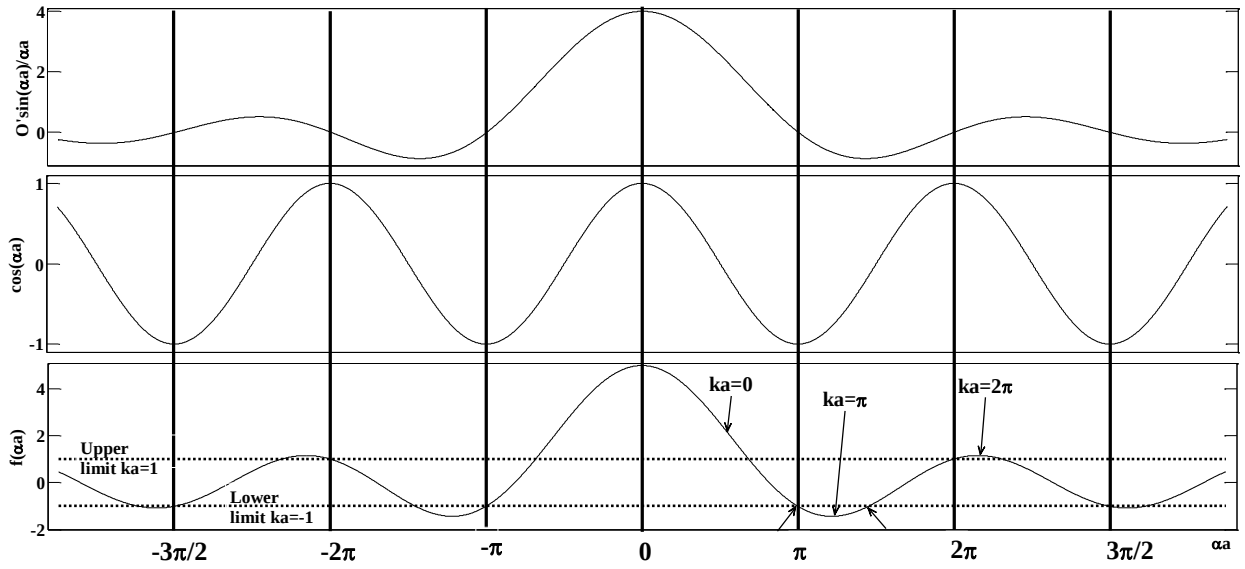

Figure 2-16: Top-$O'\sin(\alpha a)/\alpha a$. Center-$\cos(\alpha a)$. Bottom-$O'\sin(\alpha a)/\alpha a+\cos(\alpha a)$. The two straight lines at -1 and $+1$ in the bottom portion are the limits of $\cos(ka)$ where *k* is zero or $\pm\pi/a$ and the limits alternate as -1^n $\quad n=0,1,2,3,\cdots,\infty$. O' and α were arbitrarily chosen as 4 and 1.5 respectively and the parameter *a* was also assigned an arbitrary value of 1.

For Eq. 2-1.61 to be satisfied, the portions of $f(\alpha a)$ lying outside the limits of $\cos(ka)$ are not solutions to Eq. 2-1.61 and are the forbidden energy levels—band-gaps. The band-gaps in Fig. 2-16 can also be represented in a k-space diagram which could be directly extracted from Eq. 2-1.61 (Neamen, 1992) by isolating the parameter *ka*.

Section 2.2: Semiconductors and Neutron Detection

Two basic types of neutron interactions with matter are of most interest in radiation detection. First, the neutron can be scattered by a nucleus, transferring some of its kinetic energy to the nucleus. If enough energy is transferred, the recoiling nucleus ionizes the material surrounding the point of interaction. This recoil mechanism is only efficient for neutrons interacting with light nuclei. In fact, only hydrogen and helium nuclei are light enough for use in

practical detectors. Second, the neutron can cause a nuclear absorption reaction. The products from these reactions, such as protons, alpha particles, gamma rays, and fission fragments, can initiate the detection process. Some reactions require minimum neutron energy (threshold), but many take place at thermal energies. Detectors exploiting thermal reactions are usually surrounded by moderating material to take maximum advantage of this feature (Crane and Baker, 1991). When semiconductor detectors are used as the pulse generating medium, the energy deposition by charged particles generates e-hole pairs which ultimately get collected by the bias voltage generating a pulse. In the current section, mechanisms whereby semiconductors respond to charged particles are described.

The *pn* Junction

A doped semiconductor in contact with a metal can either form an Ohmic or a rectifying Schottky contact, and a *pn* junction is formed when a *p*-doped and an *n*-doped semiconductor are in contact. In the cases where a Schottky contact or a *pn* junction are formed a depletion region is generated; in either case, the device is a diode.

Basic Structure of the *pn* Junction

A *pn* junction is shown in Fig. 2-17. In actuality, however, the two regions are part of the same crystalline volume that has been doped with one type of dopant on one side, with the other type of dopant on the other, often the substrate material.

The *n* dopants are also known as electron donors because they provide electrons which become mobile under the influence of an electric field or thermal excitation. The freed electrons diffuse into the *p* doped region where the dopants are also known as electron acceptors. The holes[9] migrate into the *n* doped region. The diffusion of electrons and migration of holes reaches equilibrium and a space charge depleted region is formed between the two doped regions; the region is referred to as the depletion region (Neamen, 1992). In diodes, the width of the depletion region is a function of applied voltage and temperature; the direction of the applied electric field also is referred to as the bias direction.

[9] Positive ions left behind in the valence band when electrons from the valence band are excited to the conduction band.

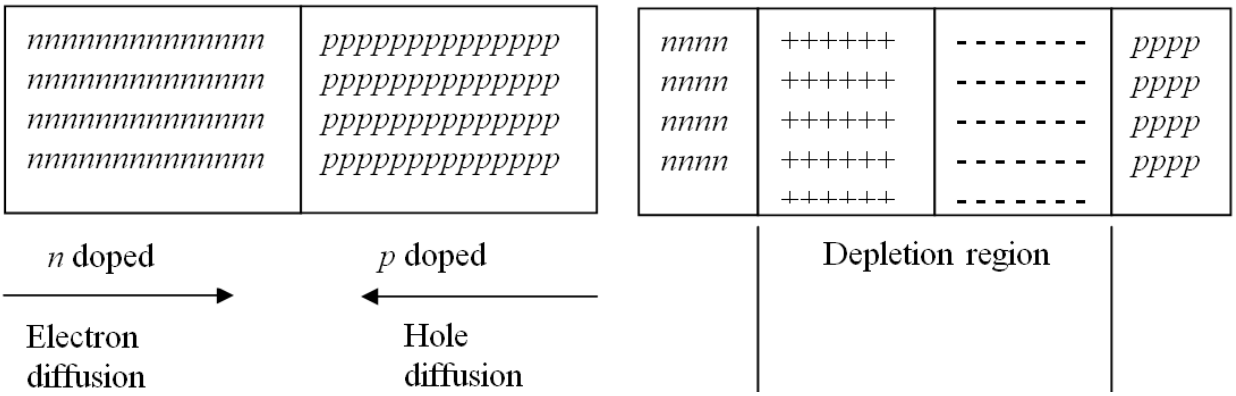

Figure 2-17: (a)-Two doped regions, showing the mobile charge carriers, in contact forming the initial *pn* contact plane. (b)-The depletion region is formed when the diffusion of electrons into the *p* region and the migration of holes into the *n* doped region reaches equilibrium leaving behind immobile ions.

Biasing

Devices can be biased in three ways: zero, forward, or reverse biasing. Reverse biasing is the configuration required for charged particle detection, and thus neutron detection (Knoll, 2010). Forward biasing will not be discussed, for in the case of forward biasing there is always current flow, which prohibits signal isolation.

Zero Biasing: The Built-In Potential Barrier

Assuming no voltage is applied across the *pn* junction, then a fair deduction would be: if the temperature across the entire device is uniform, the device and consequently the *pn* junction is in thermal equilibrium, and the Fermi energy level[10] is constant throughout the system (Neamen, 1992). The conduction and valence band energies must bend going through the depletion region, because the relative position of the conduction and valence bands with respect to the Fermi energy changes between *p* and *n* regions (Neamen, 1992), as shown in Fig. 2-18. The built-in potential $V_{barrier}$ maintains equilibrium between majority carrier electrons in the *n*

[10] The Fermi energy is a concept in quantum mechanics referring to the energy of the highest quantum state in a system of fermions at absolute zero (0 K)

region and minority carrier electrons in the *p* region, and also between majority carrier holes in the *p* region and minority carrier holes in the *n* region.

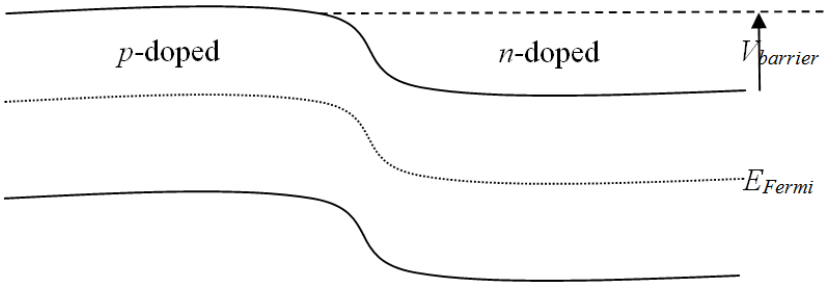

Figure 2-18: Energy band diagram of a *pn* junction in thermal equilibrium and at zero bias voltage showing the Fermi Energy Level and the built in potential $V_{barrier}$.

The potential barrier is given by ,

$$V_{\text{barrier}} = \frac{kT}{e}\ln\left(\frac{N_d N_a}{n_i^2}\right), \qquad 2\text{-}2.1$$

where n_i is the intrinsic carrier concentration, N_d and N_a are the donor (*n*-dopant) and acceptor (*p*-dopant) concentrations respectively, k is the Boltzmann constant, T the system's temperature, and e is the electron's coulomb charge (Neamen, 1992).

Reverse Biasing and Depletion Region Width

Reverse biasing a device constitutes the application of a positive potential on the *n*-doped region with respect to the *p*-doped region. By applying a potential, whether in reverse or forward bias, the device will no longer be in thermal equilibrium and the Fermi energy level is no longer constant throughout the system (Neamen, 1992), as shown in Fig. 2-19, and the Fermi level on the *n* side is below the Fermi level on the *p* side. The difference between the two is equal to the applied voltage or energy over charge (kT/q). The total potential barrier is the sum of the built in potential and the applied reverse bias voltage given by Eq. 2-2.2, and V_{bi} is given in Eq. 2-2.1. The depletion region's width is given by Eq. 2-2.3 (Neamen, 1992) where the semiconductor's permittivity is ε_s and ε_o is the permittivity of free space.

$$V_{\text{total}} = V_{bi} + V_{\text{Applied}} \qquad 2\text{-}2.2$$

$$W_{\text{Depletion}} = \sqrt{\frac{2\varepsilon_s\varepsilon_o V_{\text{total}}}{e}\frac{N_a + N_d}{N_a N_d}} \qquad 2\text{-}2.3$$

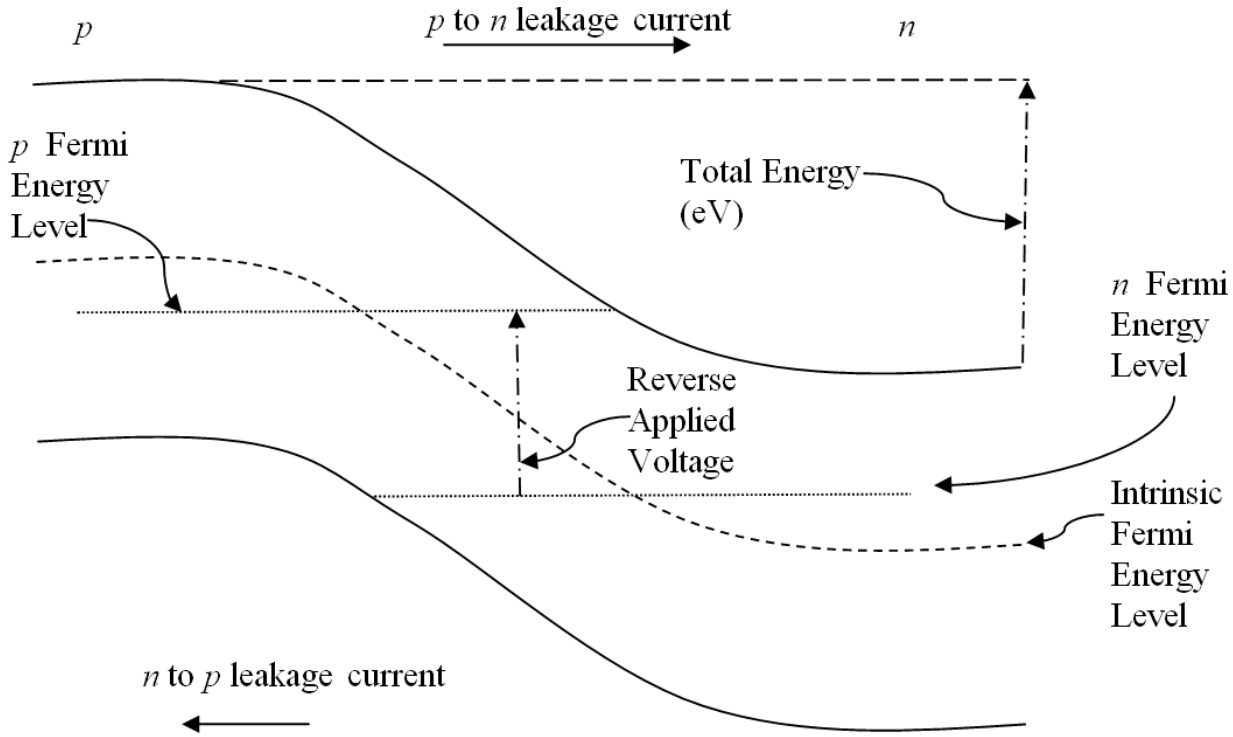

Figure 2-19: Energy band diagram of a *pn* junction in reverse bias (Neamen, 1992). The total leakage current in reverse biasing is the sum of both leakage currents.

The width of the depletion region described in Eq. 2-2.3 is also referred to as the "active volume" of a semiconductor device designed for radiation detection purposes (Knoll, 2010). The region is referred to in such a manner because only e-hole pairs generated within the depletion region of a reverse biased detector generate detectable pulses. The electric field in the bulk of the *n* and *p* doped regions is negligible and assumed to be zero (Neamen, 1992) in most calculations, and the electric field's presence is mostly in the depletion region and can separate the e-hole pairs as they are generated.

Neutron Detection via Charged Particles

When a device is in reverse bias, a leakage current, generally on the order of micro or nano-amps, is always present even when the applied voltage is less than the device's breakdown voltage[11]; therefore, for efficient pulse counting detection, all signals generated must be of a current higher than the leakage current (which contributes to noise).

[11] The voltage required to overcome the resistance presented by the depletion region.

Energy Deposition and e-hole Pair Generation by Charged Particles

Before a charged particle reaches the detector's active volume, the particle must go through a "dead layer" (Knoll, 2010) if the particle's origin is outside the detector; the dead layer constitutes detector housing and fabrication materials as well as the inactive regions of the semiconductor device itself. Consequently, not all the energy is deposited in the detector's effective region. However, if the neutron interacts with a conversion isotope such as ^{10}B inside the active volume as in the case of the proposed detector in Fig. 1-4, the reaction products would deposit a considerable amount of energy in the active zone of the detector. Energy deposition is given by the Bragg curve of which an example is shown in Fig. 1-2. On the other hand, a daughter particle may exit the active volume before complete energy deposition. In all cases however, once sufficient ionization energy[12] is deposited in the detector's active volume, a signal may be generated above the leakage current if the deposited energy is sufficient to generate enough e-hole pairs to surpass the leakage current/noise.

Pulse Generation and Affecting Factors

When a charged particle deposits energy in the active volume of the detector, e-hole pairs are generated. The electric field present in the vicinity must be sufficient to separate the pairs into a free electron capable of moving along the conduction band and a hole which migrates by electron substitution[13] in the opposite direction along the valence band. The electrons and holes, or the charge carriers, move in opposite directions constituting a monodirectional electric current which persists until all charges have been collected at the edges of the active region of the detector (Knoll, 2010). However there are factors which could affect the pulse's period, shape, and height; the factors are the direct result of the semiconductor's properties and the applied biasing voltage.

The first condition for effective pulse generation is a direct consequence of the ionization energy of the semiconductor material. Ionization energies in semiconductors are typically on the order of 3 to 10 eV. Considering the short ranges of charged particles in solid materials, such as a

[12] The minimum energy required to generate a single e-hole pair in the semiconductor's material.

[13] The combined electric field of the hole and the applied voltage pulls on an electron from a neighboring neutral site in the valence band neutralizing the original hole and leaving a hole in the neutral site's location, thus holes migrate in the direction of the applied electric field.

semiconductor's, the deposition of 3 to 10 eV in order to generate a single e-hole pair takes place very easily; however, a single e-hole pair is never sufficient to generate a pulse above noise given the charge carriers—electrons and holes—pass through all trapping sites[14] in the semiconductor on the way to the edges of the active region where they get collected. In effect, the more energy deposition the more charge carrier generation which directly translates to higher current, and from Ohm's law—$V = RI$ —the higher the current the higher the voltage when the resistance is constant. Thus the relation between pulse height and energy deposition: the pulse height is directly proportional to energy deposition in the detector's active volume.

Another factor which affects current as well as pulse period is charge carrier mobility in the semiconductor; in other words, the speed at which the charge carriers move under the influence of the electric field, for current is given by (Shockley, 1938, Ramo, 1939, and Radeka, 1988) $I = dQ/dt = qdV/dt$ where q is charge, V is the weighting potential, and dt is the time differential. Charge carrier mobility is an experimentally determined quantity; furthermore, the mobility of electrons is higher than the mobility of holes resulting in different drift velocities in the semiconductor given by Eqs. 2-2.4 and 2-2.5 (Knoll, 2010)

$$v_e = \mu_e E \qquad \text{2-2.4}$$

and

$$v_h = \mu_h E \,, \qquad \text{2-2.5}$$

where μ is the mobility, v is the drift velocity, and E is the applied electric field. The pulse's period is inversely affected by the mobility, i.e., higher mobility leads to a shorter pulse because charges are collected faster. Trapping sites affect pulse period: traps may hold on to charge carriers for an extended period of time. When traps release charge carriers into their respective bands at later times, the detrapping effect extends charge collection times and pulse period is increased as a consequence.

[14] Unintended impurities or unavoidable structural defects that hold charge carriers at energy levels between the conduction and the valence bands and prevent/delay further charge carrier migration to collection sites where a pulse is generated.

Section 2.3: Radiation Detector Efficiencies

As earlier mentioned, detector efficiencies are thoroughly discussed, described, and formulated elsewhere (McGregor and Shultis, 2011). The types of efficiencies described here are absolute, relative, and intrinsic efficiency for point and beam sources. Here the discussion on efficiencies will be short and is only meant for completeness. Further details can be found in the literature (McGregor and Shultis, 2011).

As earlier stated, the perception of the efficiency of a detector being the ratio of absorbed neutrons resulting in detectable signals to the number of neutrons impinging on the detector is intrinsically incomplete. Source activity, geometric set up, source and detector shapes determine the number of neutrons impinging on the detector. Unless the source is a collimated beam encompassing an area less than the detector's area exposed to the beam, the number of neutrons impinging on the detector is invariably a fraction of the actual number of neutrons emanating from the source. Thus, for total efficiency to be determined, variables such as source activity, solid angle subtended by the detector from every point of the source, and detector orientation must be known.

Absolute efficiency $\equiv \varepsilon_A$ is defined as the ratio of detectable signals/counts to the total number of emissions from the source and is mathematically described by Eq. 2-3.1 to include the branching ratio[15]. Absolute efficiency is an example of how an efficiency measurement can change with geometric set up between source and detector as shown in Fig. 2-20.

$$\varepsilon_A = \frac{\text{count rate}}{\left(\text{source acitvity}\right)\cdot\left(\text{branching ratio}\right)} \equiv \frac{R_{\text{det}}}{AB} \qquad 2\text{-}3.1$$

[15] The branching ratio is the ratio of activity of the source with the specific radiation to the total activity of the source.

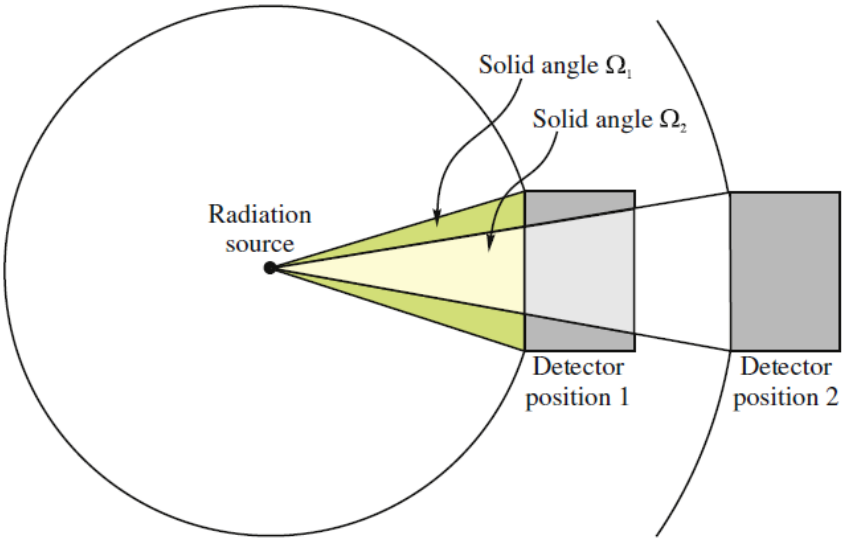

Figure 2-20: The radiation flux entering the detector at position 1 with solid angle Ω_1 is greater than the radiation flux entering the detector at position 2 with solid angle Ω_2 (McGregor and Shultis, 2011). Should the source have been a line or a plane source, then the solid angles subtended by the detectors from every point on the source must be considered.

Relative efficiency is akin to absolute efficiency where, by again referring to Fig. 2-20, relative efficiency is simply the ratio of the absolute efficiencies of two detectors under the same exact geometric setup and conditions where one of the absolute efficiencies is known and used as the reference efficiency as shown in Eq. 2-3.2.

$$\varepsilon_R = \frac{\text{count rate}}{(\text{source activity})\cdot(\text{branching ratio})\,\varepsilon_A^{\text{reference detector}}} \equiv \frac{R_{\text{det}}}{AB\varepsilon_A^{\text{reference detector}}} = \frac{\varepsilon_A^{\text{detector}}}{\varepsilon_A^{\text{reference detector}}} \qquad 2\text{-}3.2$$

The values of both absolute and relative efficiencies are highly dependent on geometry, and the geometry must be reported in detail along with source activity and type of source. Caution must be exercised when reporting relative efficiency, given the same source, activity and branching ratio cancel out reducing Eq. 2-3.2 to Eq. 2-3.3; implying, if the detectors have the same parameters, relative efficiency may seem to be 100%.

$$\varepsilon_R = \frac{R^{\text{detector}}}{R^{\text{reference}}} \qquad 2\text{-}3.3$$

Intrinsic efficiency of a detector exposed to radiation from a point source is the introduction of the subtended solid angle to absolute efficiency where the solid angle is the fraction of the source's activity reaching the detector as given in Eq. 2-3.4 and can still be described by Fig. 2-20.

$$\varepsilon_{i_{\text{point}}} = \frac{\text{count rate}}{(\text{source activity})\cdot(\text{branching ratio})\cdot(\text{solid angle})} \equiv \frac{R_{\text{det}}}{AB\Omega} = \frac{\varepsilon_A}{\Omega} \qquad \text{2-3.4}$$

The introduction of the solid angle factor mitigates the need to accurately describe the geometric arrangement; however depending on the detector's geometric parameters such as the area exposed to the radiation and thickness of the reacting medium, a parallax factor which is intrinsic to the detector can affect the efficiency if the NCM is sufficiently thick. This is because the solid angle varies with respect to depth into the NCM from the exposed surface and is analogous to a multitude of detectors at different distances from the source as shown in Fig. 2-21. Therefore the reacting medium's geometric parameters must be described along with the solid angle subtended by the detector's surface facing the source.

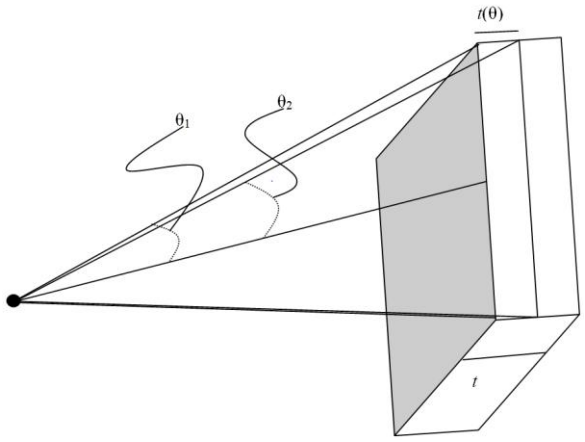

Figure 2-21: A depiction of a sufficiently thick NCM with thickness *t* shows the parallax effect at two different thicknesses, the thickness *t* (θ) varies with the angle as sin (θ) and Eq. 2-3.4 must be adjusted accordingly (McGregor and Shultis, 2011).

Finally, the intrinsic efficiency of a detector in a beam source is of particular interest, for the efficiency of the detectors developed in the project will be ultimately evaluated using the mono-energetic thermal neutron beam—0.025 eV—at KSU. The detectors may also be tested using the multi-energetic neutrons in the southeast beam emanating from the reactor's core. The advantage of using a mono-energetic neutron source is because the neutron absorption cross-section of the NCM, h-BN, is invariant where as in a multi-energetic source the cross-section is

different for different neutron energies (Fig. 1-1) and thus the neutron energy spectrum must be known along with the intensity of neutrons within each differential energy interval defined by the experimenter(s).

The geometric advantage of using a beam source is the near total independence from solid angle determination, where the solid angle is small enough to be considered negligible; however geometric dependence on area persists. The dependence on area results from the angle of incidence of the beam on the detector's surface as shown in Fig. 2-22, and the intrinsic efficiency of a detector in a beam source is given by

$$\varepsilon_i = \frac{\text{count rate}}{(\text{beam intensity})\cdot(\text{intersected area})} \equiv \frac{R_{\text{detector}}}{I\text{A}_{\perp}\cos(\phi)}. \qquad 2\text{-}3.5$$

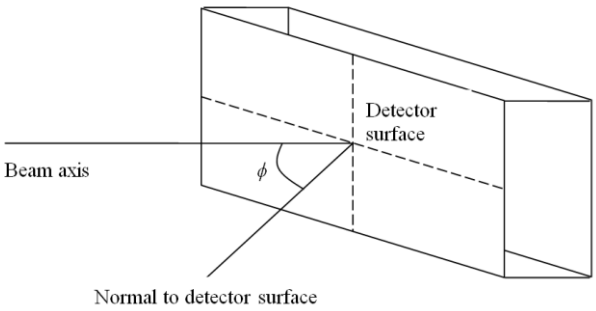

Figure 2-22: A detector facing a beam with an angle of incidence ϕ. The area intersected by the detector's surface and the beam is the area of the detector's surface multiplied by the cosine of the angle of incidence, or if the detector's area is larger than the beam's area than the intersected area is the beam's area multiplied by the cosine of the angle of incidence.

Measuring the intrinsic efficiency of a new detector such as the one fabricated at TTU requires relating the detector's count rate to another detector's count rate with known intrinsic efficiency; the efficiency procedure and formulation will be discussed in the procedural section concerned with the evaluation of a detector's efficiency.

Section 2.4: Monte Carlo Coding

Due to advances in computer technology and availability, Monte Carlo methods are often used by various industries and academic fields of study where the statistics of events is based on

randomness. The main advantage Monte Carlo offers is the ability to statistically analyze events/processes, based on pseudo-randomly generated statistical data, without the need for live or actual data collection. Such abilities allow the comparison of actual results to theoretical results, and may be used to improve the process or design. However, any Monte Carlo code written to analyze a certain process should be validated by comparison to known results.

Efficiency assessment of any detector/sample is to be performed using a beam source and Eq. 1-2.7 with $\phi = 0$. Thus, a Monte Carlo code was written to reflect the conditions and treat neutrons from a collimated beam source incident perpendicular—ϕ=0—to the detector's square surface area facing the beam. The detector is modeled as having a thickness *T*.

Based on the description of the proposed detector, where the detector's NCM is the operational semiconductor, and on the discussion in Section 2.2: Semiconductors and Neutron Detection, a significant percentage of the charge generated as e-hole pairs by the energy deposited within the NCM is collected. Thus, the code is focused on evaluating energy deposition within the NCM for each neutron interaction in the h-BN medium. The charged particles resulting from the reactions in Eq. 1-1.2 are emitted isotropically in opposite directions, to conserve momentum. The scored quantity is a histogram of energy deposition in the medium.

Energy versus Distance Data and Fits

The first and one of the most important steps in the coding process is to acquire data reflecting charged particle energy loss as a function of distance travelled for the purposes of energy deposition calculations. The relevant energy distance data needed are the data pertaining to the charged particle products by the reactions in Eq. 1-1.2 in h-BN. The free source program SRIM (Ziegler, 2011), which uses Monte Carlo methods and formulation, was used to acquire the needed energy deposition data. Figures 2-23 through 2-26 show the actual SRIM data and curves fitted by Matlab to the data. The respective fit equations are given in Eqs. 2-4.1 through 2-4.4.

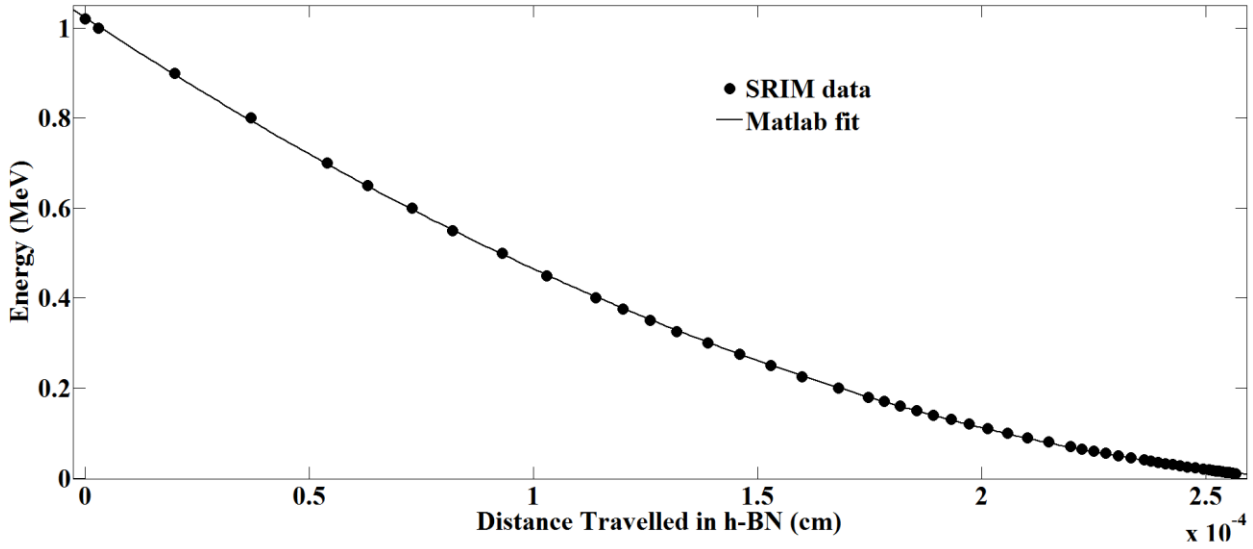

Figure 2-23: Matlab energy verses distance fit for SRIM generated data for the 1.02 MeV lithium nucleus from the first reaction in Eq. 1-1.2.

$$E(r)_{\text{MeV}} = 3.761\times10^{9} r^{3} + 9.14\times10^{6} r^{2} - 6536r + 1.023 \qquad \text{2-4.1}$$

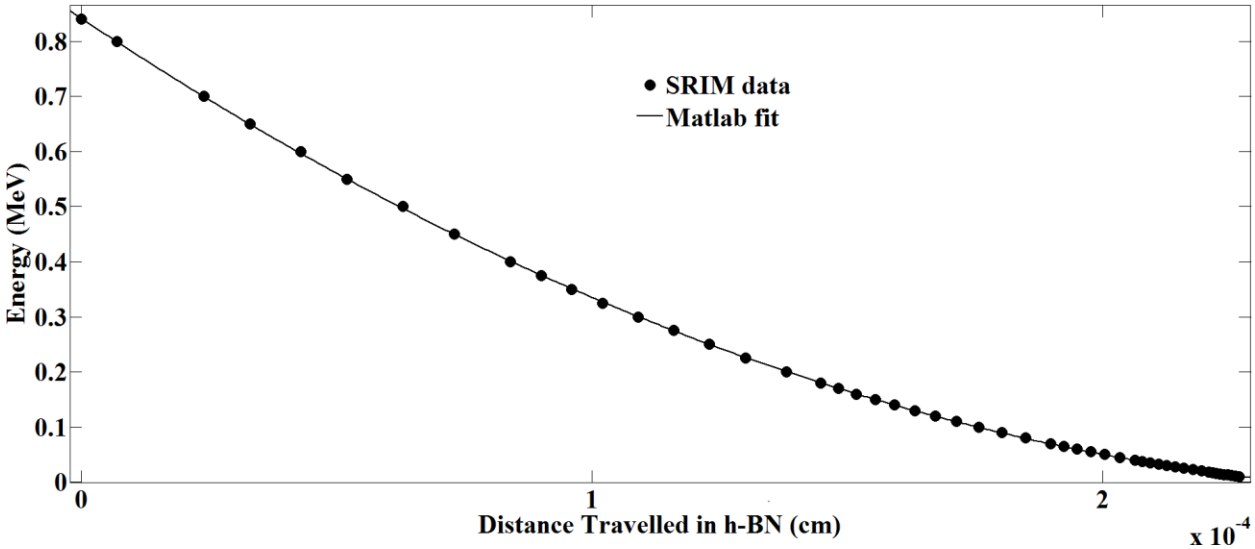

Figure 2-24: Matlab energy verses distance fit for SRIM generated data for the 0.84 MeV lithium nucleus from the second reaction in Eq. 1-1.2.

$$E(r)_{\text{MeV}} = 1.311\times10^{9} r^{3} + 1.151\times10^{7} r^{2} - 6211r + 0.824 \qquad \text{2-4.2}$$

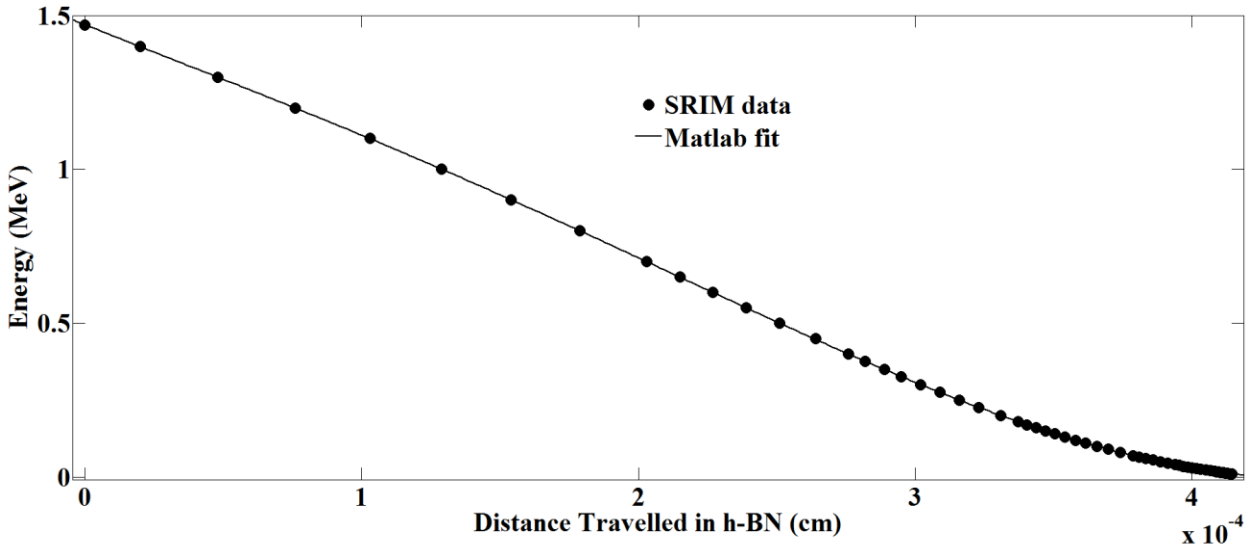

Figure 2-25: Matlab energy verses distance fit for SRIM generated data for the 1.47 MeV alpha-particle from the first reaction in Eq. 1-1.2.

$$E(r)_{\text{MeV}} = -3.79\times10^{16}r^5 + 7.924\times10^{13}r^4 - 3.249\times10^{10}r^3 + 2.799\times10^{6}r^2 - 3625r + 1.471 \qquad \text{2-4.3}$$

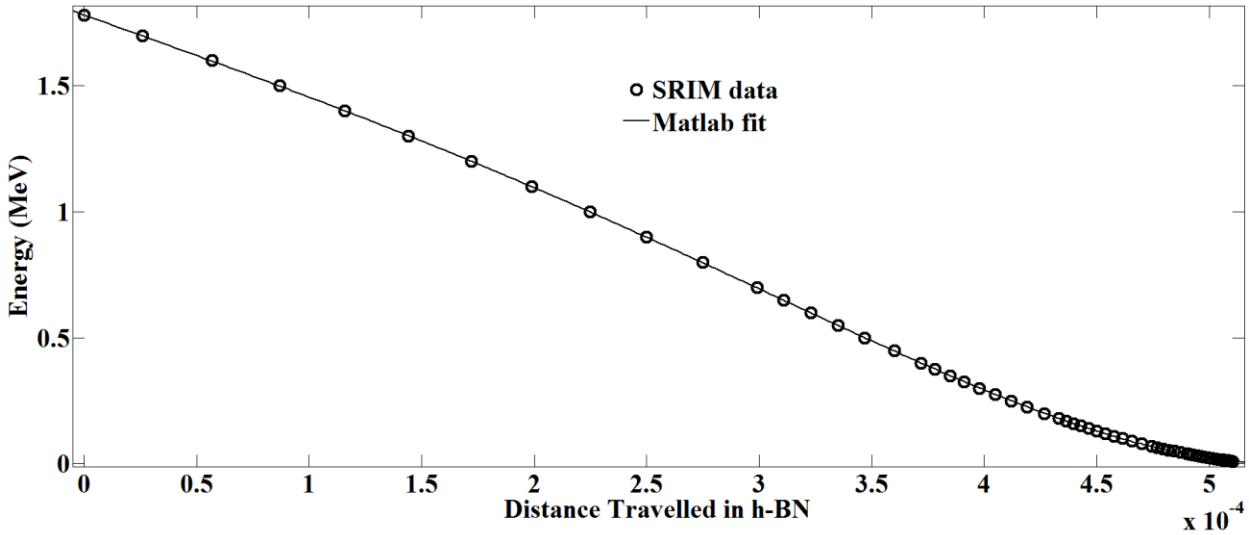

Figure 2-26: Matlab energy verses distance fit for SRIM generated data of the 1.78 MeV alpha-particle from the second reaction in Eq. 1-1.2.

$$E(r)_{\text{MeV}} = 2.475\times10^{16}r^5 - 2.016\times10^{12}r^4 - 6.676\times10^{9}r^3 + 1.365\times10^{5}r^2 - 3211r + 1.782 \qquad \text{2-4.4}$$

Figures 2-23 through 2-26 show the Matlab fits represented by Eqs. 2-4.1 through 2-4.4 shadowing the SRIM generated data. Thus, equations 2-4.1 through 2-4.4, also generated by

Matlab, are good approximations of the SRIM data and will be implemented in the code for energy deposition calculations as will be later discussed in the current section.

Logic Flow

In the current code the starting point in the life of a neutron is at the interface between a monoenergetic collimated thermal neutron beam with a diameter of 1.27 cm and the perpendicularly aligned NCM, h-BN. The h-BN layer is infinite in the (*x*, *z*) plane and the thickness *T* is in the *y* direction starting at $y = 0$ and ending at $y = T$. The energy of the neutrons in the beam is 0.025 eV. Based on Eq. 1-2.4 and the data in Fig. 1-1, the macroscopic absorption cross-section for h-BN synthesized from natural boron with a ^{10}B enrichment fraction of 0.198 is $\Sigma_a = 41.84\ \text{cm}^{-1}$. Neutron containment within the beam implies that a neutron enters the NCM uniformly within a disk with a diameter of 1.27 cm.

Selection of a starting position for a neutron in a disk distribution on the surface of the h-BN's layer is performed using a rejection method where two random positions, *x* and *z*, are chosen uniformly within a square with sides equal to the diameter of the beam and then checking whether the point (*x*, *z*) is in a disk of radius *R* (Dunn and Shultis, 2011). The two positions are determined, in history *i*, from

$$x_i \text{ or } z_i = R(2\rho_i - 1) \qquad \text{2-4.5}$$

where ρ_i is a random number on the interval [0,1], and the point (x_i, z_i) is accepted if and only if

$$\sqrt{x_i^2 + z_i^2} \le R \qquad \text{2-4.6}$$

.

However, rejection sampling within a disk is not necessary, for the code would yield similar energy deposition spectra—theoretical MCA pulse height spectra—for any other perpendicular neutron source geometry or even if the source geometry is not defined. This is due to the fact that energy deposition is dependent on the distance travelled by the particles in h-BN and not on the neutron's point of entry into the h-BN layer. Disk geometry was chosen because the thermal beam, in the reactor facility at KSU, which would be used for efficiency determination of any detector is rounded in geometry and has a diameter of 1.27 cm.

The next step is to determine whether or not the neutron interacted with the h-BN layer; if so, where with respect to the thickness of the layer? Choosing whether or not an interaction took place and at what depth relative to the neutron's point of entry into the h-BN was based on an exponential pdf (Dunn and Shultis, 2011); the choice is given by Eq. 2-4.7

$$t = \frac{-\ln(\rho)}{\Sigma_a} \tag{2-4.7}$$

where *t* could, for all practical matters, be greater than *T* (neutron escapes absorption); *T* is the h-BN's thickness.

Upon neutron absorption another random number is chosen to determine whether the first or the second reaction in Eq. 1-1.2 occurred. Given the probabilities of occurrence of 0.94 and 0.06, respectively, a random number on the interval [0,1] is chosen and if the random number is less than or equal to 0.06 then the second reaction has occurred, otherwise the first reaction has occurred.

The interaction depth has been determined for each of the neutrons which interacted within the h-BN layer and the next logical step is to randomly pick a direction of emission of the resulting particles. As earlier mentioned, the direction is isotropic and can lie anywhere in the 4π sphere. However, only the polar angle, θ, referenced from the positive *y* axis, on the interval [0, π] is necessary, for the layer's double-faced flat parallel geometry offers conical symmetry on the azimuthal angle once a polar angle has been chosen as shown in Fig. 2-27 where any azimuthal angle chosen in the *xz* plane will always fall in the prescribed cone and will not contribute to distance calculations. Choosing the polar angle involves integrating the cosine, ω, pdf of the angle on the interval [-1, 1] as in Eq. 2-4.8 resulting with ω as given by Eq.2-4.9 .The distances to the exit planes can be determined by dividing *t* and *T-t* by the cosine of the chosen angle which is ω, otherwise referred to as the directional cosine.

$$\frac{1}{2}\int_{-1}^{\omega} d\omega' = \frac{1}{2}\left[\omega + 1\right] = \rho_{i_\omega} \tag{2-4.8}$$

then

$$\omega_i = 2\rho_{i_\omega} - 1 \tag{2-4.9}$$

where ω_i is the cosine of the chosen angle θ_i. Choosing the cosine of the polar angle on the interval [-1,1] results in two cases: 1) $0 \le \omega_i \le 1$ and the chosen angle is on the interval $[0, \pi/2]$, 2) $-1 \le \omega_i \le 0$ and the chosen angle is on the interval $[\pi/2, \pi]$. As far as the case where $0 \le \omega_i \le 1$ is concerned dividing by ω_i yields a positive distance. However, when $-1 \le \omega_i \le 0$ the directional cosine is negative rendering the direction on the axis from positive to negative, or in the negative direction, and t must be represented as $-t$ and $T-t$ as $-(T-t)$ where both parameters yield positive distances when divided by ω_i. To mitigate the negative sign effects and the introduction of a conditional loop, t and T-t were divided by the absolute value of ω_i rendering the distance travelled by the particles positive in all cases as shown in Eqs. 2-4.10 and 2-4.11 where the distance travelled to the face of the layer at thickness equal zero is

$$d_i^{y=0} = \frac{t_i}{|\omega_i|}, \qquad \text{2-4.10}$$

and the distance travelled to the face of the layer at thickness T is

$$d_i^{y=T} = \frac{T - t_i}{|\omega_i|}. \qquad \text{2-4.11}$$

If the calculated distance in the angle's direction is greater than the particle's range travelling on the determined path, the energy deposited in the h-BN is the energy with which the particle was born, simply because the particle ionizes the h-BN and deposits energy until all the particle's energy is exhausted. On the other hand, if the distance is less than the particle's range, the deposited energy must, in all such cases, be calculated based on the mathematical fits in Figs. 2-23 through 2-26.

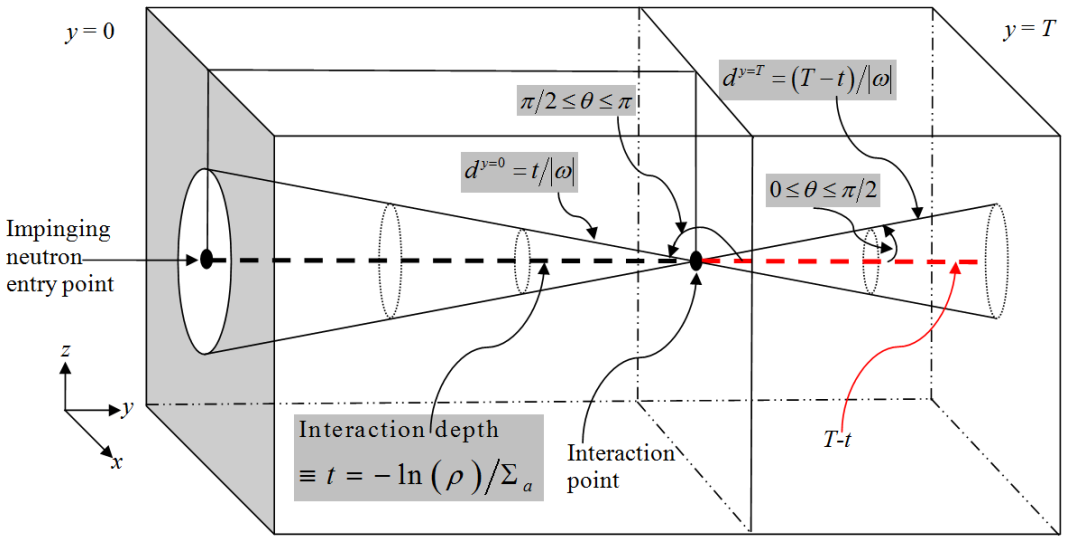

Figure 2-27: Illustration of the geometry leading to Eqs. 2-4.10 and 2-4.11 as well as the mentioned conical symmetry.

In Fig. 2-27 the distance travelled in the direction towards $y = 0$ is shown as $d^{y=0}$ and the distance travelled towards $y = T$ is shown as $d^{y=T}$. Also, clear from the Fig. 2-27, any line passing through the interaction point on the surface of the cone constitutes an equal path length to any other line on the surface of the cone passing through the interaction point providing conical symmetry and mitigating the need for an azimuthal angle which would fall in a circle circumscribing the cone's surface in Fig. 2-27.

The last event to be determined is which of the particles travels in which of the determined paths. To accomplish the task, a random number on the interval [0, 1] is chosen; if the number is on the interval [0, 0.5] then one of the particles travels in one of the directions and the other travels in the other, and if the number is on the interval [0.5, 1] the particles switch directions. In effect, the procedure gives each of the particles an equal probability of traveling in either direction rendering travelling in the 4π sphere possible for each of the particles.

The event inventory at this point stands at which of the two reactions has occurred, what is the distance inside the h-BN layer to each surface of the layer, and which particle traveled in which direction. With the event inventory complete, the energy deposited in the h-BN layer can be calculated using Eqs. 2-4.1 through 2-4.4, by simply calculating the energy at the distance travelled in the h-BN layer and subtracting the resulting energy from the energy a particle was

born with by applying Eq. 2-4.12 where *r* is the distance travelled within the range of the particle in h-BN.

$$E_i^{\text{Deposited}} = E_i^{\text{Initial}} - E_i(r) \qquad \text{2-4.12}$$

As earlier mentioned, if the distance to one of the h-BN layer's faces is greater than the particle's range in h-BN, then the entire energy the particle was born with is deposited in the h-BN layer.

Code Vetting and Validation

Hand calculations were performed on different sections of the code as the code was being written. As a consequence of the multitude of neutrons generated by the code, only a few hand calculations were performed and compared to the number of neutrons involved. Under such conditions, final vetting and validation must be the result of comparison with closely related known results. This was done by comparing the theoretical spectra based on the boron trifluoride (BF_3) tube and the absorption fraction in Eq. 1-2.7.

The Boron Trifluoride Tube

In principle a boron trifluoride (BF_3) tube's operation is similar to the operation of a ^{3}He tube, in the respect where both materials are gaseous. However, the neutron reacting isotope in a BF_3 tube is ^{10}B. Thus, a BF_3's tube spectrum provides a validation comparison to the spectrum from a BN semiconductor detector.

A radiation detector responds to energy deposited in the device and converted into charge carriers transported under the influence of an applied electric field. In other words, current is generated by separating e-ion or e-hole pairs, depending on whether the medium is a gas or semiconductor, respectively.

When a neutron interacts with a ^{10}B atom in a BF_3 tube the daughter products of the reactions in Eq. 1-1.2 are emitted in opposite directions. Each particle travels to the end of its range in the BF_3 medium, generating a number of e-ion pairs proportional to the amount of energy deposited in the gas. However, not all neutron interactions take place at positions where the entire energy is deposited in the gas; a few interactions take place at positions, near the tube's wall where the trajectory of one of the daughter particles, from the point of interaction to the

tube's wall, is shorter than the particle's range in the gas. Consequently, the particle collides with the tube's wall prior to total energy deposition in the gas. Partial energy deposition in the gas results in a spectrum comprised of energy continua for each of the particles as well as total energy peaks. The particle-wall collisions resulting in the energy continua in the spectrum are referred to as the "wall-effect" (Tsoulfanidis, and Landsberger, 2010). Figure 2-28 is a theoretical depiction of a BF_3 spectrum and shows each of the continua due to all daughter particles from the reactions in Eq. 1-1.2.

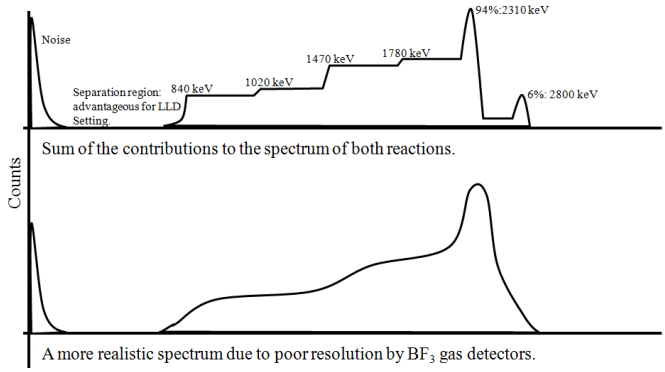

Figure 2-28: Top- A detailed BF_3 tube theoretical spectrum, for a mono-energetic neutron beam showing the energy continua for each of the particles resulting from the reaction in Eq. 1-1.2, as well as the 94% and 6% full energy peaks when neither particles undergo a collision with the wall. Bottom- A more realistic BF_3 tube spectrum lacks the sharp edges due to poor resolution and elevated dead-times at high neutron fluxes.

If the NCM is a thin h-BN layer, which does not possess favorable charge transport properties, and is surrounded by layers or pillars of a semiconductor, then the escaping particles still have energy to deposit in the semiconductor after partial energy deposition in the BN layer. The e-hole pairs generated in the semiconductor are then transported for signal generation. The escaping particles also result in continua of deposited energy in the semiconductor similar to boron lined gas filled detectors.

However, if the semiconductor and the NCM are the same material, eliminating the need for an external semiconductor as is the case for the proposed detector, then the energy continua are due to partial energy deposition in the h-BN layer, analogous to a BF_3 tube. Thus the spectrum resulting from such a detector should bear the same features as a spectrum from a BF_3 tube. The continua are still due to the "wall-effect" and are the results of escapes from the h-BN layer after partial energy deposition rather than collisions with a detector's wall.

Figures 2-29 through 2-34 are smoothed spectra generated by the code for h-BN thicknesses of 0.5, 1, 1.5, 2.5, 3.5, and 7 microns; all the spectra pertain to h-BN with 19.8% ^{10}B, 0.025 eV neutrons, a flux of 6.024×10^{4} $cm^{-2}s^{-1}$ over one minute, and a beam diameter of 1.27 cm totaling 4.5786×10^{6} incident neutrons.

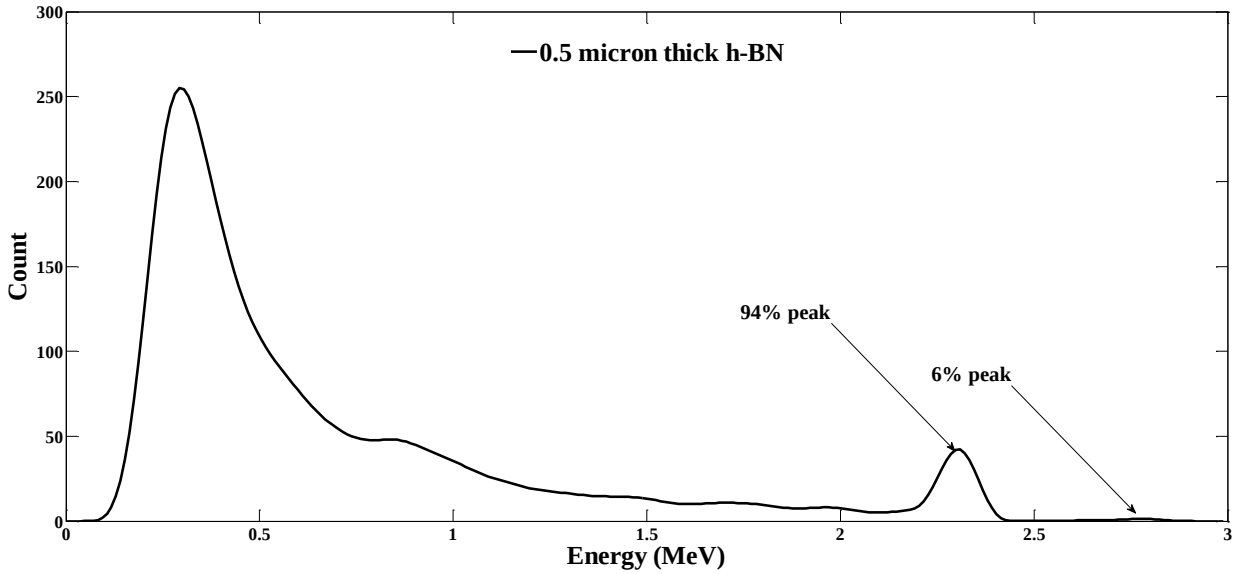

Figure 2-29: Code generated spectrum for a 0.5 μ thick h-BN layer. The first high count peak shows a high probability of escape followed by the energy continua leading to the 94% and 6% peaks which is hardly visible. In such a spectrum, most of the deposited energy seems to be at or slightly higher than the noise level and may be hard to discern between noise and actual signals resulting from neutron absorptions.

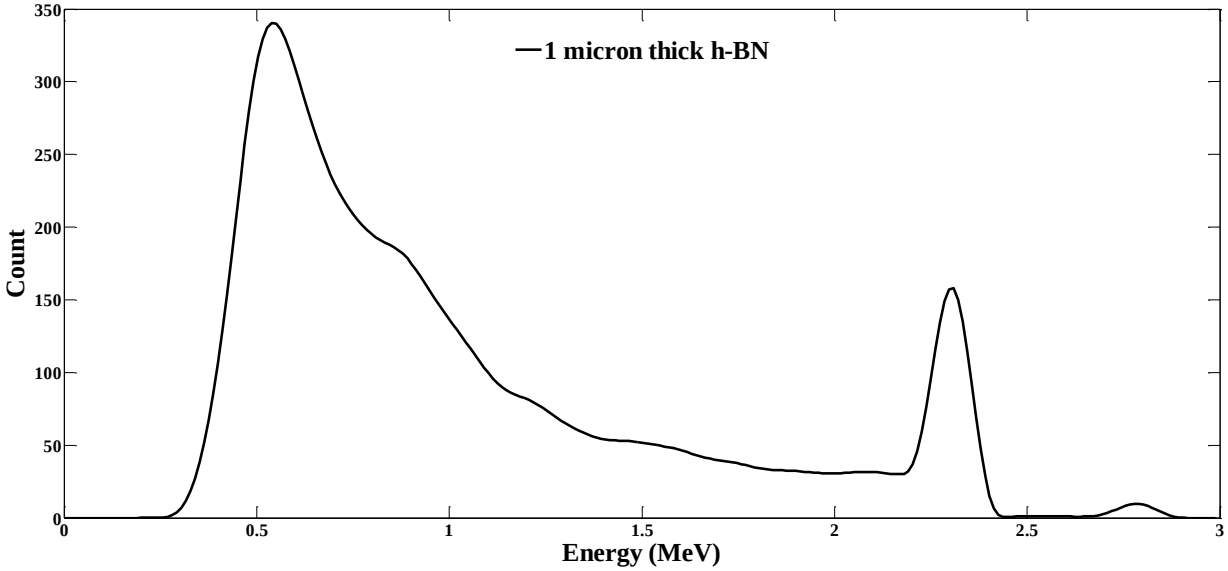

Figure 2-30: Code generated spectrum for a 1 μ thick h-BN layer. The escape peak is still prominent but shifted further up on the energy axis. The 94% peak slightly more prominent than in the 0.5 μ thick layer, and the 6% peak is more visible.

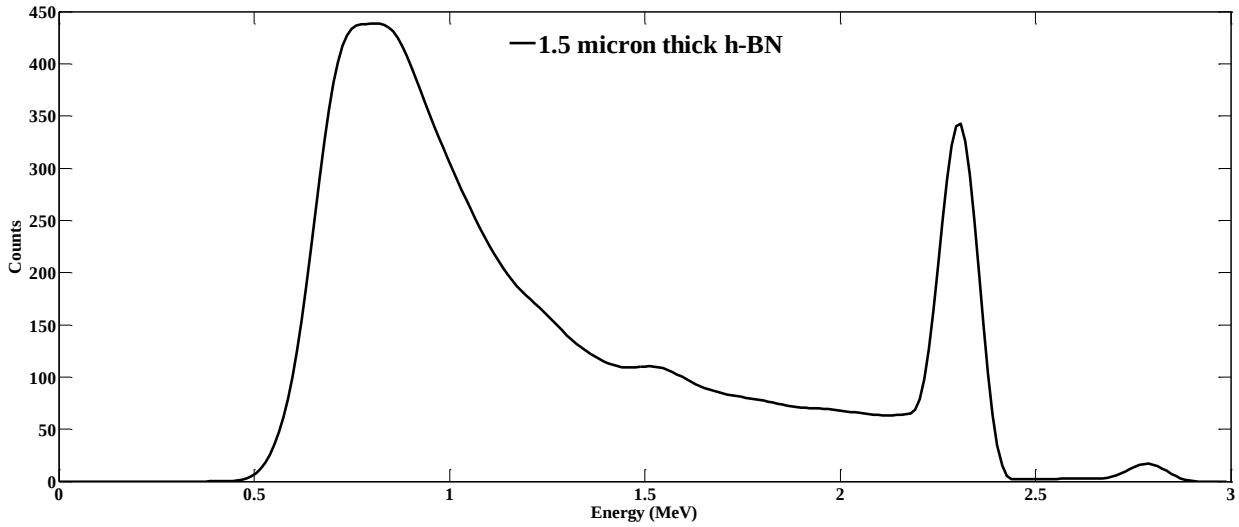

Figure 2-31: Code generated spectrum for a 1.5 μ thick h-BN layer; the escape peak is shifted even farther up the energy axis . The 94% peak is increasing in count, and the 6% peak is clearly visible.

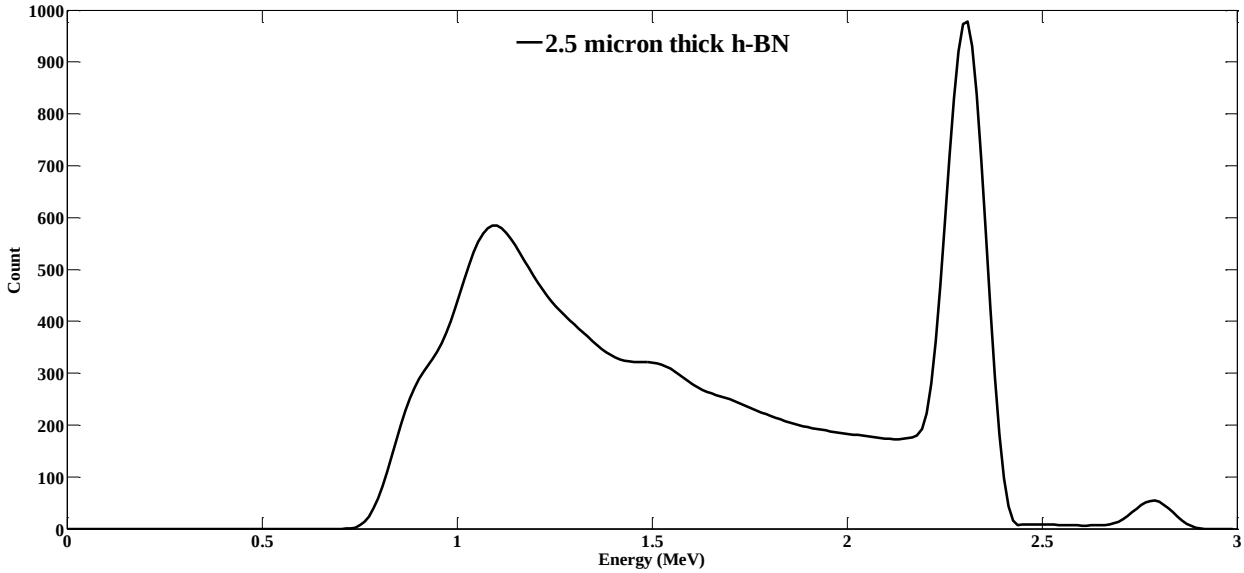

Figure 2-32: Code generated spectrum for a 2.5 μ thick h-BN layer; the escape peak is giving way to the continua.

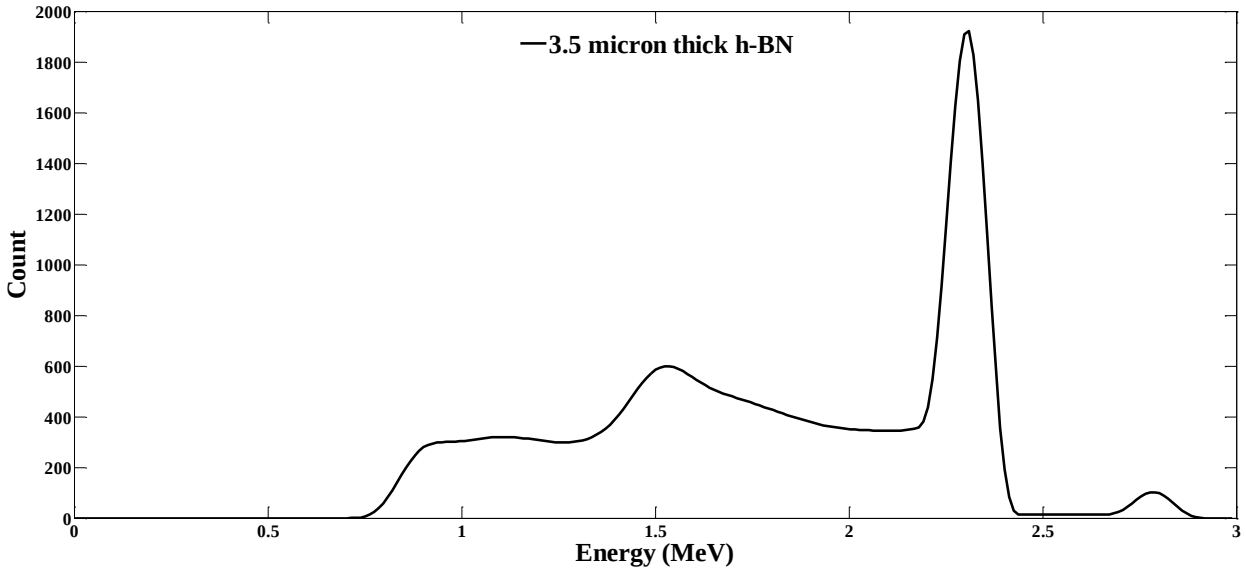

Figure 2-33: Code generated spectrum for a 3.5 μ thick h-BN layer. The escape peak is drastically moved up the energy axis and the beginning of the 840 keV lithium nucleus continuum is already visible.

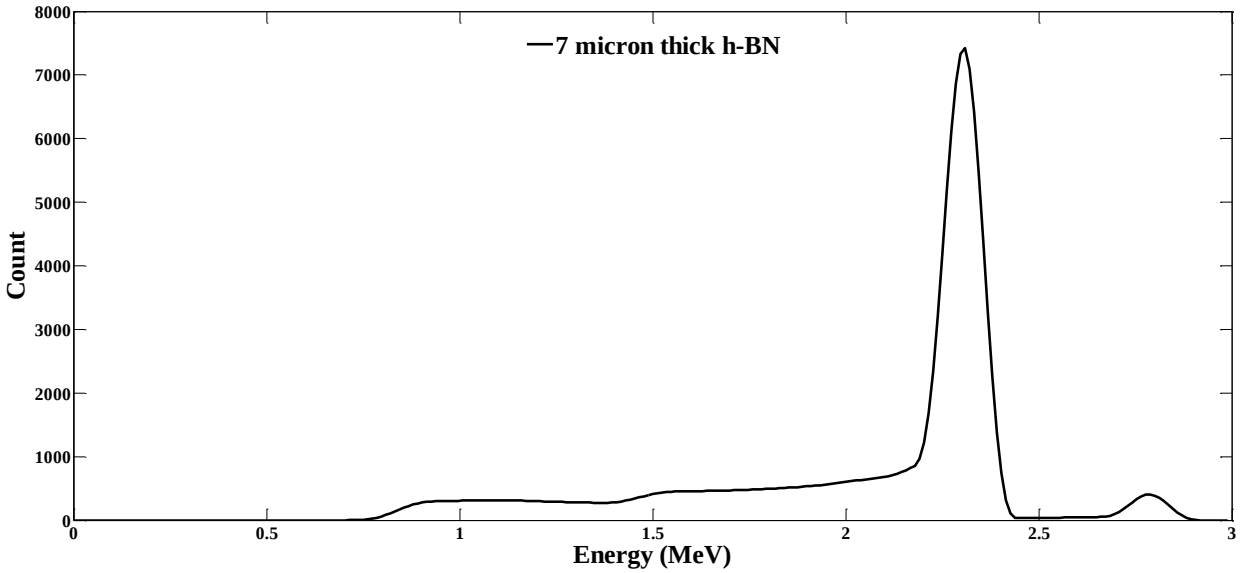

Figure 2-34: Code generated spectrum for a 7 μ thick h-BN layer closely matching the features of the theoretical spectrum in Fig.2-28.

Both the 840 keV lithium nucleus and the 1.47 MeV alpha particle continua appear more prominently than the continua corresponding to the 1.78 MeV alpha particle and the 1.02 MeV lithium nucleus for the latter continua represent only 6% of all interactions. In Fig. 2-28 however, the latter continua were inflated for the purposes of illustration.

The spectra in Figs. 2-29 through 2-34 are the result of smoothing the data generated by the code. Smoothing the data does not affect the total number of counts and was performed for two reasons: 1) smoothing reduces the scale of high peaks to other features in the spectrum by widening the high count features, rendering the low count features of the spectra more visible. 2) The spectra produced by the code are due to perfect energy resolution and do not reflect realistic spectra generated by actual detectors which do not generate spectra with perfect energy resolution. A working detector was not available in order to determine the necessary degree of smoothing, and the degree of smoothing was arbitrarily chosen. Figures 2-35 and 2-36 are, respectively, smoothing illustrations of the 2.5 and the 7 micron thick h-BN spectra showing the differences between the smoothed and the unsmoothed data. The smoothed data in Figs. 2-35 and 2-36 are the same spectra presented in Figs. 2-32 and 2-34.

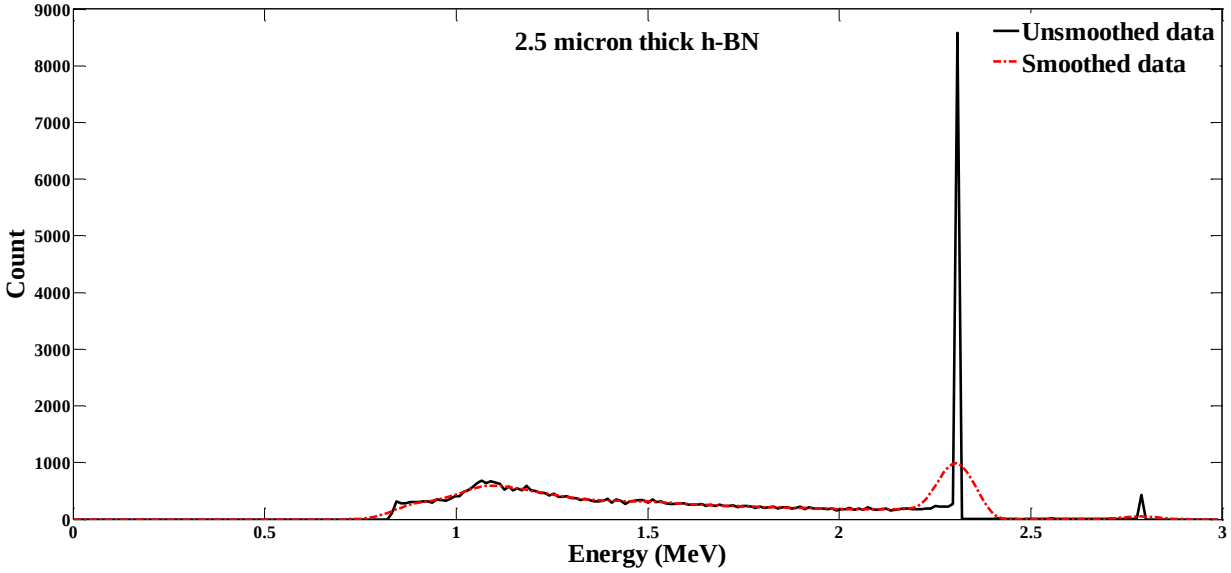

Figure 2-35: Differences between the smoothed and unsmoothed code generated spectra for the 2.5 micron thick h-BN layer.

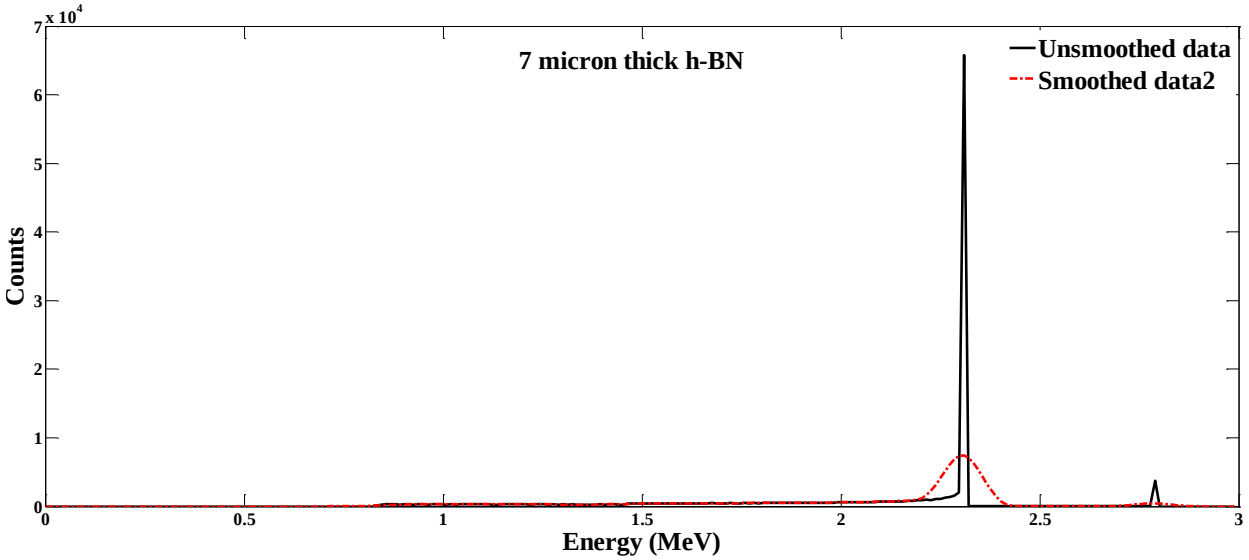

Figure 2-36: Differences between the smoothed and unsmoothed code generated spectra for the 7 micron thick h-BN layer.

In light of the two comparative spectral analyses a conclusion can be made that the code is operating properly and yielding correct, though theoretical, spectral results. Furthermore, the spectra in Figs. 2-29 through 2-36 are simple histograms of energy deposited in the h-BN layer by individual neutron interactions within the layer. The amount of deposited energy directly translates to the number of e-hole pairs generated within the detector's active volume and pulse height. The average energy of the particles resulting from the $^{10}B(n,\alpha)^{7}Li$ reaction is given by

$$E_{AV} = (0.94 \times 2.31)\,\text{MeV} + (0.06 \times 2.8)\,\text{MeV} = 2.3394\ \text{MeV}. \qquad 2\text{-}4.13$$

Based on Eqs. 2-4.1 through 2-4.4 and the corresponding figures, not every neutron interaction deposits the total energy of the particles within the h-BN slab. The code was run for thicknesses from 0.5 μ to 36 μ in intervals of 0.5 μ, and the total deposited energy of all absorbed neutrons was averaged over the number of absorbed neutrons and is shown in Fig. 2-37 (a) is the average energy deposited per neutron absorption, and (b) is a plot of the percentage energy deposition of the average energy value in Eq. 2-4.13 per absorbed neutron. The code was run with the same parameters used to generate the spectra in Fig. 2-29 through Fig. 2-34.

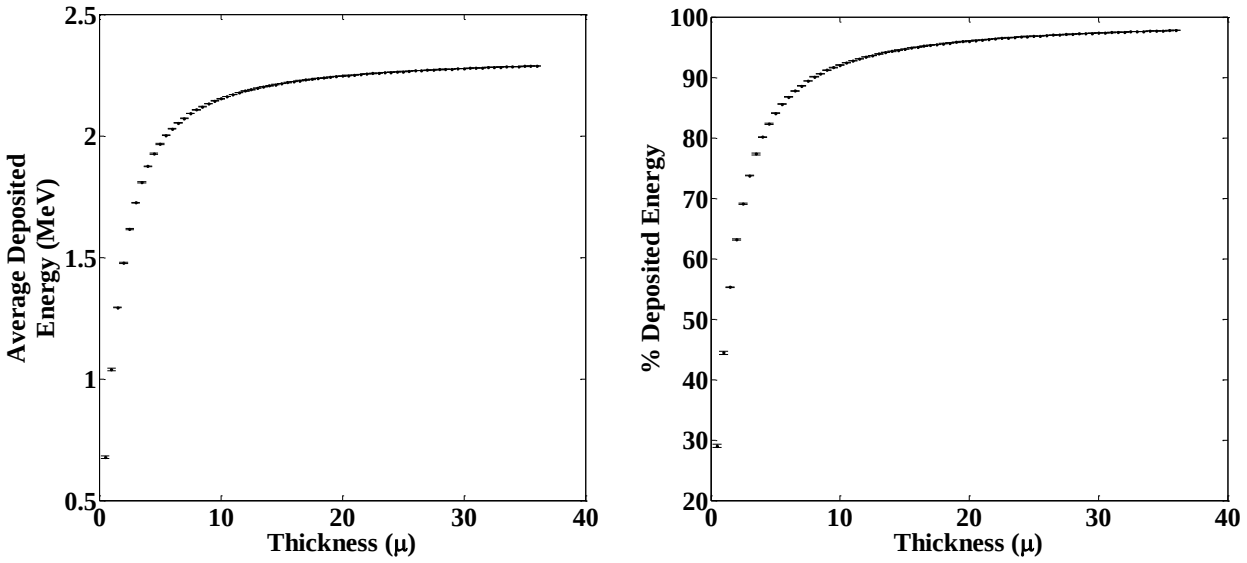

(a) (b)

Figure 2-37: (a)-Best case average energy deposition per neutron absorption in h-BN made from natural boron with a 0.198 ^{10}B enrichment fraction. (b)-Percent energy deposition per absorbed neutron based the average energy of the ^{7}Li nuclei and the alpha-particles in Eq. 2-4.13.

For both figures in Fig. 2-37 the average was calculated five times for each thickness then the mean and standard deviation was then calculated based on the five values and the error bars represent the error in the average. On the other hand, it would also be useful to calculate the average deposited energy and the percent deposited energy, once per thickness, and then determine the distribution of the deposited energy about the average deposited energy as shown in Figs. 2-38 and 2-39. Basically, Figs. 2-38 and 2-39 represent the same set of calculated data. However, since the standard deviation is usually plotted symmetrically about the average, the upper error limit of the data was higher than the highest allowed value in some cases as is clear in Fig. 2-38. Consequently, the upper error limit was truncated down to the maximum allowed values and is represented in Fig. 2-39.

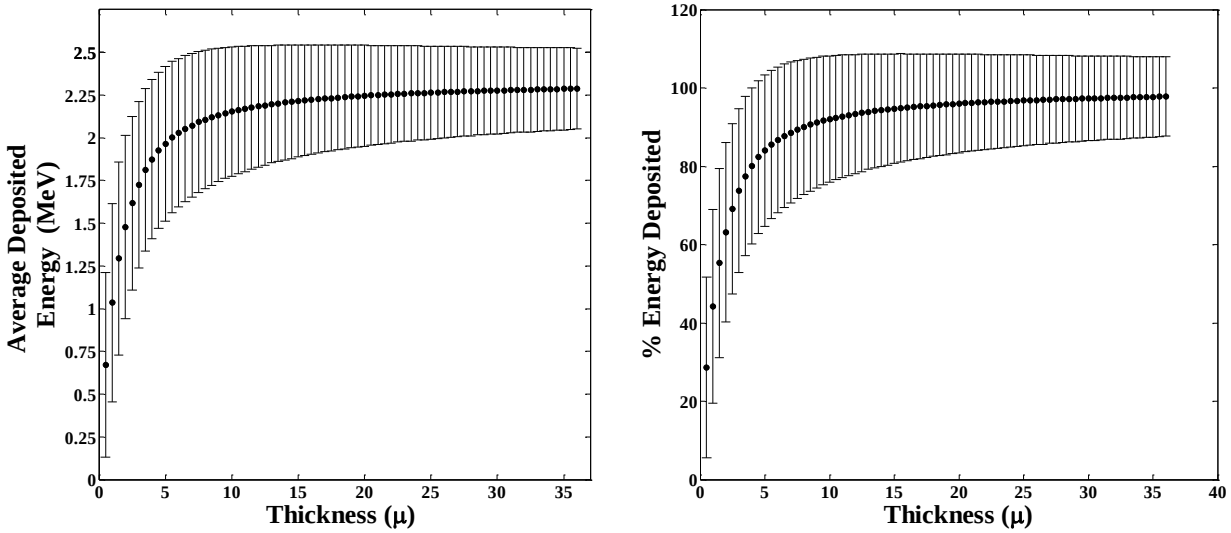

(a) (b)

Figure 2-38: Error about the average energy deposition where the average deposited energy and percent energy deposited as calculated by the code clearly show upper limit error values above allowed maximum average energy of Eq. 2-4.13 and error percentages higher than 100%.

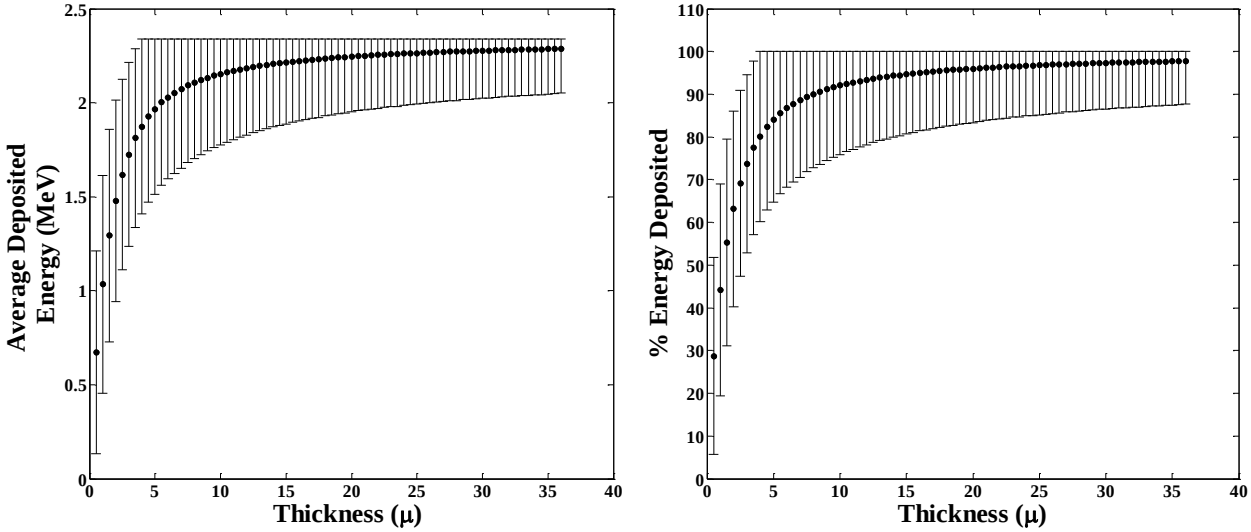

(a) (b)

Figure 2-39: Upper limit error values in Fig. 2-38 truncated to maximum allowed values.

The Absorption Fraction

The absorbed fraction of neutrons impinging on an h-BN slab generated by the code must also be verified against Eq. 1-2.7, for the efficiency of a detector largely depends on the absorbed fraction. Furthermore, the validation enables efficiency calculation prediction. Absorption data generated by the code for h-BN thicknesses from 0 to 1000 microns and 0.198 enrichment and

the same code parameters used to generate the spectra in Figs. 2-29 through 2-34 verses Eq. 1-2.7 is shown in Fig. 2-40.

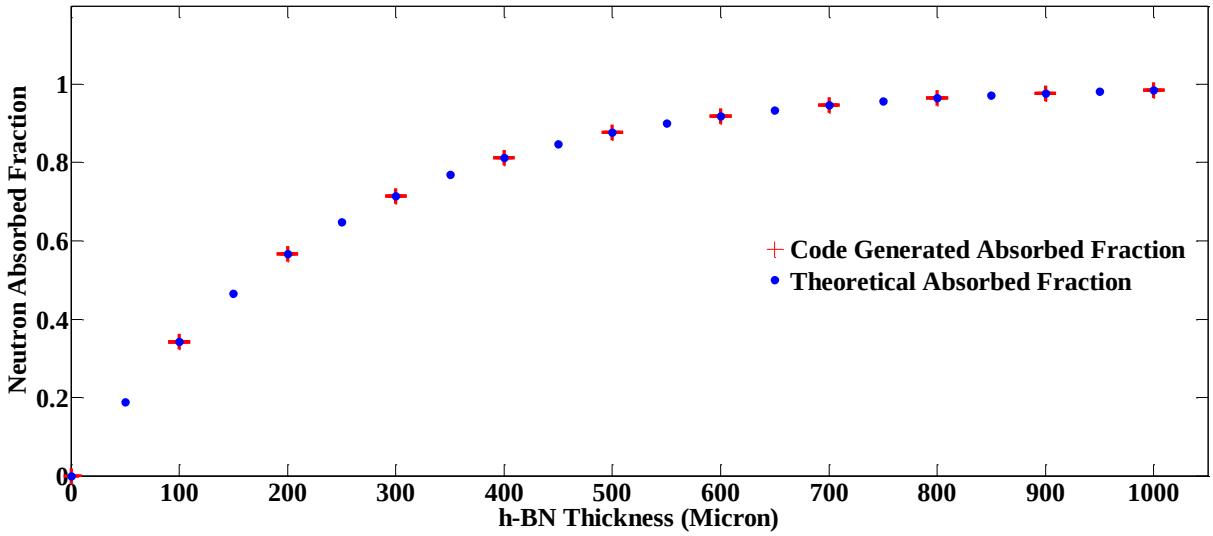

Figure 2-40: Code generated absorption data against theoretical absorption data—Eq.1-2.7—for h-BN made from natural boron with a 0.198 ^{10}B enrichment fraction.

Chapter 3 - Experimentation

In addition to the determination of the utility of the crystals synthesized by the Chemical Engineering team as suitable detector NCM's, and assessing the detector fabricated at TTU; the MNE team at KSU independently investigated the feasibility of and radiation damage in pyrolytic h-BN. In total, the MNE Team at KSU conducted four experiments.

I — Radiation damage in pyrolytic h-BN caused by neutron irradiation was assessed. Selected pyrolytic h-BN samples were tested for neutron response. A similar experiment with the same steps up to neutron response testing was previously conducted (McGregor et al, 2008), but damage was not assessed.

II — Testing a neutron detector fabricated from a single domain crystal synthesized by the Chemical Engineering team at KSU.

III — Testing a neutron detector fabricated from a boron chromium nickel alloy—dubbed the Robin's Egg—with microscopic h-BN crystals deposited on the surface of the alloy.

IV — Assessment of the thin film h-BN detector fabricated at TTU.

Furthermore, for all of the experiments, determining the neutron detection efficiency of any detector/sample was contingent upon a positive neutron response. Screening for neutron response was first conducted at the Southeast beam located in the reactor facility at KSU. Efficiency determination, when necessary, was to be conducted at S.M.A.R.T. laboratory's monoenergetic—0.025 eV—diffracted neutron beam also located in the reactor facility at KSU.

Section 3.1: Generalities

To avoid redundancy, common aspects, procedures, calculations, and equipment employed in this work are presented independently.

Equipment and Circuit Block Diagram

The equipment used in these experiments is listed in Table 3-1. Figure 3-1 is a schematic diagram of the equipment set-up. Equipment settings for the individual experiments are tabulated in each of the experiments' sections.

Table 3-1: Equipment at the Southeast Beam of the reactor facility at KSU.

Unit description	Brand	Model
High voltage power supply (HVPS)	ORTEC	456
Preamplifier	ORTEC	142A
Amplifier	CANBERRA	2022
Multichannel analyzer (MCA)	APTEC	EAGLE/CLASSIC
Oscilloscope (OS)	AGILENT TECHNOLOGIES	DS01024A

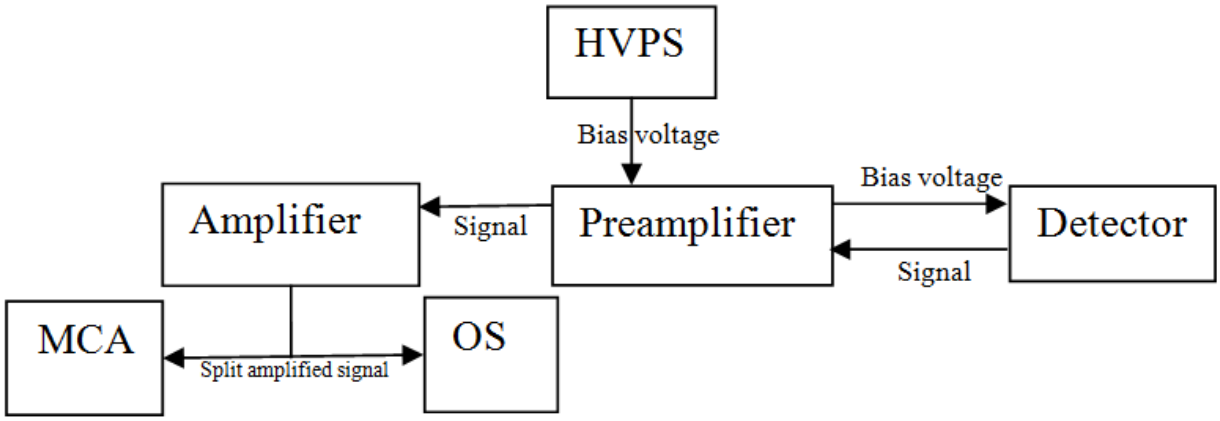

Figure 3-1: General block of the circuit used in all experiments and both equipment sets, where the box labeled detector represents any sample/detector undergoing the procedure.

Neutron Response

All detector/samples were tested for neutron response as a preliminary to efficiency determination and validation.

In order to ensure the sound operation of the equipment in Table 3-1 and the circuit in Fig. 3-1, a verified neutron detector was connected to the circuit and exposed to the neutron

beam prior to the conduction of any experiment. The step insures the equipment's sound operation should the detector being tested fails to respond to neutrons.

The southeast beam was collimated down to a diameter of half an inch by means of a layered shield. The shield was comprised of two inches of bakelite for fast neutron thermalization followed by two inches of borated polyethylene for thermal neutron absorption. The final layer is two inches of lead to suppress/scatter γ-rays from the first reaction in Eq. 1-1.2. A half inch hole was then drilled through the layered assembly restricting the beam to the half inch hole. The collimated beam's thermal and fast neutron flux were determined using copper NAA where upon neutron absorption by ^{63}Cu the activated ^{64}Cu emits annihilation photons with a branching ratio of 0.35. The fast and thermal fluxes were calculated to be 474.78 cm $^{-2}$s $^{-1}$ and 21.7 cm $^{-2}$s $^{-1}$ per kW of reactor power, respectively; neither flux is monoenergetic. With a 21.87:1 thermal to fast neutron flux ratio the beam is ideal for thermal neutron response experimentation where the thermal neutron spectrum follows a Maxwellian distribution.

Neutron response testing involved biasing the detector/sample as shown in Fig. 3-1 and aligning the detector with the collimated beam. As far as simple neutron response testing is concerned, where the objective is not efficiency determination, careful angular alignment of the detector with the beam to satisfy Eq. 2-3.5 with ϕ = 0 for maximum areal exposure is not necessary.

Efficiency: Procedure and Formulation

With a sample/detector oriented perpendicular to the diffracted monoenergetic thermal neutron beam, Eq.2-3.5 reduces to Eq. 3-1.1 with $\phi = 0$ and $\cos(\phi) = 1$

$$\varepsilon_i = \frac{R_{\text{detector}}}{I\text{A}_{\perp}} \qquad 3\text{-}1.1$$

When a detector with a known efficiency ε records R counts, the number of neutrons N impinging on the detector per unit time and area is given by Eq. 3-1.2.

$$N = \frac{R}{\varepsilon} \qquad 3\text{-}1.2$$

If the area of the beam impinging on the detector is less than the detector's area facing the beam, then *N* is the neutron flux in the beam, which is constant regardless of the detector placed in the beam's path. The diffracted beam at KSU has a diameter of 1.27 cm (McGregor and Shultis, 2011), thus placing a ^{3}He tube with a 5 cm diameter covers the beam. The ^{3}He is known to have an intrinsic beam efficiency $\equiv \varepsilon_i$ of 85%. With the thermal neutron flux in the beam considered statistically constant over time, then the total number of neutrons, N_{total}, in the beam is

$$N_{\text{Total}} = \frac{R^{^3\text{He}}}{\varepsilon_{i_{\text{beam}}}^{^3\text{He}}} = \frac{R^{\text{detector}}}{\varepsilon_{i_{\text{beam}}}^{\text{detector}}} \quad . \tag{3-1.3}$$

Correcting for the difference in area between the detector being evaluated and the ^{3}He tube, or in this case the beam's area, for the beam's diameter is smaller than the ^{3}He tube's diameter, the intrinsic beam efficiency of the detector can be formulated by Eq. 3-1.4

$$\varepsilon_{i_{\text{beam}}}^{\text{Detector}} = \frac{R^{\text{detector}}}{R^{^3\text{He}}} \frac{\text{A}^{\text{beam}}}{\text{A}_{\perp}^{\text{detector}}} \varepsilon_{i_{\text{beam}}}^{^3\text{He}} \tag{3-1.4}$$

Current Voltage Curves and Conductivity Measurements

All samples used in Experiments I were subjected to current-voltage curve IV-curve measurements. Recording IV-curves requires a voltage sweep, usually symmetric about zero volts, from a negative voltage to a symmetric positive voltage with the current measured at each voltage. For semiconductor devices the IV-curve reveals the bias conditions for the particular device. If a device has a *pn* junction or a Schottky contact, the IV-curve will bear diode characteristics; on the other hand, the IV-curve also reveals Ohmic contacts. Figure 3-2 is an example of an ohmic IV-curve belonging to a pyrolytic h-BN sample bearing the nearly constant slope characteristic of a resistor.

Another property revealed by an IV-curve is the electrical conductivity; where pre-and post-neutron irradiation conductivity changes reveal the fashion by which a sample's electrical properties are affected by irradiation. For conductivity measurements the original IV data are inverted placing voltage on the vertical axis and current on the horizontal axis, where the resistance is the slope of the curve. Eq. 3-1.5 is the formula for conductivity.

$$\text{Conductivity} \equiv \sigma_I = \frac{\ell}{\text{AR}}\ \text{S}\cdot\text{m}^{-1}, \qquad 3\text{-}1.5$$

where ℓ is the path-length the current encounters through the sample, A is the sample's area perpendicular to the current's path, and the resistance, R, is the slope—dV/dI—of the inverted IV curve. The units of conductivity are Siemens per meter and the symbol σ is commonly used; however, for the purposes of avoiding confusion with the microscopic cross-section symbol, σ for conductivity will be represented with the subscript I denoting electrical current.

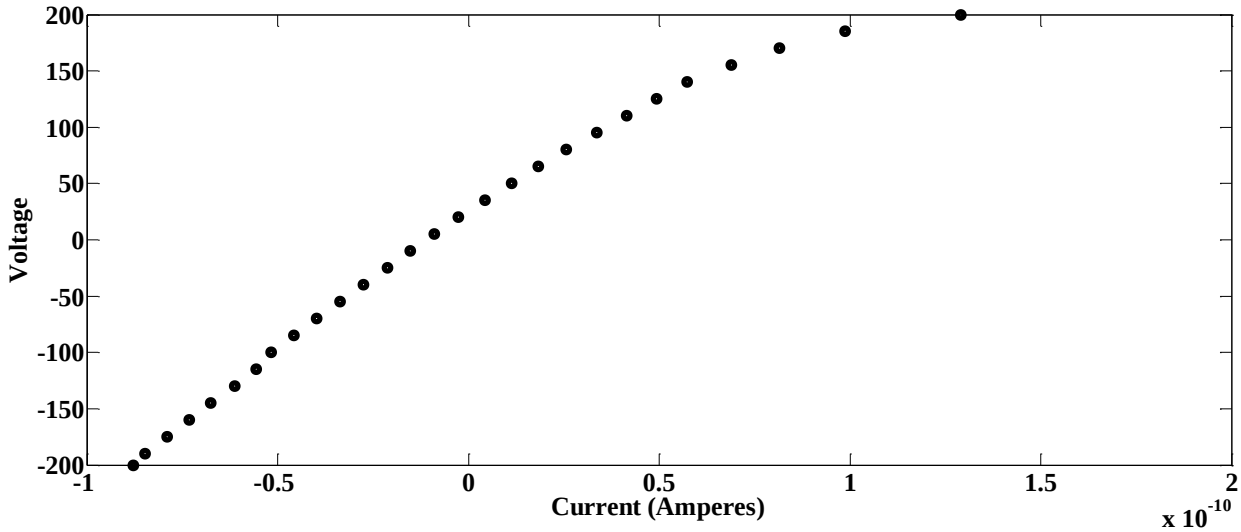

Figure 3-2: An example of an inverted IV-curve where the slope is the resistance of the h-BN sample.

Section 3.2: Experiment I

Twenty five pyrolytic h-BN samples were used in two batches of fifteen and ten samples respectively for experiment I. The second batch was not part of the original experiment; however, post neutron irradiation conductivity measurements of the first batch showed an abrupt increase in conductivity at around a neutron fluence of 10^{12} cm^{-2} . The second batch was irradiated at neutron fluences about the fluence point where conductivity abruptly increased in the first batch in order to observe a smoother transition in conductivity.

A few irradiated h-BN samples were studied using photoluminescence (PL) band-gap analysis at TTU. PL will not be discussed further in the current chapter, because the procedure was performed at TTU's facilities and was not performed by the MNE team at KSU. However,

Pl analysis should reveal pre and post irradiation bandgap energy changes. If energy changes are detected via PL and the energy peaks can be identified, then energy bandgap changes may indicate the type of damage resulting from irradiating h-BN with neutrons.

Sample Preparation and Irradiation

A 3 cm by 5 cm by 1 mm thick slab of pyrolytic h-BN was fastened with wax onto a thick ceramic block and cut into thirty-two 5 ± 0.5 mm by 5 ± 0.5 mm by 1 mm thick squares on a diamond wire saw under a flowing stream of mineral spirits for lubrication. The samples were then placed in boiling water to remove the fastening wax. Sample cleaning involved four stages of fifteen minute sonic baths in four different solvents where each successive solvent removes the previous solvent, while the first solvent removes grease and mineral spirits. The stage respective solvents are: acetone, isopropyl alcohol, methanol, and finally de-ionized water. The samples were then inserted into a multi-pocket shadow-mask with 3 mm to 4.5 mm diameter openings and placed in an electron beam evaporator where metal contacts were deposited on the samples. Each contact consisted of 500 Å of titanium followed by 20,000 Å of aluminum on each side of the p-BN samples. All steps in sample preparation took place in S.M.A.R.T laboratory's facilities at KSU.

A single sample from the first batch was not irradiated; the rest were irradiated in the central thimble of the TRIGA MARK II reactor at KSU at successively increasing neutron fluences. One at a time, the samples were placed inside an aluminum vial alongside a small steel sample, as a standard, whose mass was recorded. Upon withdrawal from the central thimble, the steel sample was placed on a high purity germanium γ-ray detector (HPGE) for neutron activation analysis (NAA) which permits the determination of the total neutron fluence (Φ)—the sum of the thermal and fast fluences—the sample was exposed to as shown in Eq. 3-3.1.

$$\Phi_{th}\bar{\sigma}_{th} + \Phi_{Fast}\bar{\sigma}_{Fast} = \frac{A\mathrm{A}_{\mathrm{Fe}}}{6.023\times10^{23}\cdot10^{-24}\cdot\lambda_{^{59}\mathrm{Fe}}mf_{^{58}\mathrm{Fe}}} \qquad 3\text{-}3.1$$

where $\bar{\sigma}_{Th}$ and $\bar{\sigma}_{Fast}$ are the averaged thermal and fast microscopic cross-sections of ^{58}Fe in barns, respectively, Φ_{Th} and Φ_{Fast} are the thermal and fast fluences, respectively, *m* is the steel

sample's mass in grams, $f_{^{58}\mathrm{Fe}}$ is the mass abundance fraction of $^{58}\mathrm{Fe}$ and is 0.282%. *A* in Eq. 3-3.1 is the activity of the resulting $^{59}\mathrm{Fe}$ in becquerel where $\text{total counts} \equiv C_{Total} = \sum_{n=1}^{N} n_i$ where n_i is the net number of counts under peak *i*, and C_{Total} is the sum of all counts under all the pertinent peaks. There are two γ-ray energy peaks resulting from the activity of ^{59}Fe: 1.095 MeV and 1.292 MeV γ-rays where the branching ratios are 0.56 and 0.44, respectively. The software controlling the detector calculates the total activity by dividing the detector's efficiency, ε, multiplied by the counting time, *t*, into the total counts under a peak or $A = C_{Total} / (\varepsilon t)$. The decay constant of the active isotope, $^{59}\mathrm{Fe}$,in s^{-1} is $\lambda_{^{59}\mathrm{Fe}}$, A_{Fe} is the elemental atomic mass of iron (58.845 grams/mole), 10^{-24} $\mathrm{barn}^{-1} \cdot \mathrm{cm}^2$ is the barn to cm^2 conversion factor, and 6.023×10^{23} is Avogadro's number atoms/mole. The neutron fluences the samples in batches one and two were exposed to are shown in Fig. 3-3. The derivation of Eq. 3-3.1 is shown in the following sequence of equations.

$\text{Activity} \equiv A = \lambda_{^{59}\mathrm{Fe}} N^{59}$, yielding $N^{59} = A / \lambda_{^{59}\mathrm{Fe}}$ where N^{59} is the total number of ^{59}Fe atoms in the sample. Considering the generation of an atom of ^{59}Fe is the result of an atom of ^{58}Fe absorbing a neutron; the number of ^{59}Fe atoms generated is the number of ^{58}Fe atoms present in the sample multiplied by the total number of neutrons per unit area—neutron fluence (flux multiplied by irradiation time)—which impinged on the sample and the sum of the averaged fast and thermal microscopic cross-sections converted to cm^2 and given by

$$N^{59} = N^{58} t_{(\text{irradiation time})} \left(\phi_{th} \bar{\sigma}_{th} + \phi_{Fast} \bar{\sigma}_{Fast} \right) \times 10^{-24} \qquad 3\text{-}3.2$$

Implying

$$t_{(\text{irradiation time})} \left(\phi_{th} \bar{\sigma}_{th} + \phi_{Fast} \bar{\sigma}_{Fast} \right) \equiv \Phi_{th} \bar{\sigma}_{th} + \Phi_{Fast} \bar{\sigma}_{Fast} = \frac{N^{59}}{N^{58} \times 10^{-24}} \qquad 3\text{-}3.3$$

where N^{58} is given by Avogadro's number multiplied by the mass of the sample and the mass abundance fraction of ^{58}Fe all divided by the elemental atomic mass of iron as shown in Eq. 3-3.4

$$N^{58} = \frac{6.022 \times 10^{23} m f_{^{58}\mathrm{Fe}}}{\mathrm{A}_{\mathrm{Fe}}} . \qquad 3\text{-}3.4$$

Substituting Eq. 3-3.4 into Eq. 3-3.3 leads to

$$\Phi_{th}\bar{\sigma}_{th} + \Phi_{Fast}\bar{\sigma}_{Fast} = \frac{N^{59}\mathrm{A}_{\mathrm{Fe}}}{6.022\times10^{23}\cdot10^{-24}mf_{^{58}\mathrm{Fe}}}, \qquad 3\text{-}3.5$$

and then substituting $N^{59} = A/\lambda_{^{59}\mathrm{Fe}}$ into Eq. 3-3.5 yields Eq. 3-3.1. Decay corrections for counting, irradiation, and waiting times were not included in Eq. 3-3.1, for the half-life of ^{59}Fe is 44.5 days and the process, from the beginning of irradiation until the end of counting, lasted less than two days rendering Eq. 3-3.1 a good approximation of the true neutron fluence the samples were exposed to.

The units of the RHS of Eq. 3-3.1 workout to $\mathrm{barn}\cdot\mathrm{atom}^{-1}\cdot\mathrm{cm}^{-2}$ as follows

$$\frac{\mathrm{neutrons}\cdot\mathrm{s}^{-1}\cdot\mathrm{g}\cdot\mathrm{mole}^{-1}}{\mathrm{atom}\cdot\mathrm{mole}^{-1}\cdot\mathrm{barn}^{-1}\cdot\mathrm{cm}^{2}\cdot\mathrm{s}^{-1}\cdot\mathrm{g}} = \mathrm{barn}\cdot\mathrm{atom}^{-1}\cdot\mathrm{cm}^{-2}. \qquad 3\text{-}3.6$$

While the units of the microscopic cross-sections in the LHS of Eq. 3-3.1 are $\mathrm{barn}\cdot\mathrm{atom}^{-1}$. Cancelling similar units from the LHS and the RHS of Eq. 3-3.1 results in the units of fluence, $\mathrm{neutrons}\cdot\mathrm{cm}^{-2}$, leftover on the RHS of Eq. 3-3.1.

Furthermore, a single independent sample was irradiated up to a fluence of approximately 9×10^{14} neutrons for the purposes of increased lithium buildup, where the increased lithium concentration may act as a *p* dopant. The sample was thermally annealed to restore order to the lattice with lithium may be an interstitial impurity. To avoid melting the aluminum contacts the annealing temperature was kept below 600^{o}C. (Watanabe et al, 2006) reported the restoration of stacking orders[16] to mechanically damaged h-BN upon annealing the h-BN at temperatures around 2000^{o}C for three hours. However in the present study boron atoms are burned-up in the process and are not replaced by annealing. Thus deformities due to the missing atoms will inevitably remain. Furthermore, whether annealing at 600^{o}C restores order is unclear, and future PL analysis on similarly processed samples may reveal whether annealing at 600^{o}C restores order.

[16] Plane slippage deforming the hexagonal lattice.

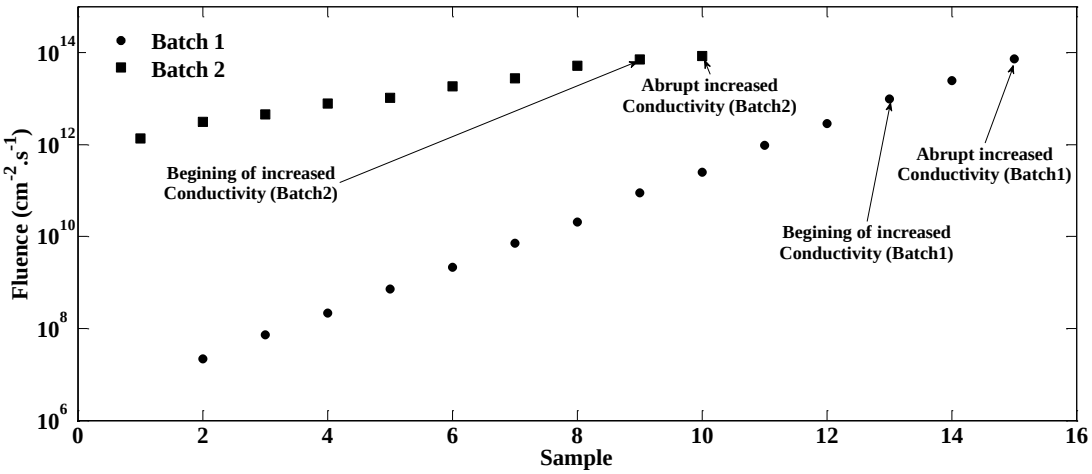

Figure 3-3: The neutron fluences the pyrolytic h-BN samples in batches one and two were exposed to.

Pre-and post-irradiation IV curves were recorded from -200 V to 200 V in a dark box for all samples in both batches. For each of these samples conductivity was determined using Eq. 3-1.5.

Sample Biasing Apparatus Construction

Testing the samples for neutron response involves biasing the samples at a certain voltage in order to collect opposite charges as earlier described in Section 2.2: Semiconductors and Neutron Detection. The apparatus used for biasing is a simple construction described as follows.

A 1 ¼ inch by 1 inch by ½ inch block of bakelite was super-glued on one side of a 2 inch by 1 ¼ inch 1 mm thick copper sheet. A hole sufficient for an 8-32 tap was drilled into one of the 1 inch by ½ inch surfaces of the bakelite. A copper leaf spring was then attached to the bakelite with an 8-32 screw; the copper spring was bent towards the copper sheet to the point where around a 0.25 mm gap was maintained between the spring and the copper sheet where the 1 mm thick samples would be inserted. Both sides of the gap—spring and copper sheet—were smeared with silver and indium free molten solder which was left to cool and harden; the flat surfaces of the hardened solder produce a more evenly distributed and cleaner electrical contact on both sides of the inserted samples. The exposed side—bakelite free side—of the copper sheet was then fastened to the floor of a 6 inch by 3 inch by 1 ½ inch aluminum box by double-sided tape. The copper sheet was then grounded by a bare copper wire connected to the aluminum box. The

spring would then be held at the bias voltage generating an electric field through any sample placed in the gap between the two conductive surfaces. The apparatus holding a non-irradiated sample is shown in Fig. 3-4. A ½ inch hole was then drilled in the containing aluminum box's cover and the detector was fastened with the sample aligned with the drilled hole; the hole was then covered with aluminum tape to reduce electromagnetic noise.

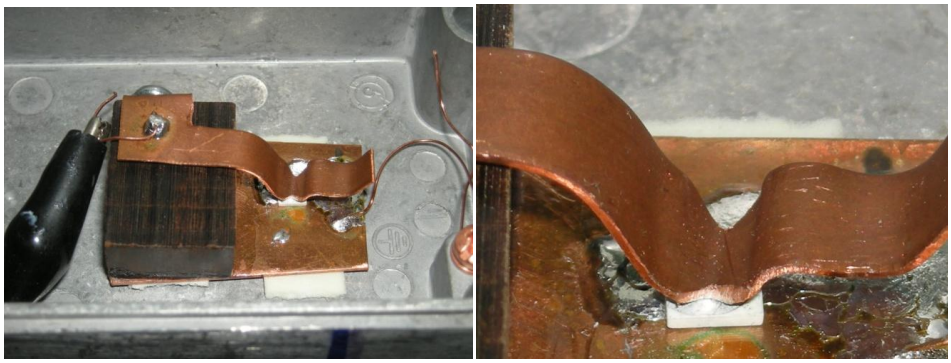

(a) (b)

Figure 3-4: The apparatus—detector—used in experiment I. (a)-The detector with ground connection to the aluminum box and bias voltage on the leaf spring. (b)-A sample held between the grounded copper sheet and the spring held at a potential.

Neutron Response

Table 3-2 lists the selected samples tested for neutron response from batch one along with the fluences the samples were exposed to.

Table 3-3 lists the equipment's settings used for the selected samples from experiment I.

Table 3-2: Samples selected from batch one for neutron response testing on the Southeast Beam. Testing was performed at 50 kW of reactor power and 1800 seconds counting time.

Sample	Irradiation Fluence (cm^{-2})
1	0
6	$2.1549\times10^{9}\pm4.621\times10^{4}$
13	$9.7593\times10^{12}\pm3.1241\times10^{6}$

Table 3-3: Circuit settings for neutron response testing of the selected samples used in Experiment I from batch one. The percent LLD is the percent of the ULD (highest channel) the LLD is set at.

Amplifier gain	Times 300
MCA Lower level discrimination (LLD)	Channel 250 or 3.05% of the total channels
MCA Upper level discrimination (ULD)	Channel 8192
Bias Voltage (V)	600

Section 3.3: Experiment II- A Single Crystal h-BN Domain

The Chemical Engineering team at KSU synthesized a polycrystalline h-BN sample with a large triangular single crystal domain within the sample. The dimensions of the triangular single crystal domain shown in Fig. 3-5 are approximately 2 mm across the triangle's base and 4 mm in height. The entire sample's thickness was on the order of tens of microns which, compounded with the fragility of the sample, rendered the sample extremely delicate for traditional detector construction using the sample as the neutron conversion medium.

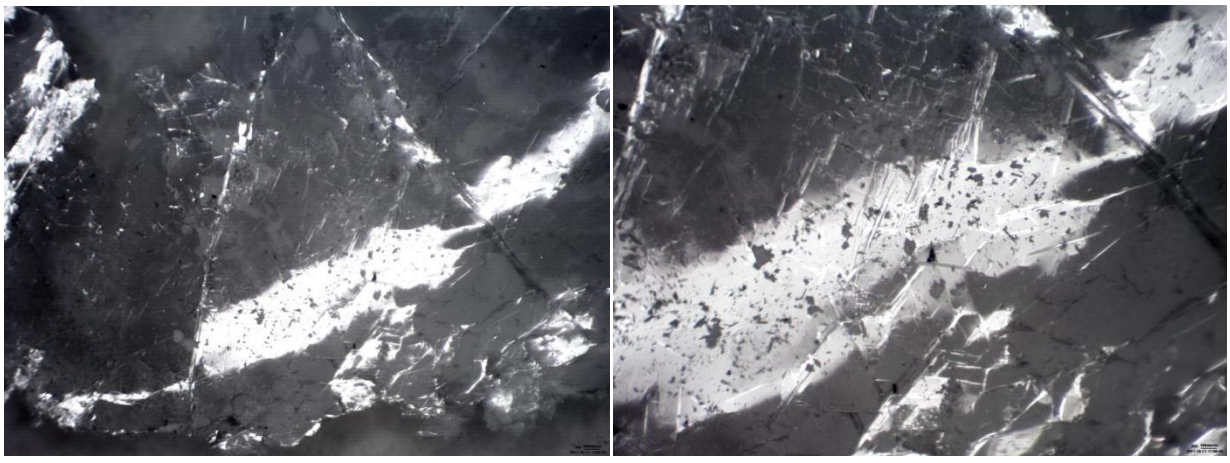

(a) (b)

Figure 3-5: (a)-A 2 mm base and 4 mm height triangular h-BN single crystal domain within a polycrystalline matrix. (b)-A magnified view of the domain showing structural defects in the form of localized ridges. The Chemical Engineering Team confirms single crystalline structure of the domain through Raman spectroscopy.

Sample Adaptation for Neutron Response Testing

"A single [h-BN] crystal has surfaces with predominant cleavage at *c* facets along the layers, and it is easily collapsed by mechanical perturbations causing the layers to glide along the surface" (Watanabe et al, 2006).Thus the sample's fragility did not allow the application of any appreciable physical pressure and the use of the detector apparatus used in Experiment I would destroy the domain. Instead the sample had to be biased laterally rather than through the thickness of the domain. Even then, the sample was too fragile for direct connections with copper wires.

The sample was fastened onto a bakelite block with wax, a molten drop of wax which hardened after the sample was deposited on the bakelite block, to support and strengthen the sample. The tips of two bare copper wires were then laid on opposite sides of the triangle, one on the top vertex, and the other on the mid-point of the base as shown in Fig. 3-6 (a). Silver conductive epoxy was then applied to the wire tips and slightly smeared to cover a small area of the domain creating two electrical contacts on opposite sides of the domain. The copper wires were then taped to the bakelite block to avoid accidental disconnection while the block was being mounted. Upon hardening of the silver conductive epoxy, black silicone was used to cover the gap between the two electrical contacts in order to avoid false signals due air ionization. The block was glued on the inside wall of a steel box with the sample facing outward toward a hole in the box. The hole in the box was covered with aluminum tape for electromagnetic noise reduction. Figure 3-6 (a) shows the sample mounted on the bakelite block and the block mounted in the steel box is shown in Fig. 3-6 (b).

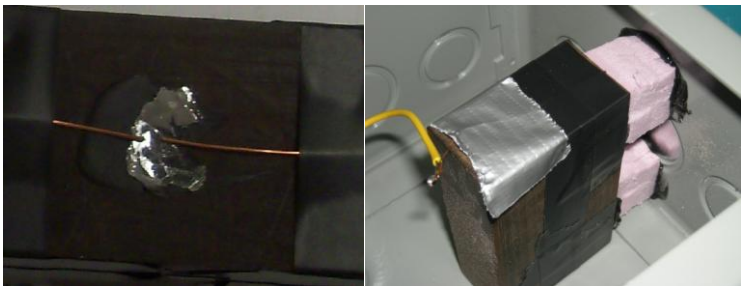

(a) (b)

Figure 3-6: (a)-The single crystal domain mounted on the bakelite block on top of cooled wax with the two copper wire tips laid on the vertex and base of the domain; the wire tips were then covered with conductive epoxy to establish electrical contacts between the domain and the wire tips on each end of the domain. (b)-The bakelite block mounted inside the steel box.

The steel box was mounted on a clamp which was in turn mounted on a stand; the mount was oriented in such geometry where the hole in the box would, within approximation, perpendicularly face the diffracted beam in the reactor facility at KSU, exposing the sample to thermal neutrons emanating from the reactor core. Table 3-4 lists the equipment settings used in testing the sample for neutron response; reactor power was 250 kW and the counting time was 900 seconds. The count was preceded by a background count lasting 900 seconds with the reactor shut off, and followed by a background count lasting 900 seconds with the reactor still running at 250 kW but with a 2 mm cadmium shutter inserted between the beam's emanation point and the detector. Running the two background counts before and after the counts was, in the current case, performed to insure whether the running reactor contributed to electromagnetic noise. Thus there were three spectra associated with the sample. The step was not performed for following experiments. Only a background count with the reactor shutoff was performed for all following experiments.

The lower level discrimination (LLD) setting on the MCA had to be elevated to 82 prior to the dead time average being reduced to 1.5 percent. The equipment in Table 3-1 was used and the experiment was conducted using the diffracted neutron beam in the KSU reactor facility, for the southeast beam was not available.

Table 3-4: Equipment settings used for neutron response testing of the single domain sample.

Amplifier gain	Times 170
MCA Lower level discrimination (LLD)	Channel 82 or 1 % of the total channels
MCA Upper level discrimination (ULD)	Channel 8192
Bias Voltage	460 Volts

Section 3.4: Experiment III- The Robin's Egg Sample

The sample was synthesized by the Chemical Engineering Team at KSU in the following manner: boron powder dissolved in nickel and chromium with respective mass percentages of 18.3, 65.6, and 16.1 placed in an oven at 1400 ^{o}C for twelve hours in an ammonia atmosphere. The molten mass solidified into the shape of the containing crucible used and attained the shape of a robin's egg; the sample is shown in Fig. 3-7.

Figure 3-7: The robin's egg sample with an h-BN crust on the metal surface exposed to ammonia during heating. The bottom side which was in contact with the crucible, was bare metal without any h-BN crust.

The crusty film surrounding the sample is polycrystalline h-BN; however, within the film, microscopic crystalline h-BN crystals had formed and are shown in Fig. 3-8 (a), while Fig. 3-8 (b) is a cross-sectional impression of the structure showing the assumed position of the h-BN crystals embedded in the surface film relative to the main metal body. There is no proof showing the crystals actually penetrate the surface film and were in physical contact with the sample's main metallic body. A simple ohm-meter was used to determine electrical non-conductivity through the film into the sample's main metallic body. An ohm-meter test also showed that the sample's main metallic body is electrically conductive.

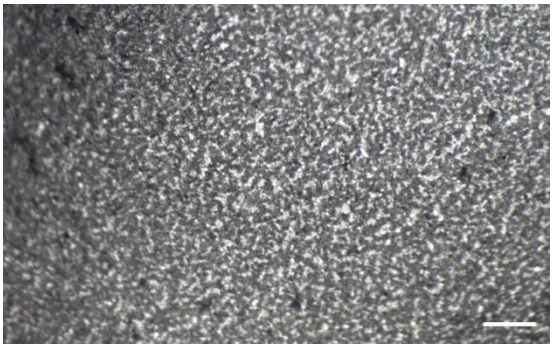

(a)

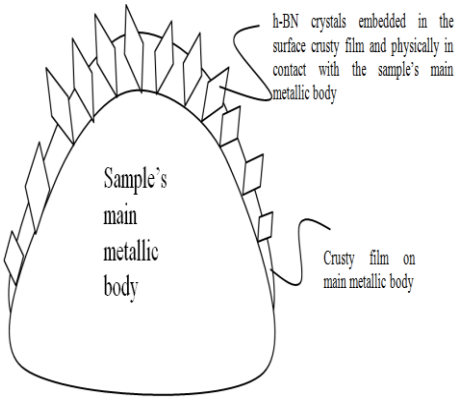

(b)

Figure 3-8: (a)-magnified sample surface showing microscopic h-BN crystals—white dots—embedded in the surface film; the white scale bar, bottom right, represents 100 microns. (b)-An assumed cross-sectional impression of the sample assuming the h-BN crystals are contact with the sample's main metallic body.

Testing the Sample for Neutron Response

Due to their small size, electrical contact was impossible to establish across any single microscopic h-BN crystal embedded in the surface film. Therefore, electrical contact across the crystals was made with the sample's metallic body and to a small surface area of the sample on the crusty side using conductive epoxy with an embedded copper wire tip. The configuration places a multitude of h-BN crystals between two electrical contacts—the sample's metallic body and the conductive epoxy— rendering the crystals as a multitude of neutron conversion mediums in an electrically parallel configuration. Thus if any of the crystals under the epoxy layer converts a neutron, and the h-BN crystal is in contact with the metallic body, and if the crystals possess adequate charge transport mechanisms, a signal should be generated.

However, the epoxy deployed in such fashion completely engulfs the crystals' exposed surfaces and an electrical potential would only be established on a small area on any individual crystal surface. Furthermore, crystalline domain orientation of each of the crystals is not invariant, for the crystals are randomly oriented on the sample's surface and each crystal would have different electrical properties with respect to any other crystal. Both factors will have adverse effects on the device's efficiency should the device respond to neutrons.

Figure 3-9 shows the epoxy and the soldered wire on both sides of the sample. The sample was then placed in the same aluminum box used for experiment I with the epoxy facing the drilled hole. The aluminum box was connected to the circuit with settings shown in Table 3-5 and mounted in front of the Southeast beam for neutron response testing; reactor power level was 50 kW— corresponding to a thermal neutron flux of 23,739 ± 154 $cm^{-2}s^{-1}$; counting and background times were 900 seconds live time.

(a) (b)

Figure 3-9: (a)-The metallic side of the robin's egg sample showing a soldered copper wire. (b)-The side with the crusty of embedded crystals showing the first of two conductive epoxy layers next to the tip of a copper wire whose diameter is approximately 0.5 mm; the copper wire's tip was sandwiched between the first epoxy layer and a second epoxy layer.

Table 3-5: Circuit settings for the robin's egg sample; dead time was 2.6 percent at a LLD level of 250.

Amplifier gain	Times 100
MCA Lower level discrimination (LLD)	Channel 2050 or 25.02% of the total channels
MCA Upper level discrimination (ULD)	Channel 8192
Bias Voltage	500 Volts

Section 3.5: Experiment IV- Assessment of TTU Team's Detector

TTU's detector construction is presented in Fig. 3-10 (a) (Li et al, 2011) the device is fabricated as follows: "Hexagonal h-BN epitaxial layers of about 1 μm thickness were synthesized by metal organic chemical vapor deposition (MOCVD) using natural triethylboron (TEB) sources (containing 19.8% of ^{10}B and 80.2% of ^{11}B) and ammonia (NH_3) as B and N precursors, respectively. Prior to epilayer growth, a 20 nm BN or AIN buffer layer was first deposited on sapphire substrate at 800 ^{o}C. The typical h-BN epilayer growth temperature was about 1300 ^{o}C." The fabrication procedures consisted of the following steps. First, photolithography was employed to define the micro-scale strips (5 μm/5 μm width/spacing) followed by pattern transferring using inductively coupled plasma dry etching to form micro-strips. A bilayer of 5nm/5nm (Ni/Au) was deposited using e-beam evaporation (Li et al, 2011).

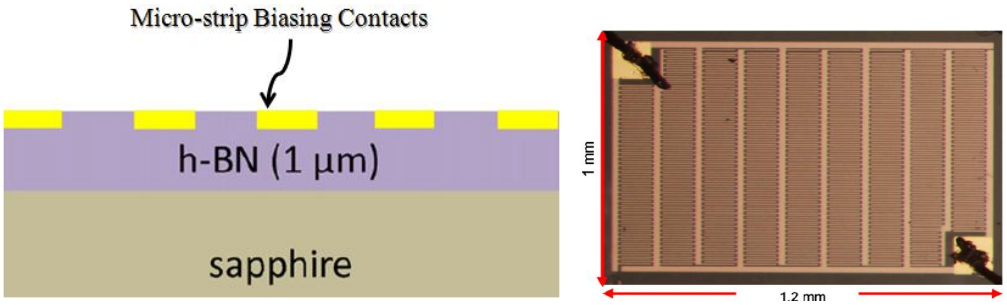

(a) (b)

Figure 3-10: (a)-An impression of the nickel/gold micro-strips embedded in the h-BN epitaxial layering the micro-strips are 5 μm apart and biasing is lateral through the h-BN layering. (b)-The Fig. is a photograph of the continuous winding of the micro-strips on the surface of the h-BN (Li et al, 2011).

Evaluation of the TTU detector involved neutron response on the Southeast beam at KSU's reactor facility; the experiment is simply to determine whether the detector responds to neutrons. Contingent upon successful neutron response, the experiment would proceed into the next phase of neutron detection efficiency determination using the 0.025 eV diffracted neutron beam at KSU's reactor facility.

The breakdown voltage of h-BN is 800 V/mil translating to 31.5 V/ μm. Biasing voltages measured at the preamplifier output were set below 31.5 V to prevent breakdown. The voltage measured at the preamplifier output is lower than the HVPS bias voltage. The equipment used is presented in Table 3-1 and biasing was based on the block diagram in Fig. 3-1. Equipment settings are presented in Table 3-6.

Table 3-6: Equipment settings for the detector fabricated at TTU.

Amplifier gain	Times 1000
MCA lower level discrimination (LLD)	Channel 150 or 1.8% of the total channels
MCA upper level discrimination (ULD)	Channel 8192
Bias voltage at preamplifier output	30 Volts

The LLD setting was raised until a dead time average of 1.5% was reached. Reactor power was set at 100 kW resulting in a thermal neutron flux of 47,478 $cm^{-2}s^{-1}$. The capacitance of the aluminum box detector assembly was 5 pF, which according to ORTEC is within specification for the 142A preamplifier used in the experiment. The preamplifier can be used for detectors with up to 100 pF capacitance. The detector was also tested for biasing conditions by

running an IV curve from -30 to 30 volts on the detector which revealed no *pn* junctions in both directions across the device and the detector consisted of simple Ohmic contacts.

Chapter 4 - Experimental Outcomes

Prior to presenting the results from the experiments conducted for this work note should be made that none of the samples, including the detector fabricated at TTU showed any neutron responsiveness on a MCA pulse height spectrum at the southeast beam or the diffracted beam in the case of the sample in Experiment II. Thus the determination of neutron detection efficiency was not performed in any of the experiments. However the samples in Experiment I did show conductivity and band-gap changes due to irradiation.

Conductivity changes in the p-BN sample batches 1 and 2 are shown in Figs. 4-1 and 4-2 respectively. Band-gap measurements obtained by PL analysis at TTU for select samples (7 and 10) in batch 2 are shown in Fig. 4-3 alongside a PL spectrum of a non-irradiated sample.

Conductivity and Band-gap Changes in Experiment I

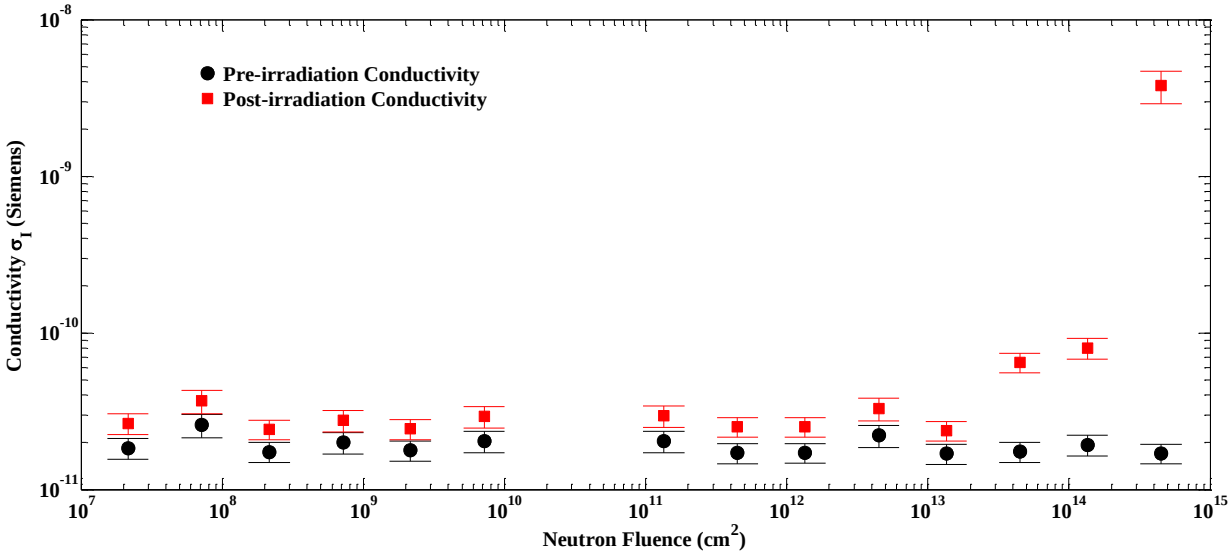

Figure 4-1: Conductivity changes for pre and post irradiation of the samples in batch 1.

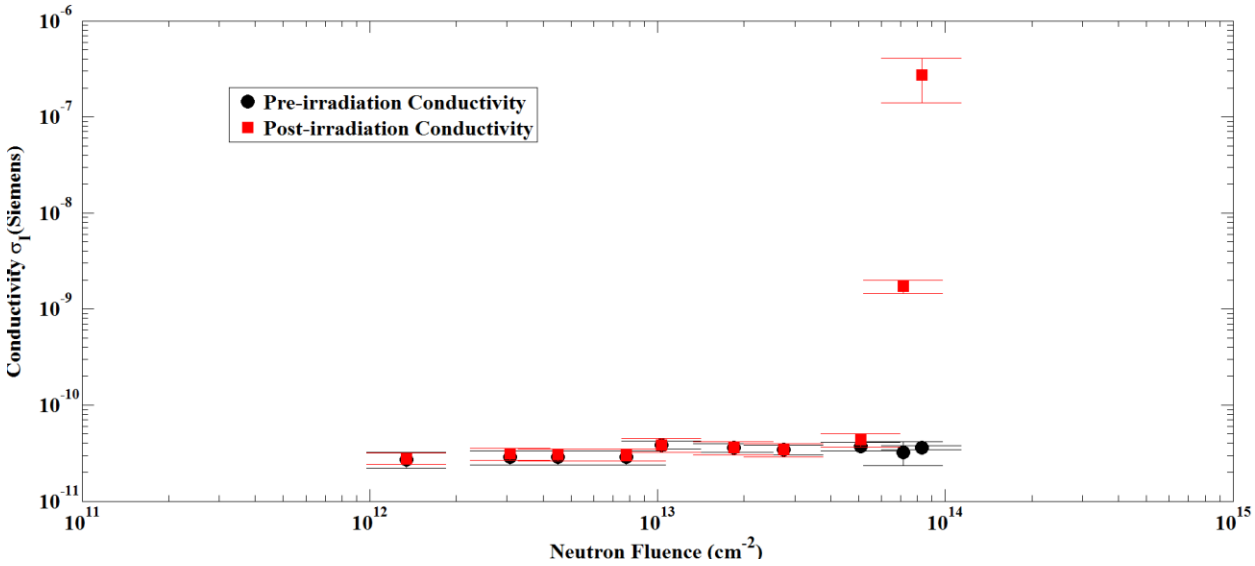

Figure 4-2: Conductivity changes for pre and post irradiation of the samples in batch 2.

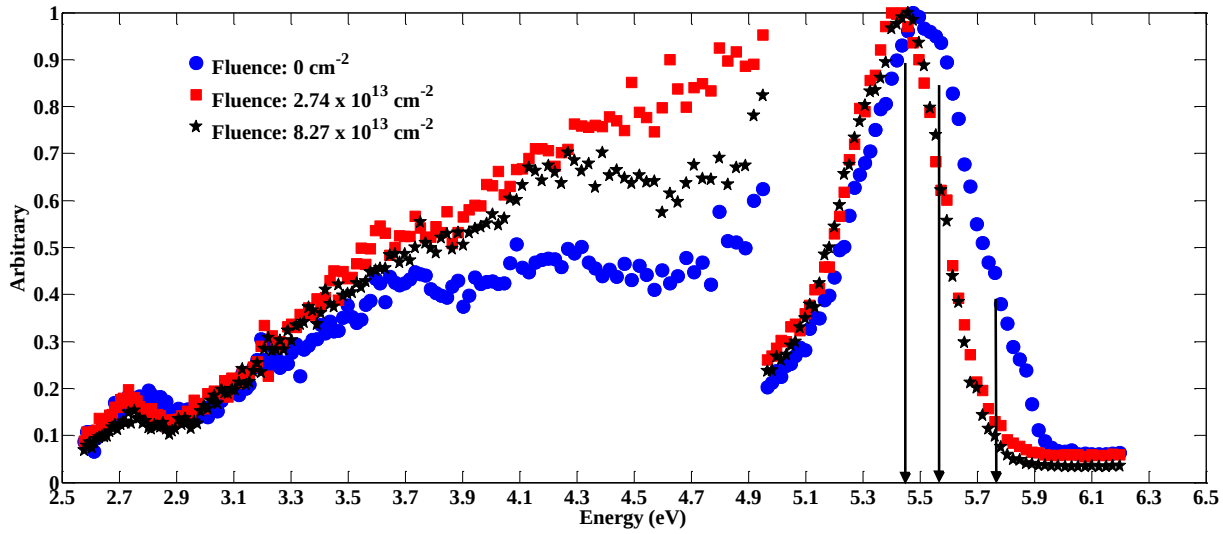

Figure 4-3: Photoluminescence spectra from two irradiated p-BN samples from batch 2 exposed to thermal neutron fluences of 2.74×10^{13} and 8.27×10^{13} cm^{-2}, and a PL spectrum from a non-irradiated p-BN sample. The discontinuity in the data is a result of using different scales on different energy ranges by the TTU staff.

The photon wavelength of each of the energy peaks in Fig. 4-3 can be determined based on the photon energy relation in Eq. 4-1.1

$$E = \frac{hc}{\lambda} \qquad 4\text{-}1.1$$

where E is the photon's energy, in eV, h is Planck's constant and has the value of 4.1356×10^{-15} eV.s^{-1}, c is the velocity of light which is 3×10^{17} nm.s^{-1}, and λ is the photon's wavelength in nanometers. The major energy peak of the PL spectra for p-BN in Fig. 4-3 is at approximately 5.45 eV rendering the wavelength to be 227.6 nm for all samples. For the non-irradiated p-BN sample, the shoulder following the major peak has a wavelength of approximately 223.5 nm and there appear to be, but not definitive, shoulders at wavelengths around 215 nm (5.77 eV) and at 212 nm (5.85 eV).

The pulse height MCA spectra of all the p-BN samples in Experiment I, including the highly irradiated and annealed sample, were not consistent for any single sample under the same biasing voltage and MCA settings and thus the presentation of any of the spectra would not be an accurate description of any of the samples' performance, for repeatability may not be achieved.

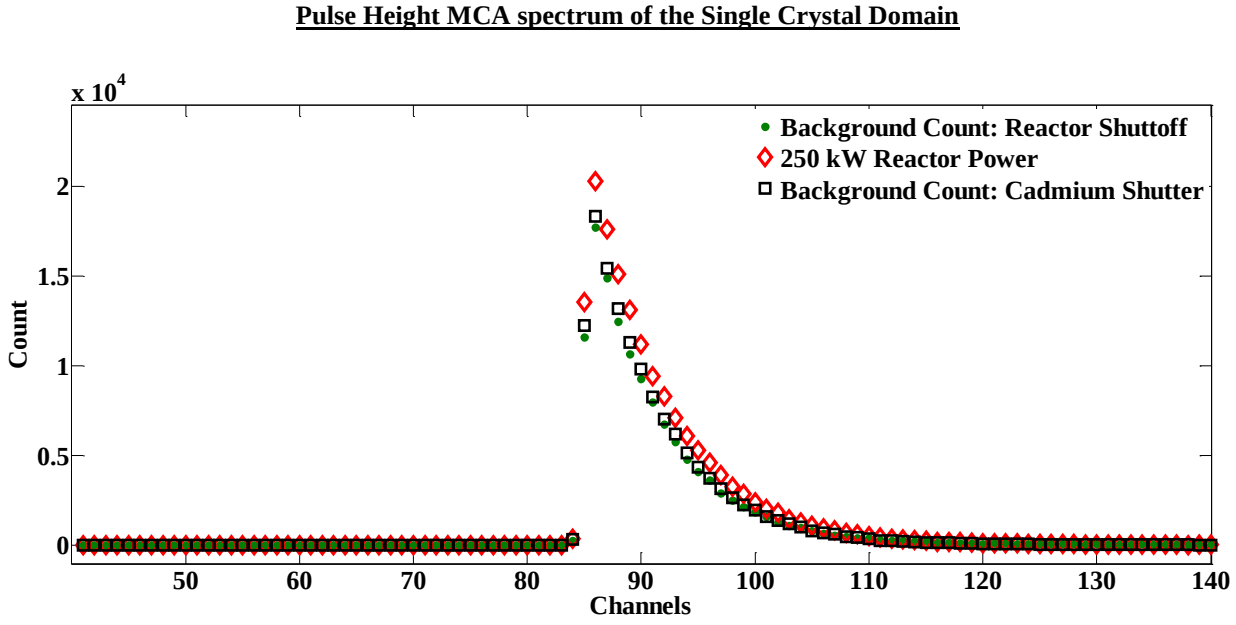

Figure 4-4: MCA pulse height spectra of the single crystal h-BN domain synthesized by the Chemical Engineering Team at KSU. The two background spectra and the spectrum pertaining to the 250 kW reactor power level only show statistical variations characteristic of noise.

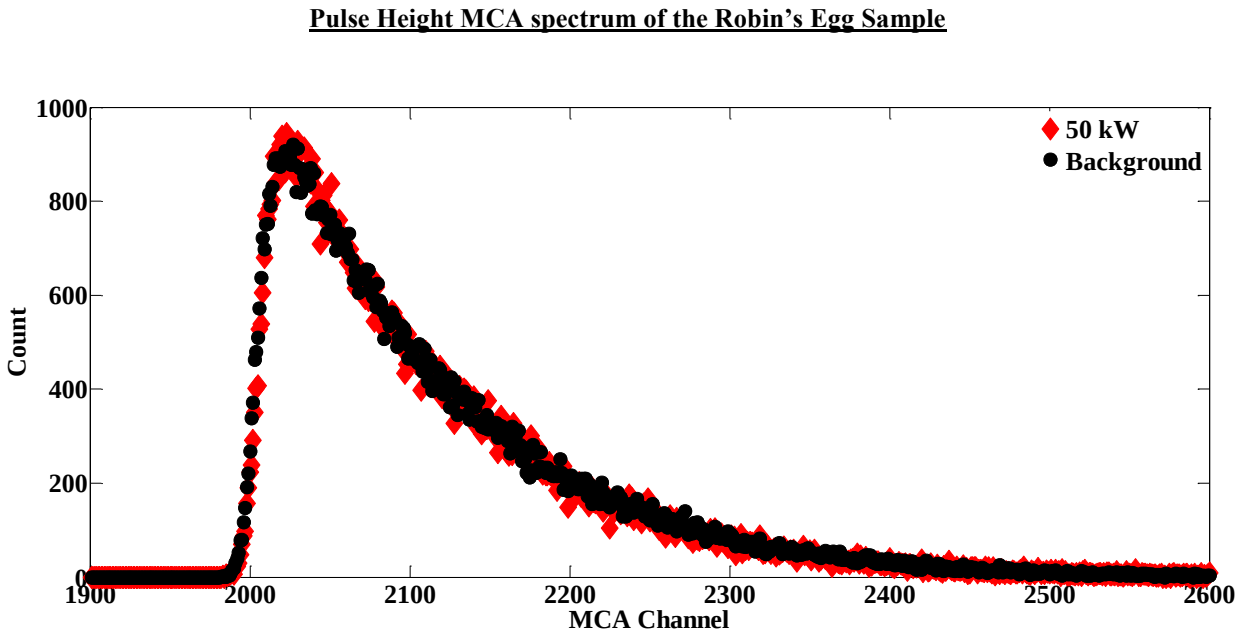

Figure 4-5: The background and the neutron MCA spectra of the Robin's Egg Sample.

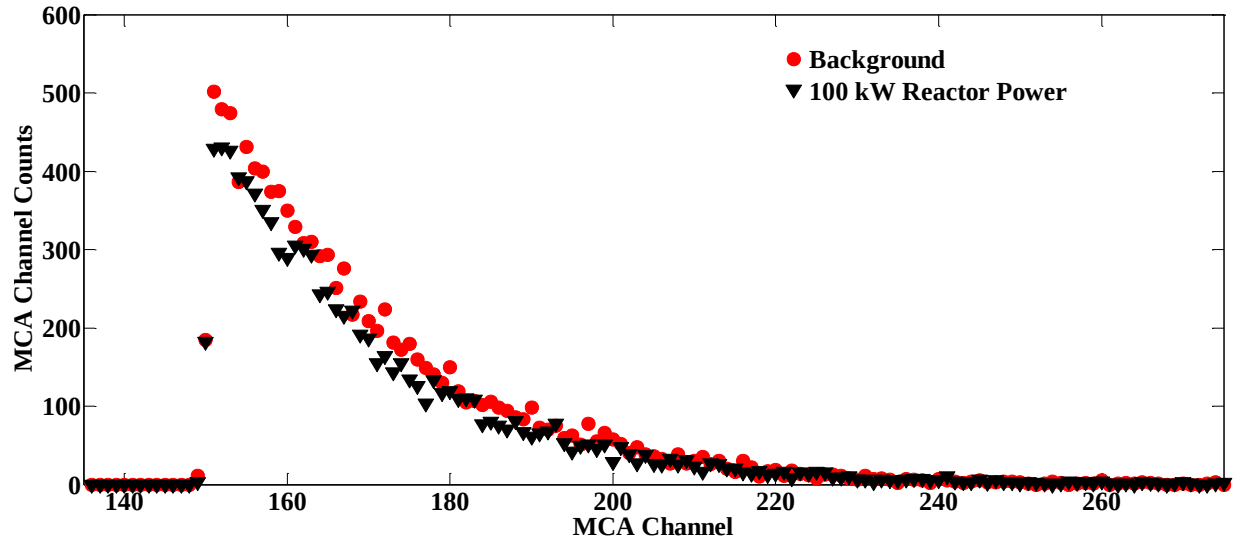

Figure 4-6: The background and the neutron MCA spectra of the detector fabricated at TTU.

Due to the non-responsiveness of the detector to neutrons, the bias voltage was increased to 270 V at the preamplifier's output in an attempt to investigate whether higher bias voltage would improve charge carrier transport properties. However, the voltage arced visibly in the air between the micro strips. An insulator was then sprayed on the detector in an effort to inhibit arcing and the voltage was lowered to 80 V at the preamplifier before visible sparking seized at

the contacts leading into the device. When the detector was observed on the oscilloscope's screen, noise indicative of arcing was observed and a MCA spectrum was not recorded. The IV curve for the detector is shown in Fig. 4-7.

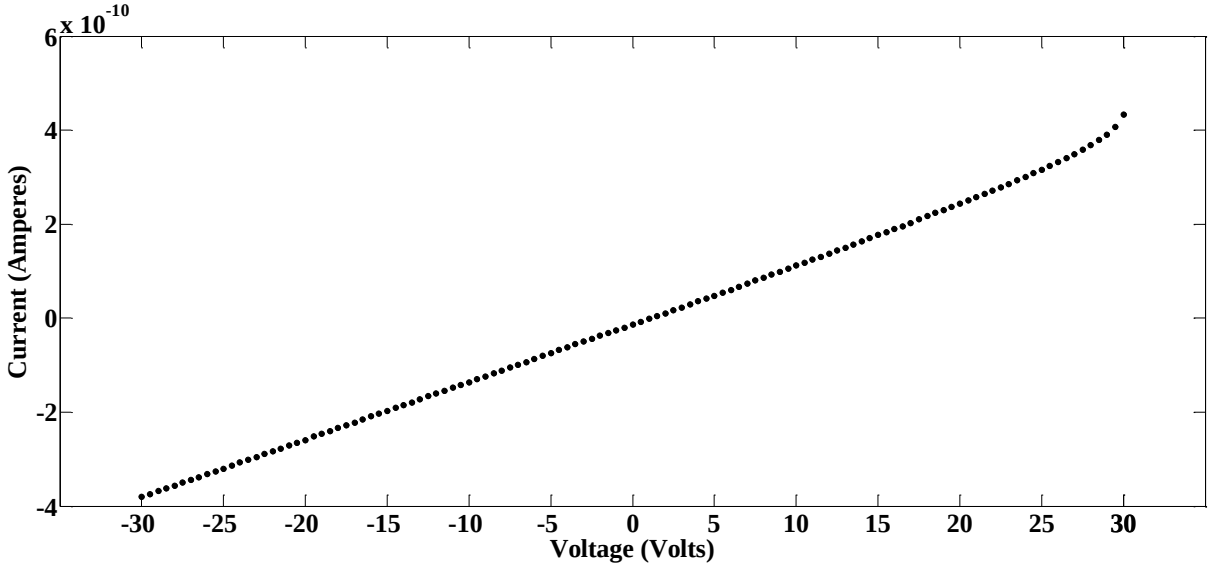

Figure 4-7: The IV curve generated by the detector fabricated at TTU. The IV curve shows that the detector is a simple resistor and does not bear any features pertaining to a *pn* junction. By inverting the IV curve placing voltage on the vertical axis and current on the horizontal axis, and then calculating the slope, resistance, whose value is $7.834\times10^{10}\ \Omega$.

Chapter 5 - Discussion, Conclusions, and Further Work

The pyrolytic h-BN samples used in Section 3.2: Experiment I yielded inconsistent pulse height spectra and a definite conclusive statement cannot be made concerning the inconsistency. A similar experiment conducted with pyrolytic h-BN at an earlier time by (McGregor et al, 2008) yielded some MCA response data; however, the samples did get noisier with increasing neutron fluence and neutron resulting pulses where not discernible from noise (McGregor et al, 2008). Increased noisiness may be due to an increase in conductivity as shown in Figs. 4-1 and 4-2 and an increase in disorderliness as will be later discussed in the current chapter. Batch 2 in Section 3.2 was an effort to observe a smoother transition in conductivity rather than an abrupt increase in conductivity as in batch 1. However conductivity also increased abruptly in batch 2, and a safe conclusion can be stated as: conductivity rises abruptly once initiated at a certain neutron fluence which appears to be between 10^{13} and 10^{14} neutrons.cm^{-2}.

The interesting part of the results from Section 3.2: Experiment I is the bandgap PL analysis. "[h-]BN has a natural tendency toward stacking disorder, such as stacking faults or strained lattice layers" (Watanabe et al, 2006). The PL spectra in Fig. 4-3 show the total disappearance of the 223.5, 215, and 212 nm peaks in the irradiated samples. According to (Watanabe et al, 2006) , where the 215 nm wavelength due to ordered stacking of h-BN layers as shown in the of Fig. 1-3. Also according to (Watanabe et al, 2006), the 227 nm is due to "deformed" h-BN. However, the PL spectrum of the non-irradiated sample shows levels of the 215 nm wavelength indicating some amount of ordered h-BN in pyrolytic h-BN. The 223.5 and 212 nm peaks remain unidentified.

The sample in Section 3.3: "A Single Crystal Domain" is a single crystal domain which according to (Watanabe et al, 2006): "A single crystal has surfaces with predominant cleavage at *c* facets along the layers, and it is easily collapsed by mechanical perturbations that cause the layers to glide along the surface" rendering the sample unworkable leading to the unconventional manner by which electrical contacts were deposited on the sample. The spectrum of the single crystal domain reflecting the 250 kW reactor power level in Fig. 4-4 appears to be slightly higher than both background counts—the reactor shutoff and the neutron beam interrupted by a cadmium shutter—and may be interpreted as a response to neutrons. However, a closer look at

Fig. 4-4 shows the counts in the spectrum pertaining to the 250 kW reactor power level are simply slightly elevated counts of the same energies in the same MCA channels pertaining to both background counts and does not contain any counts in channels describing energies above noise or background energies. Furthermore, the 250 kW spectrum follows the same trend as the background spectra and reaches zero count at the same energy/channel as the background spectra. Therefore the 250 kW spectrum pertaining to the single crystal domain in Fig. 4-4 is a statistical variation of noise.

As far as the sample evaluated in "Section 3.3: The Robin's egg", noisiness and non-responsiveness may be attributed to multiple factors: **first**- the unconventional manner by which electrical contacts were attached, **second**- possible poor charge carrier transport in h-BN, **third** whether the microscopic crystals are in contact with the metallic body of the sample or not is unclear. Whether any of the three mentioned factors is a predominant contributor to noise and non-responsiveness in a MCA pulse height spectrum is unknown.

Concerning the detector fabricated at TTU using un-doped epitaxial grown h-BN layers (Li et al, 2011), the lack of neutron response may be due poor charge carrier transport resulting from stacking faults during epitaxial growth as pointed out by (Watanabe et al, 2006): "In general, a layered material such as h-BN is subject to stacking faults during epitaxial growth that affect its crystallinity." However, even if epitaxial growth does lead to perfect crystallinity, stacking disorders are inevitable once the material is exposed to neutrons as pointed out by the PL results in Fig. 4-3, where the 215 nm wavelength count due to ordered plane stacking disappears due to increasing disordered layer stacking. Thus the exposure of h-BN to neutron fluences on the order of 10^{13} $cm^{-2}s^{-1}$ leads to disordered structures along the charged particles' paths in the crystal and is distributed randomly within the crystal's volume increasing defect concentrations and possibly inhibiting charge carrier transport. The distribution of such disorderliness throughout the crystal changes the electrical properties at interaction localities affecting the overall electrical properties of the crystal as localized disordered regions standing as barriers or traps to normal charge carrier transport (Baranovski, 2006), and doped h-BN is not immune to the phenomenon.

The discussion now has to, very briefly, move into the topic of charge transport in disordered solids, for any neutron detector dependent on h-BN being the NCM and the

operational semiconductor as the charge carrier transport medium simultaneously, as is the proposed detector, is indeed subject to, rather quickly, accumulating disorderliness and "localized [disordered] states [which] can either play the role [of] traps terminating charge carrier transport via extended states or they can be used by charge carriers in the so called 'hopping transport mode', in which the carriers move via direct tunneling between the localized states"(Baranovski, 2006). For further clarification, also from (Baranovski, 2006): "[i]nstead of bands and [energy] gaps, one can only distinguish in disordered materials between extended and localized states. In the former states, the charge carrier wave function is spread over the whole volume of the sample, while in the latter states the wave function of a charge carrier is localized in a spatially restricted region, and a charge carrier in such a state cannot spread as a plane wave, like in ordered materials." Tunneling can be described as the wave function for region two in the potential barrier example in the subsection titled Quantum Mechanics of this work.

The most concise conclusion which may be drawn from the conducted experiments and the PL analysis, is, whether doped or not an h-BN detector based on deploying h-BN as a NCM and a semiconductor simultaneously in order to bypass the charged particle range and neutron absorption conflict presents serious challenges: **First**- h-BN is intrinsically an insulator with a band-gap energy of 5.76 eV and whether doping improves h-BN's charge transport properties is unclear. The TTU team claims the achievement of both *p*-type and *n*-type doping of h-BN in separate h-BN volumes. However, a *pn* junction has not been achieved at this time. **Second**- stacking disorders during crystal growth on a substrate, whether epitaxial or otherwise seem to be unavoidable. **Third**- based on PL analysis results and (Watanabe et al, 2006), any detector based on utilizing h-BN as a semiconductor is subject to lattice stacking disorders upon neutron exposure even though the starting material may have perfect crystallinity. **Fourth**- h-BN grown independently from metal solvent solution may produce high quality single crystal domains (Kubota et al, 2008) with a high degree of orderliness, however detector fabrication from such domains exposes the domains to mechanical perturbations and stresses leading to stacking disorders (Watanabe et al, 2006) which would be compounded when the device is exposed to neutrons.

Besides doping research and crystal growth improvement methods on h-BN, research must also focus on the mitigation of stacking disorders in g-BN in order to avoid the degradation

of possibly existing desirable electrical properties. Special attention must also be paid to the fact where neutron absorption in h-BN does induce considerable localized damage drastically changing charge carrier transport properties at neutron absorption sites. From another point of view, research on heavily disordered h-BN may yield desirable results on the basis where some disordered solids, not necessarily h-BN however, do possess charge carrier transport properties (Baranovski, 2006), however, whether heavily or slightly disordered h-BN does possess adequate charge carrier transport properties can only be answered through further research.

Finally, considering the possibility of an h-BN semiconductor based detector, optimized efficiency requires maximum neutron absorption and a large percentage of energy deposition within the h-BN detector's active volume. The spectrum pertaining to the 7 micron thick h-BN layer in Fig. 2-34 generated by the Monte Carlo code shows complete energy continua pertaining to the resulting charged particles from the reactions in Eq. 1-1.2 suggesting that 7 microns of h-BN manufactured with natural boron is sufficient for signal generation above noise levels. Furthermore, Fig. 2-37 shows approximately 85% averaged energy deposition in 7 microns of h-BN while Fig. 2-38 shows less than 5% neutron absorption for 7 microns of h-BN made with natural boron. Thus a detector employing 7 microns of h-BN made with natural boron as the active volume of the detector may not exceed efficiencies beyond 5%, for the detector cannot absorb more than 5% of impinging neutrons.

An argument of employing enriched h-BN would increase neutron detection efficiency by increasing neutron absorption is plausible. Thicknesses of 7 microns and 30 microns of h-BN made with 100% ^{10}B enriched boron would absorb approximately 25% and 40 % of impinging neutrons, respectively. Employing such highly enriched boron to manufacture h-BN dramatically decreases the mean free path[17] of neutrons in the h-BN and most reactions would take place near the surface being impinged on increasing escapes and reducing average energy deposition. However, considering the opposite directions the resulting particles from the reactions in Eq. 1-1.2 travel, and considering an absorption taking place at the surface exactly; one of the particles will ultimately escape while the other travels into the h-BN medium depositing the totality of the energy the particle was born with in the h-BN medium. Under such circumstances,

[17] The mean free path is the average path length travelled by a particle in a medium prior to an interaction event taking place.

the counts under the continua will increase at a higher rate than counts under the total energy peaks as the enrichment fraction increases. Future analysis using the Monte Carlo code written for the project should reveal design parameters necessary for absorption and energy deposition optimization in a simultaneous fashion.

Bibliography

Baranovski Sergei Charge Transport in Disordered Solids [Book]. - New York : John Wiely & Sons, 2006.

Charles Kittel Introduction to Solid State Physics [Book]. - New York : John Wiely & Sons, 1996.

Contributors Wikipedia Boron Nitride [Online]. - Wikipedia, May 10, 2012. - May 14, 2012. - http://en.wikipedia.org/wiki/Boron_nitride.

D.S. McGregor, T.E. Unruh, W.J. McNeil Thermal neutron detection with pyrolytic boron nitride [Journal] // Nuclear Instruments and Methods in Physics Research. - 2008. - 533 : Vol. A 591 (2008) 530. - p. 4.

Donald A. Neamen Semiconductor Physics and Devices [Book]. - University of New Mexico : McGraw-Hill Higher Education, 1992.

Douglas S. McGregor, J. Kenneth Shultis Reporting detection efficiency for semiconductor neutron detectors: A need for a standard [Journal] // Nuclear Instruments and Methods in Physics Research. - 2011. - 174 : Vol. A 632(2011)167. - p. 8.

Galperin Yuri M. Introduction to Modern Solid State Physics [Book]. - Oslo : Oslo University, 1994.

Griffiths David J. Introduction to Quantum Mechanics [Book]. - Upper Saddle River : Pearson Education Inc., 2005. - Second.

Hugh D. Young, Roger A. Freedman University Physics [Book]. - San Francisco : Pearson, 2004. - 11.

J. Kenneth Shultis, Richard E. Faw Fundamentals of Nuclear Science and Engineering [Book]. - New York : Marcel Dekker Inc., 2002.

J. Li, R.Dahal, S.Majety, J.Y.Lin, H.X.Jiang Hexagonal boron nitride epitaxial layers as neutron detector materials [Journal] // Nuclear Instruments and Methods in Physics Research. - 2011. - 420 : Vol. A654(2011)417. - p. 5.

Kenji Watanabe, Takashi Taniguchi, Takashi Kuroda, and Hisao Kanda Effects of deformation on band-edge luminescence of hexagonal boron nitride single crystals [Journal] // APPLIED PHYSICS LETTERS. - 2006. - 141902 : Vol. 89.

Kevin Osberg, Nathan Schemm, M. Susan Hallbeck, Sina Balkir, Peter A. Dowben, Jennifer I. Brand, and A Handheld Neutron-Detection Sensor System Utilizing a New Class of Boron Carbide Diode. - [s.l.] : University of Nebraska - Lincoln, Research Papers in Physics and Astronomy, 12-1-2006.

Knoll Glenn F. Radiation Detection and Measurment [Book]. - Hoboken, NJ : John Wiely & Sons Inc., 2010. - 4th.

NDT Resource Center NDT Resource Center [Online]. - 2012. - May 14, 2012. - http://www.ndt-ed.org/EducationResources/CommunityCollege/Materials/Structure/linear_defects.htm.

Nicholas Tsoulfanidis, Sheldon Landsberger Measurment and Detection of Radiation [Book]. - Boca Rayton, FL : Taylor & Francis Group, 2010. - 3rd.

Radeka V. Low Noise Techniques in Detectors [Book]. - [s.l.] : Ann. Rev. Nucl. Part. Sci., 1988. - Vols. 38, pp217-277.

Rebecca J. Nikolić, Adam M. Conway, Catherine E. Reinhardt, Robert T. Graff, Tzu Fang Wang, Nirmalendu Deo, and Chin Li Cheung Fabrication of Pillar-Structured Thermal

Neutron Detectors // Published Research - Department of Chemistry. - University of Nebraska - Lincoln : Barry Chin Li Cheung Publications, 12 2, 2007.
S.Ramo Currents Induced by Electron motion [Book]. - [s.l.] : Proc. IRE, 1939. - Vols. 27, pp584-585.
SOLIDSONLINE SOLIDSONLINE [Online]. - University of Pennsylvania, September 01, 2011. - May 14, 2012. - http://www.solidsonline.com/articles/13-Physicists-develop-new-insight-into-how-disordered-solids-deform.
Stephen T. Thornton, Andrew Rex Modern Physics for Scientists and Engineers [Book]. - Southbank, Australia : Thomson Brooks/Cole, 2006. - Third.
T.W. Crane and M.P. Baker Passive Nondestructive Assay of Nuclear Materials [Book Section]. - [s.l.] : Reilly, D. et al., 1991.
Universe The Molecular The Molecular Universe [Online]. - 9 10, 2008. - May 14, 2012. - http://www.themolecularuniverse.com/blog/archives/2008/09/10/defects_add_character/index.html.
W.Shockley Currents to Conductors Induced by a Moving Point Charge [Book]. - [s.l.] : J. Appl. Phys., 1938. - Vols. 9, pp.635-636.
William L. Dunn, J. Kenneth Shultis Exploring Monte Carlo Method [Book]. - Burlington, USA : Elsevier, 2011.
Yoichi Kubota, Kenji Watanabe, Osamu Tsuda, and Takashi Taniguchi Hexagonal Boron Nitride Single Crystal Growth at Atmospheric Pressure Using Ni-Cr Solvent [Journal] // Chemistry of Materials. - 2008. - 5 : Vol. 20.
Ziegler James F. The Stopping and Range of Ions in Matter (SRIM). - 2011.